

OKINAWA INSTITUTE OF SCIENCE AND TECHNOLOGY
GRADUATE UNIVERSITY

Thesis submitted for the degree

Doctor of Philosophy

**Characterization of Nanoscale Defects
in Hybrid Perovskite Thin Films for
Photovoltaic Applications**

by

Sofia Kosar

Supervisor: **Keshav M. Dani**

September 2022



Declaration of Original and Sole Authorship

I, Sofiia Kosar, declare that this thesis entitled “Characterization of nanoscale defects in hybrid perovskite thin films for photovoltaic applications” and the data presented in it are original and my own work.

I confirm that:

- No part of this work has previously been submitted for a degree at this or any other university.
- References to the work of others have been clearly acknowledged. Quotations from the work of others have been clearly indicated, and attributed to them.
- In cases where others have contributed to part of this work, such contribution has been clearly acknowledged and distinguished from my own work.
- None of this work has been previously published elsewhere, with the exception of the following:
 - **Kosar, S.**; Winchester, A. J.; Doherty, T. A. S.; Macpherson, S.; Petoukhoff, C. E.; Frohna, K.; Anaya, M.; Chan, N. S.; Madéo, J.; Man, M. K. L.; Stranks, S. D.; Dani, K. M. "Unraveling the varied nature and roles of defects in hybrid halide perovskites with time-resolved photoemission electron microscopy" *Energy & Environmental Science* **2021**, 14, 6320-6328.

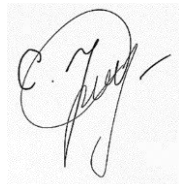
In this project, I have collected, analyzed and interpreted photoemission electron microscopy, photoelectron spectroscopy, time-resolved photoemission electron microscopy, photoluminescence-, scanning electron- and atomic force microscopy data to study defects in perovskite thin films. The data is shown in Figure 1(a,b), Figure 2, Figure 3, Figure 4, Figure S1, Figure S2(c,d,e), Figure S5 - Figure S10 of the paper. Contributions from co-authors can be found in the “Author contributions” section of the paper.

- Doherty, T. A. S.; Winchester, A. J.; Macpherson, S.; Johnstone, D. N.; Pareek, V.; Tennyson, E. M.; **Kosar, S.**, Kosasih, F. U.; Anaya, M.; Abdi-Jalebi, M.; Andaji-Garmaroudi, Z.; Wong, E. L.; Madéo, J.; Chiang, Y.-H.; Park, J.-S.; Jung, Y.-K.; Petoukhoff, C. E.; Divitini, G.; Man, M. K. L.; Ducati, C.; Walsh, A.; Midgley, P. A.; Dani, K. M.; Stranks, S. D. "Performance-limiting nanoscale trap clusters at grain junctions in halide perovskites" *Nature* **2020**, 580, 360-366.

For this work, I have collected, analyzed and interpreted photoemission electron microscopy data to image trap clusters and grain morphology of perovskite thin film samples. I have also collected, analyzed and interpreted atomic force microscopy data. The data is shown in Figure 1(d,e,f) of the paper. The contributions from other authors can be found in "Author contributions" section of the paper.

Date: September 2022

Signature:

A handwritten signature in black ink, appearing to read 'C. E. Petoukhoff', is written over a light gray rectangular background.

Abstract

Hybrid halide perovskites have emerged as one of the most promising contenders for next generation, low-cost photovoltaic technologies. Thanks to the remarkable optoelectronic properties of hybrid perovskite absorbers, perovskite solar cells now achieve efficiencies comparable to conventional inorganic solar cells (Si, GaAs), despite being actively researched for only about a decade. The ability to be processed from solution and to be deposited on transparent and flexible substrates, makes them very attractive for various photovoltaic applications. However, before their wide commercialization, hybrid perovskites need to overcome important limitations. In particular, the presence of defects in perovskite thin films has been detrimental to material properties, and has been a critical reason preventing devices from reaching their full potential. To successfully deploy hybrid perovskites, we must understand the nature of the different types of defects, assess their potentially varied roles in device performance, and understand how they respond to passivation strategies. In this thesis, we employed photoemission electron microscopy to directly image nanoscale defects, and uncovered the presence of multiple types of defects in state-of-the-art perovskite thin films. By adding time resolution to our photoemission electron microscopy measurements, we found that depending on their nature, these defects played varied roles in charge carrier trapping – from highly detrimental to relatively benign. Further, we also found them to show varied response to passivation strategies, as seen from our photoemission measurements. With this work, by identifying the origins of various defects occurring in perovskite thin films and highlighting importance of designing meaningful and targeted strategies to overcome them, as well as demonstrating sophisticated yet greatly rewarding tools to detect these very nanoscale defect-rich sites, we hope to contribute to development of more viable and durable perovskite photovoltaics.

Acknowledgements

I would like to take an opportunity to express gratitude to people who supported me during my work on this thesis.

First of all, I would like to thank collaborators from Stranks Lab at the University of Cambridge. All this work would not have been possible without perovskite films fabricated and carefully shipped to Okinawa by Dr. Stuart Macpherson. I would also like to thank Dr. Tiarnan Doherty, Kyle Frohna, Dr. Miguel Anaya and the team assisting with nXRD measurements who supported allocation of PbI_2 and hexagonal polytype defects for our publication with nanoscale structural information. I would like to acknowledge Prof. Samuel Stranks for the opportunity to contribute to the development of perovskite photovoltaics through the fruitful collaboration between our groups. I thank all the Cambridge team for the opportunity to have enriching discussions about perovskites.

I would like to acknowledge colleagues from the Femtosecond Spectroscopy Unit at OIST. I thank Dr. Andrew Winchester for sharing his knowledge about TR-PEEM and for investing his time and effort in my training. I also thank him for initiating TR-PEEM research of perovskites in our group and for many valuable discussions about data analysis and interpretation.

I thank Dr. Michael Man and Dr. Julien Madéo for their constant technical support. I thank Dr. Michael Man for the help with maintaining PEEM and for various discussions about data analysis and interpretation. I am grateful that I had an opportunity to learn from Dr. Man about instrumentation and technology. I also thank Dr. Man for reading through the draft of this thesis. I thank Dr. Julien Madéo for support with maintaining laser system for my measurements and for being available for discussions about optical experiments. I also thank him for moral support. I would like to thank Dr. Christopher Petoukhoff for being available for discussions about photovoltaics. I also thank him for encouragement and for making me feel confident about my project. I thank Lisa Walter for helping with scanning electron microscopy imaging for Section 6.3.1. I thank Dr. Abdullah Al-Mahboob for joining our perovskite team for a while and for providing his perspective.

I thank Vivek Pareek, Dr. Joel Pérez-Urquizo, Xing Zhu and Dr. E Laine Wong for many nice group outings, movie nights and group trips to remote islands. It was always a lot of fun to plan activities together and spend time with the group. The memories of driving around remote islands in a tiny car fully packed with camping equipment will always stay with me. I thank Nicholas Chan for being available to discuss programming issues and for his company when having cup ramen dinners while working late nights. I thank Dr. David Bacon for moral support and encouragement. I acknowledge Dr. Viktoras Lisicovas for his dedication to maintaining group's website for the past year.

I would lastly like to acknowledge my supervisor Prof. Keshav Dani for the opportunity to join his group and to pursue the topic of my interest for my PhD. I am grateful for the chance to learn a complex technique of TR-PEEM and to be one of the first people applying this instrumentation

to study hybrid perovskite thin films. I appreciated the knowledge and skills I gained in this group a lot. I thank Prof. Dani for his confidence that I would succeed with my work and for encouraging my self-trust as a researcher. I would also like to acknowledge his help and guidance in preparing manuscript published from this work and for discussions regarding my future career directions.

I thank my OIST Thesis Committee Members Prof. Tsumoru Shintake and Prof. Yoshinori Okada for yearly meetings to discuss my research progress and for their valuable comments and encouragement. I also thank my External Thesis Examiners Prof. Libai Huang and Prof. Elbert E. M. Chia for taking their time to read and evaluate this thesis and for their valuable feedback.

Last but not least, I would like to acknowledge my family for their unconditional support. My grandparents Roman and Mariia, my mother Ruslana, my uncle Ivan and my sister Mariia for explaining the importance of education early on and for working very hard to support and encourage me at every step I was taking. I would also like to thank my uncle Ivan and his family Anna and Roman for taking care of me during my stay in Japan and for the privilege to never feel like I was too far from home, because I could always visit a big part of my family in mainland Japan. I also deeply thank Chris for his wholehearted support during these years.

Abbreviations

AFM: atomic force microscopy

BBO: beta barium borate

BQ: benzoquinone

CB: conduction band

CIGS: copper indium gallium selenide

CCD: charge-coupled device

CVD: chemical vapor deposition

DMF: dimethyl formamide

DMSO: dimethyl sulfoxide

DTA: 2,5-di(thiophen-2-yl)terephthalic acid

ETL: electron transport layer

FA: formamidinium

FF: fill factor

FTO: fluorine doped tin oxide

GBL: gamma-Butyrolactone

HTL: hole transport layer

ITO: indium tin oxide

MA: methylammonium

NIR: near infrared

NMA: naphthylmethylamine

PCE: photo-conversion efficiency

PED: photoelectron diffraction

PEEM: photoemission electron microscopy

PES: photoelectron spectrum

PL: photoluminescence

PTAA: poly triaryl amine

SEM: scanning electron microscopy

SPELEEM: spectroscopic photoemission and low energy electron microscope

TCO: transparent conductive oxide

TEM: transmission electron microscopy

TR-PEEM: time-resolved photoemission electron microscopy

TR-PL: time-resolved photoluminescence

UHV: ultrahigh vacuum

UV: ultraviolet

UPS: ultraviolet photoelectron spectroscopy

VIS: visible

VB: valence band

XRD: x-ray diffraction

XPEEM: x-ray photoemission electron microscopy

XPS: x-ray photoemission spectroscopy

Nomenclature

E_B : binding energy

E_{cutoff} : cutoff energy

E_F : Fermi level

E_f : energy of final state

E_g : band gap

E_i : energy of initial state

E_{kin} : kinetic energy

E_{vac} : vacuum level

J_{sc} : short circuit current

J_m : maximum current

R_L : load resistance

R_s : series resistance

R_{sh} : shunt resistance

P_m : maximum power point

P_s : density of incident sunlight

V_m : maximum voltage

V_{oc} : open circuit voltage

\hbar : Plank's constant

$h\nu$: photon energy

ω : transition probability

PbI₂ – lead iodide

Spiro-OMeTAD 2,2',7,7'-Tetrakis[N,N-di(4-methoxyphenyl)amino]-9,9'-spirobifluorene

CH₃NH₃⁺: methylammonium cation

HC(NH₂)₂⁺: formamidinium cation

t : Goldschmidt tolerance factor

μ : octahedral factor

m_0 : mass of electron

D : diffusion coefficient

L : diffusion length

Φ : work function

I_{Pb} : I on the Pb site

I_i : iodine interstitial

Pb_I : Pb on I site

V_{Pb} : lead vacancy

Ψ_i : wavefunction of initial state

Ψ_f : wavefunction of final state

k_{II} : parallel component of momentum vector

nm: nanometer

ns: nanosecond

μ s: microsecond

μ m: micrometer

He-Ne: Helium-Neon laser

Table of Contents

Declaration of Original and Sole Authorship	ii
Abstract	iv
Acknowledgements	v
Abbreviations	vii
Nomenclature	ix
Table of Contents	xi
List of Figures	xiv
Chapter 1. Background and Scope of Investigation	1
1.1 Abstract	1
1.2 Hybrid perovskites	2
1.3 Perovskite thin film photovoltaics	5
1.3.1 Fabrication of perovskite thin films.....	5
1.3.2 Perovskite solar cells	6
1.3.3 Performance of perovskite solar cells.....	9
1.4 Limitations of perovskite photovoltaics	12
1.4.1 Defects in hybrid halide perovskites	13
1.4.2 Defect-induced limitations in perovskite thin films	14
1.5 Thesis objectives and overviews.....	16
Chapter 2. Time-resolved Photoemission Electron Microscopy	18
2.1. Abstract	18
2.2. Photoemission electron microscopy	19
2.2.1. General aspects of photoemission	19
2.2.2. Photoemission electron microscope	21
2.2.3. UV photon sources	23
2.2.4. PEEM resolution and probe depth.....	25
2.3. Time-resolve photoemission electron microscopy	26
2.3.1. General aspects of TR-PEEM.....	26
2.4. Interpretation of TR-PEEM signal.....	29

2.5.	Conclusion	32
Chapter 3. Photoemission Electron Microscopy of Hybrid Perovskite Thin Films		33
3.1.	Abstract	33
3.2.	Nanoscale distribution of defects	34
3.2.1.	Sample preparation and mounting for PEEM	34
3.2.2.	Imaging of nanoscale defects in perovskite thin films with PEEM	36
3.2.3.	Considerations for PEEM imaging	38
3.2.4.	Defects in triple cation mixed halide perovskite thin films	39
3.3.	Surface morphology of perovskite thin films	41
3.3.1.	Imaging surface morphology in hybrid perovskites with PEEM	41
3.3.2.	Considerations for imaging polycrystalline films in PEEM	42
3.4.	Correlation of surface morphology with defect location	44
3.4.1.	Photoemission electron microscopy measurements	44
3.4.2.	Atomic force microscopy measurements	46
3.4.3.	Scanning electron microscopy measurements	48
3.5.	Conclusion	50
Chapter 4. Photoelectron Spectroscopy of Hybrid Perovskite Thin Films		51
4.1.	Abstract	51
4.2.	Photoelectron spectroscopy	52
4.2.1.	Energy-resolved imaging of perovskite thin films	52
4.2.2.	Insights into the origin of defects from PES	55
4.3.	Energetic variations at defect sites	61
4.4.	Conclusion	64
Chapter 5. Time-resolved Photoemission Electron Microscopy of Hybrid Perovskites ...		65
5.1.	Abstract	65
5.2.	TR-PEEM imaging considerations	66
5.2.1.	TR-PEEM imaging of perovskite thin films	67
5.2.2.	TR-PEEM trapping dynamics	70
5.3.	Correlation with steady-state photoluminescence losses	72
5.4.	Conclusion	74

Chapter 6. Effects of Passivation on Defect Distribution in Perovskite Thin Films	75
6.1. Abstract	75
6.2. Passivation by post-treatment	76
6.2.1. Light and environment effects	76
6.3. Passivation during perovskite formation	86
6.3.1. Passivation with KI additives	86
6.4. Conclusion	90
Chapter 7. Conclusion and Outlook	91
7.1. Conclusion	91
7.2. Outlook	93
References	95

List of Figures

Figure 1.1. Perovskite crystal structure with general formula ABX_3 , where A represents an organic or inorganic monovalent cation, B – a divalent metal cation and X – a monovalent inorganic anion.

Figure 1.2. Energy level diagram of an intrinsic semiconductor with valence band denoted as VB , conduction band CB , Fermi level E_F and band gap E_g .

Figure 1.3. Band gap values for perovskites with different compositions. Data acquired from: Tao S. *et al.* for ABX_3 (A = MA, FA, Cs, B = Pb, Sn, X = I, Br) perovskites [42]; Kulkarni S. *et al.* [43], Zhang S. *et al.* [44], McMeekin D. *et al.* [45], Abdi-Jalebi M. *et al.* [46], Doherty T. *et al.* [47], Ogomi Y. *et al.* [48], for mixed compositions.

Figure 1.4. Spin-coating of perovskite thin film using anti-solvent treatment.

Figure 1.5. Schematic of a dye sensitized solar cell. (1), (2), (3), (4), (5) denote absorption of light by the dye, generation of electrons and their injection to TiO_2 , diffusion of electrons to back electrode and to counter electrode, reduction of redox mediator in electrolyte at the counter electrode and recharging of dye, oxidation of redox mediator, respectively.

Figure 1.6. Schematic of a typical perovskite solar cell. ETL , HTL , TCO denote electron- and hole transporting layers, and transparent conductive oxide, respectively.

Figure 1.7. Working principle of perovskite solar cell. Upon absorption of sunlight, electrons in perovskite are promoted to higher energy levels, leaving holes behind. Photo-excited electrons move to electron-transport layer (ETL) and transparent conductive oxide (TCO), while holes move to hole-transporting layer (HTL) and are collected at metal electrode.

Figure 1.8. Current voltage characteristic of an ideal solar cell. J_m , V_m , P_m , J_{sc} , V_{oc} denote maximum current, maximum voltage, maximum power point, short circuit current and open circuit voltage, respectively.

Figure 1.9. Number of literature reports that researched properties of hybrid perovskite thin films on micro- and nanoscale (shown in time frame from 2014 to 2021). Data acquired from [5, 7, 46, 47, 79, 80, 82, 83, 94-96, 98, 114, 133, 134, 136-297].

Figure 2.1. Diagram of photo-emission process. (a) UV light ($h\nu$) causes photo-emission of electrons (e^-) from the surface of a solid (photoelectric effect). (b) Upon absorption of UV photons, electrons (filled red circle) are promoted from the valence band, conduction band and core level states to free electron states above the vacuum level, leaving holes (hollow red circle) behind.

Figure 2.2. Three-step model of photoemission. Adapted from Hüfner S. “Photoelectron spectroscopy: principles and applications” [324].

Figure 2.3. Diagram of photoemission electron microscope. Electro-magnetic lenses are marked with ellipses. *CL1*, *CL2*, *CL3*, *OBJ*, *TL*, *FL*, *IL*, *PI*, *RL*, *INL*, *ACL*, *P2*, *P3* denote Condenser lens 1, Condenser lens 2, Condenser lens 3, Objective lens, Transfer lens, Field lens, Illumination lens, Projective lens 1, Retarding lens, Intermediate lens, Acceleration lens, Projective lens 2, Projective lens 3.

Figure 2.4. Typical working modes of LEEM/PEEM photoemission electron microscope (adapted from Menteş T. and Locatelli A. [325]).

Figure 2.5. Diagram of PEEM experiment. Output beam of a femtosecond pulsed laser source enters the UV light generation set-up (highlighted with grey dashed line). 266 nm and 200 nm light is generated by frequency conversion using nonlinear BBO crystals (1, 2 and 3). The UV beams are coupled to the PEEM through the side window.

Figure 2.6. Spatial resolution of PEEM imaging. (a) 84 % 16 % profile for perovskite thin film sample with good alignment showing best resolution of 18 nm. (b) 84 % 16 % profile for perovskite sample with poor alignment and space charge effects showing decreased spatial resolution of 46 nm.

Figure 2.7. Diagram of time-resolved photoemission. (a) The UV light (*UV probe*) arrives after the sample was photo-excited with pump pulse (*pump*) and causes photo-emission of electrons (e^-) from the surface of a solid. (b) Upon absorption of pump photons, electrons (red circle) from the valence band states are promoted to conduction band leaving holes (hollow red circle) behind. The UV probe pulses photo-emit electrons from the conduction band to the free electron states above the vacuum level. (c) Snapshots of electron motion at selected time delays between pump and UV probe pulses in TR-PEEM.

Figure 2.8. Diagram of TR-PEEM experiment. Output beam of a femtosecond pulsed laser source is split for the generation of UV light (highlighted with grey dashed line) and for the optical pump. Pump beam passes through a mechanical delay stage and is focused on the sample through the side window of PEEM.

Figure 2.9. Interpretation of TR-PEEM signal. (a) Energy level diagram of p-doped GaAs sample. Upon photo-excitation with pump photons (*pump*), electrons (filled red circles) are promoted from valence band (*VB*) to the conduction band (*CB*), leaving holes behind (hollow red circles). UV probe photons (*6.2 eV probe*) cause photo-emission of remaining electrons from valence band states to the vacuum level (E_{Vac}). By changing time delay between pump and probe pulses, the evolution of the population of valence band states can be traced. (b) TR-PEEM decay curve for the process described in (a). Because electrons are promoted from the valence band states to the conduction band states, the population of valence band decreases, and change in photoemission intensity is negative. (c) TR-PEEM images for selected time delays in (b), showing a clear decrease in photoemission intensity colored with blue. (d) Energy level diagram for GaAs sample when probed with photons of lower energy (*4.65 eV probe*). Again, pump photons (*pump*) cause photo-excitation of electrons from valence band (*VB*) to conduction band (*CB*). Here, however, the lower energy photons photo-emit the photo-excited electrons from the conduction band to the vacuum level (E_{Vac}). (e) TR-PEEM decay curve for the processes

described in (d). Because here we are probing conduction band states that were populated after the photo-excitation, the change in photoemission intensity is positive. (f) TR-PEEM images for selected time delays in (e), showing clear increase in photoemission intensity after photo-excitation colored with red.

Figure 3.1. PEEM sample mounting. (a) Sample holder that consists of a cartridge and a cap. (b) Perovskite thin film sample on glass/ITO substrate positioned on the sample holder before covering with cap. (c) Sample holder with perovskite sample inside the preparation chamber of PEEM. (d) Hermetically sealed suitcase for transferring air-sensitive samples to PEEM.

Figure 3.2. Optical microscopy images of a perovskite thin film sample. (a) A uniform film surface, typically expected for good-quality perovskite films. (b) Gold fiducial markers deposited on the film surface for guidance in correlative measurements.

Figure 3.3. PEEM imaging of nanoscale defects in perovskite thin films. (a) Energy-level diagram of perovskite sample: green arrow indicates transition from defect states (*defects*) below the Fermi level (E_F) to vacuum states with E_{Vac} when probing of sample with photon energies of 4.65 eV; valence band states are indicated with E_V , conduction band states with E_C . (b) PEEM image visualizing nanoscale distribution of defect clusters (colored with green) on the surface of triple-cation mixed halide perovskite thin film. Pristine regions without defects, do not show PEEM intensity upon probing with 4.65 eV photons.

Figure 3.4. PEEM imaging of nanoscale defects with energy-filtering. (a) Energy-level diagram of perovskite sample: grey arrow indicates transitions from valence states (E_V), defect states (*defects*) below the Fermi level (E_F) to vacuum states (E_{Vac}) when probing of sample with photon energies of 6.2 eV; conduction band states are marked with E_C . (b) Energy-filtered PEEM image visualizing nanoscale distribution of defect clusters on the surface of triple-cation mixed halide perovskite thin film. The image was acquired using energy analyzer and with an energy slit to collect only contributions from mid gap states, as indicated with green dashed box in (a).

Figure 3.5. Size distribution of nanoscale defects in perovskite thin films. (a) A typical PEEM image of defects. (b) Size distribution of defects (from a 6 μm by 6 μm area). (c) Magnified PEEM images of defects of different in sizes, from few tens to few hundreds of nanometers.

Figure 3.6. PEEM imaging of surface microstructure of perovskite thin films. (a) Energy-level diagram of perovskite sample: grey arrow indicates transitions from valence band states (E_V) to vacuum states (E_{Vac}) when probing of sample with photon energies of 6.2 eV; Fermi level is indicated with E_F , and conduction band states are indicated with E_C . (b) High-resolution PEEM image of grains of the same area that was shown in Fig. 3.3.

Figure 3.7. Topological contrast in PEEM and AFM imaging. (a) PEEM image of surface microstructure of perovskite thin film. (b) AFM image of surface height variation of the same region of perovskite sample as shown in (a).

Figure 3.8. Spatial distribution of defects with respect to surface morphology. (a) PEEM image acquired with 4.65 eV probe photons showing nanoscale defects (blue). (b) PEEM image acquired with 6.2 eV probe photons showing grain morphology of the same region of the film as in (a). (c) Superimposed PEEM images of defects (blue) and grains (grey). (d) Magnified region from (c) showing a nanoscale defect situated at boundary between two morphological

grains. (e) Line profile of the intensity from the 4.65 eV PEEM image (blue) against the intensity from the 6.2 eV PEEM image (grey). Numbering corresponds to regions of interest in (c).

Figure 3.9. Spatial arrangement of nanoscale defect clusters. (a) PEEM overlays of 4.65 eV images of defects (green) and 6.2 eV images of grains (grey). Smaller defects were found to be located at specific grain boundaries (“Grain boundary defects”), while larger defects were associated with entire grains (“Intra-grain defects”). (b) PEEM images of grain morphology. White circles are showing the locations where defects are situated.

Figure 3.10. Correlation of grain boundary defects with atomic force microscopy. AFM images of grains overlaid with PEEM images of grain boundary defects for the same areas as discussed in Figure 3.8.

Figure 3.11. Relation of local morphological variations and presence of nanoscale defects. (a) PEEM images of grain boundary (green box) and intra-grain (red and blue boxes) defects. (b) AFM images of the same regions as (a). White dashed circles mark locations of defects.

Figure 3.12. Characterization of surface morphology with SEM and PEEM. (a) Images of surface morphology acquired with (a) SEM and (b) PEEM. PEEM topography of grains and grain boundaries follows the SEM image reasonably well. The parts of the film exhibiting low PEEM contrast or poor resolution, can be imaged in SEM with better quality.

Figure 3.13. Relation of local morphology imaged with SEM to spatial location of nanoscale defects. (a) PEEM images of grain boundary (green box) and intra-grain (red and blue boxes) defects. (b) SEM images of the same regions as (a) with locations of defects marked with white dashed circles for better visibility. (c) AFM images of the same regions as (a and b) with line profiles through the defect clusters indicating the raised height only for some of the intra-grain defects. Solid black line indicates mean height for the sample, with grey shaded area denoting the root mean-square bounds.

Figure 4.1. Schematic of a spectroscopic PEEM. UV probe pulses cause photoemission of electrons from sample surface; electrons are then accelerated through hemispherical energy analyzer, dispersed in energy, and imaged on CCD camera for each energy. In this way a sequence of energy-filtered PEEM images can be collected. Inset shows energy level diagram of hybrid perovskite: grey arrow indicates transitions from valence band states (E_V) through the defect states (*defects*) below the Fermi level (E_F) to vacuum states (E_{Vac}) upon probing of sample with photons of 6.2 eV in energy.

Figure 4.2. Energy-filtered PEEM images of perovskite thin film collected when probing samples with 6.2 eV photons. At the energies from -2.1 eV to -1.4 eV, the contrast shown is due to surface morphology (highlighted with grey box). Localized nanoscale defects appear in images from -1.3 eV to -0.1 eV below the Fermi level (0 eV), and are highlighted with green box. The intensity of each image is scaled independently for better visibility.

Figure 4.3. Photoelectron spectroscopy of perovskite thin film samples. (a) PEEM image of pristine grains. (b) Averaged PES extracted from the entire area shown in (a). (c) PES of a single pristine grain indicated with red in (a). (d) Overlaid PEEM images of defects (green) and surface morphology (grey contrast). (e) Photoelectron spectrum extracted for the region containing nanoscale defects shown in (d). PES contains contributions from both valence band and mid gap

defect states. (f) Magnified part of PES in (e) shown with black line and square, and PES of pristine region in (b) shown with grey line and circle.

Figure 4.4. Photoelectron spectroscopy of intra-grain defects. Typical (a) PEEM and (b) SEM images and (c) PES (blue line) of intra-grain defect associated with morphological grain. (d) PES of multiple defects as described in (a), showing consistent large density of mid gap states. (e) PEEM and SEM images of additional intra-grain defects similar to (a). Typical (f) PEEM and (g) SEM images and (h) PES (red line) of intra-grain defect associated with grain with brighter SEM contrast. (i) PES of multiple defects as described in (f), showing consistent lower density of mid gap states, as compared to (d). (j) PEEM and SEM images of additional intra-grain defects similar to (f).

Figure 4.5. Photoelectron spectroscopy of grain boundary defects. Typical (a) PEEM and (b) SEM images of defects that appeared at grain boundaries. (c) PES of the grain boundary defect (green line). (d) PES of multiple grain boundary defects showing low density of mid gap states.

Figure 4.6. Photoelectron spectra for intra-grain (blue and red) and grain boundary (green) defects averaged for multiple features of the same type, as compared to pristine areas (grey). Inset shows contributions from mid gap states on logarithmic scale.

Figure 4.7. Estimation of energy distribution of defects. (a) Gaussian fits (red, yellow, purple) to the photoelectron spectra for selected defects used to estimate peak energy of the mid gap states. (b) Estimated $E - E_F$ of mid gap states for different types of defects based on fitting: grain boundary-, PbI_2 and another type of intra-grain defects are represented with green, red and blue bars, respectively.

Figure 4.8. Photoelectron spectroscopy of grains and nanoscale defects. (a) Overlaid PEEM images of grains and defects. (b) Photoelectron spectra of defects and pristine grains. For some of the intra-grain defects shifted cutoff energy was observed.

Figure 4.9. Plotting two-dimensional work function maps. (a) Photoelectron spectrum extracted from energy-filtered images of perovskite thin film. (b) Processing steps to determine cutoff energy and calculate work function. (c) Work function map plotted for an area of perovskite thin film of about $3 \mu\text{m}$ by $3 \mu\text{m}$. (d) Amplitude map that follows grain morphology, generated during the processing.

Figure 4.10. Correlation of defects and local work function. (a) PEEM image and work function map of a pristine region of perovskite thin film. (b) Overlaid PEEM images and work function maps of regions associated with intra-grain defects. (c) Overlaid PEEM images and work function maps of regions associated with grain boundary defects. White dashed circles are outlining locations of nanoscale defects.

Figure 5.1. Schematic of time-resolved PEEM experiment of perovskite sample. Inset shows energy-level diagram of perovskite sample at the instance of photo-excitation. Incident pump photons (*pump*) promote electrons in perovskite from valence band states (E_V) to the conduction band states (E_C). The time-delayed UV probe photons (*UV probe*) photo-emit electrons from defect states (*defects*) below the Fermi level (E_F) to the vacuum level (E_{Vac}). For each time delay between pump and probe, a PEEM image is recorded.

Figure 5.2. Time-resolved PEEM images of perovskite thin film. For pristine regions that were not associated with nanoscale defects, no changes in photoemission intensity were observed after photo-excitation, implying absence of charge trapping. The defects associated with precipitated PbI_2 , did not demonstrate any obvious signs of charge trapping upon photo-exciting perovskite, while the intra-grain polytype- and grain boundary defects, showed clear hole-trapping signal as seen from reduction of photoemission intensity at their sites. Color scale indicates change in PEEM intensity ($I(t) - I_0$): blue color denotes reduction in photo-emission intensity, while red color – increase in photoemission intensity.

Figure 5.3. Time-resolved PEEM dynamics. TR-PEEM decay curves plotted as percentage change in PEEM intensity after photoexcitation ($[I(t) - I_0]/I_0 \times 100$) versus pump–probe time-delay for (a) pristine region, (b) PbI_2 defects, (c) grain boundary defects and (d) intra-grain polytype defects. Solid lines represent exponential decay fits.

Figure 5.4. Correlation of PEEM and photoluminescence maps. (a) PEEM image of nanoscale defects. (b) Photoluminescence intensity map overlaid with PEEM map of defects for the same region as (a). (c) Magnified regions of interest as indicated with color-coded boxes in (b), showing overlaid PEEM/PL maps of pristine region (black box), region associated with PbI_2 defect (red box), intra-grain polytype defect (blue box) and grain boundary defect (green box).

Figure 6.1. Schematic of photo-exposure measurements. Step (1) covers PEEM measurements including PEEM imaging of defects, PES and TR-PEEM; at step (2), photo-exposure is conducted in an external chamber filled with dry air; at step (3), PEEM measurements are repeated again after the treatment.

Figure 6.2. TR-PEEM response of grain boundary defects to photo-exposure in dry air. (a) PEEM and TR-PEEM images of selected grain boundary defect before exposure (“Unexposed”) and after treatment with 1 mbar dry air (“After treatment”) upon illumination. (b) TR-PEEM dynamics before and after treatment for grain boundary defects plotted as percent change in PEEM intensity $[I(t) - I_0]/I_0 \times 100$.

Figure 6.3. Response of intra-grain defects to photo-exposure under 1 mbar dry air. (a) PEEM images of a selected intra-grain polytype defect before (“Unexposed”) and after the treatment (“After treatment”). Images are plotted on the same intensity scale. (b) Photoemission spectra of the defects in (a) showing that density of occupied mid gap states was not obviously affected by the treatment. (c) PEEM images of a selected intra-grain PbI_2 defect before and after the treatment. Images plotted on the same intensity scale. (d) Photoemission spectra of the defects shown in (c). Similar to (b), the density of occupied mid gap states for PbI_2 defects was not affected by the treatment.

Figure 6.4. TR-PEEM response of intra-grain defects to photo-exposure in dry air. (a) PEEM and TR-PEEM images of selected intra-grain polytype (blue box) and PbI_2 (red box) defects before exposure and after treatment with 1 mbar dry air upon illumination. (b) TR-PEEM dynamics before and after the treatment for intra-grain polytype (blue line) and PbI_2 (red line) defects, plotted as percent change in PEEM intensity $[I(t) - I_0]/I_0 \times 100$.

Figure 6.5. Response of polytype intra-grain defects to photo-exposure with different dry air conditions. (a) PEEM images of a selected defect before exposure and after treatments, shown

on the same intensity scale. (b) Photoelectron spectra plotted for the defects shown in (a), with contribution from mid gap states highlighted with blue shaded boxes.

Figure 6.6. Response of PbI_2 defects to photo-exposure with different dry air conditions. (a) PEEM images of a selected defect before exposure and after treatments, shown on the same intensity scale. (b) Photoelectron spectra plotted for the defects shown in (a), with contribution from mid gap states highlighted with red shaded boxes.

Figure 6.7. Evolution of photoelectron spectra of intra-grain defects and pristine areas before and after the treatment. (a) Photoelectron spectra of selected intra-grain polytype defect (blue line) and pristine grains (grey) before the treatment (“Unexposed”) and after photo-exposure with 1 mbar and 10 mbar dry air upon illumination, as labelled. By tracking cutoff energy, larger energy shift is observed between defect site and pristine grains after the treatment. (b) Evolution of photoelectron spectra of PbI_2 defects, showing similar increased energy shift between defect site and pristine grains after the treatment.

Figure 6.8. Evolution of defects after treatment. PEEM images of intra-grain defects before treatment (“Unexposed”), after photo-exposure in dry air (“After treatment”) and one day after the treatment (“1 day after treatment”). PEEM images were taken with same exposure conditions and are shown of the same intensity scale.

Figure 6.9. Distribution of defects in K-passivated perovskite thin films. (a) Energy-level diagram of perovskite sample when using 4.65 eV probe photons. (b) Estimated defect sizes (analyzed within 5 μm field of view). (c) PEEM image of surface defects in K-passivated perovskite thin film. (d) PEEM image of defects in un-passivated sample.

Figure 6.10. Correlation of defects in K-passivated samples with surface morphology. (a) PEEM image of defect in K-passivated samples acquired with 4.65 eV photons. (b) SEM images of the same area as (a). Red dashed circles are indicating defects in (a) that are associated with morphological grains in (b). (c) Magnified PEEM and SEM images from the areas marked with blue boxes in (a) and (b), showing intra-grain nature of defects in K-passivated perovskite films.

Figure 6.11. Photoelectron spectroscopy of K-passivated perovskite thin film. (a) PEEM image of selected intra-grain defect. (b) Photoelectron spectrum of intra-grain defect highlighted with green circle in (a). (c) Photoelectron spectra of intra-grain defect highlighted with green circle in (a) and pristine area highlighted with grey circle in (a), showing energy shift towards higher work function values for the defect site.

Figure 6.12. TR-PEEM signal of intra-grain defects in K-passivated perovskite thin film. 1.55 eV photons with fluence of about 100 $\mu\text{J cm}^{-2}$ were used for photoexcitation. TR-PEEM response was recorded for intra-grain defects and averaged for multiple defects.

Chapter 1

Background and Scope of Investigation

1.1 Abstract

The primary aim of this thesis is to understand the underlying limitations in performance of hybrid perovskites – materials that are employed as light absorber layers in perovskite photovoltaic devices. Hybrid perovskites are emerging materials on the market of solar cells, and despite being introduced only about a decade ago [1], perovskite solar cells have already reached impressive photo-conversion efficiencies (PCE) exceeding 25 % for single junction solar cells [2], which is approaching efficiencies of single crystal Silicon based devices [2]. Despite rapid development of devices, the understanding of properties and limitations of hybrid perovskites has been slower, as it requires comprehensive and time-consuming investigation, as well as utilization of state-of-the-art equipment. In particular, many interesting phenomena in hybrid perovskites have been found on micro- and nanoscale [3, 4]. This implies that utilization of appropriate methodologies with high degree of spatial resolution, is required to shed light on their origin. Among those phenomena are nanoscale heterogeneities in properties, such as photoluminescence intensity, that have been observed and associated with presence of charge-trapping defects [5-8]. Such defect-mediated charge trapping processes result in non-radiative recombination and limit maximum PCE that perovskite photovoltaic devices can output [9, 10], and therefore, should be avoided in commercially-viable devices. The formation of defects has been proposed to be induced during the film fabrication [11-14], when growth conditions become favorable for some defect types to introduce high density of non-radiative recombination centers that energetically lay deep in the band gap [15-22]. The distribution and exact origin of such defects, as well as their direct impact on device efficiency, are not yet well understood, and form the basis of investigation in this thesis, where we focus on accessing the origin of defects and their roles in charge trapping on spatial-, energy- and temporal landscapes. This Chapter starts with an introduction to hybrid halide perovskites in Section 1.2, followed by discussion of thin film perovskite photovoltaics in Section 1.3, limitations of hybrid perovskites in Section 1.4 and concludes with setting objectives and short overview of the work accomplished within this thesis in Section 1.5.

1.2 Hybrid perovskites

Hybrid perovskites represent a family of semiconducting materials that have generated resonant attention over the past decade due to their wide application for photovoltaics. While remarkable optoelectronic properties of these materials allow them to serve as absorber layers in state-of-the-art solar cells, hybrid perovskites have also found application as light-emitting diodes [23-25], photo- and X-ray detectors [26-32].

Hybrid perovskites typically crystallize in a cubic perovskite structure, have a general formula of ABX_3 , and are composed of Earth-abundant elements. The A site is usually occupied by a monovalent cation that can be either organic or inorganic, while B - a divalent metal cation is six-fold coordinated with a monovalent X anion. There is a wide variety of ions that can occupy A, B, and X sites, however the most common are methylammonium ($CH_3NH_3^+$), formamidinium ($HC(NH_2)_2^+$), Cs^+ for A site, Pb^{2+} , Sn^{2+} , Ge^{2+} for B site, and I^- , Br^- , Cl^- for X site, as shown in the schematic in Figure 1.1.

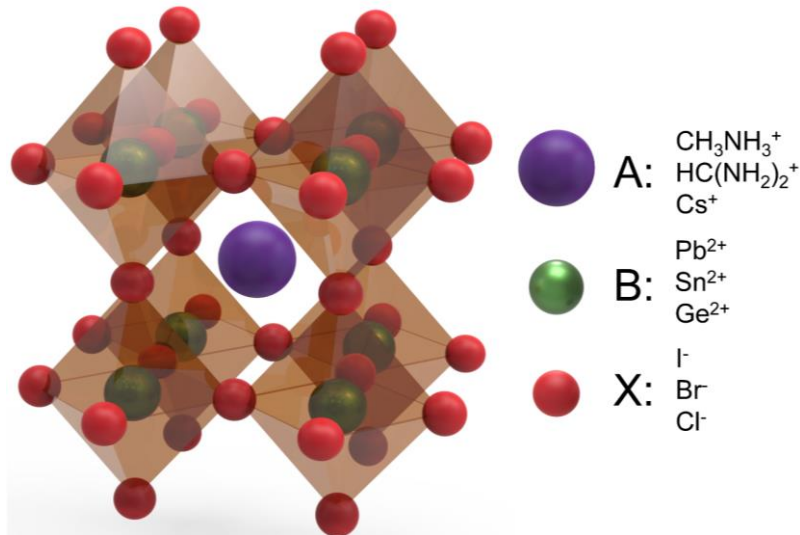


Figure 1.1. Perovskite crystal structure with general formula ABX_3 , where A represents an organic or inorganic monovalent cation, B – a divalent metal cation and X – a monovalent inorganic anion.

The sizes of ions should satisfy the Goldschmidt tolerance factor t (calculated according to the Equation 1.1 [33, 34]) in order to keep the perovskite lattice stable, where r_A , r_B , r_X represent the ionic radii of the A, B, and X site ions, respectively. A stable cubic perovskite lattice can be realized for combination of ions with t in range of ~ 0.9 to 1.0 . The t values of < 0.8 , result in formation of orthorhombic perovskite lattice, while $t > 1.0$ – in tetragonal or hexagonal structure. Additionally, the octahedral factor μ (Equation 1.2 [35, 36]) determines fit of the B site anion into the X_6 octahedron to keep the lattice stable. Li *et al.*, have estimated the lowest limit of the octahedral factor for perovskite formation to be of about 0.425 [35].

$$t = \frac{r_A + r_X}{\sqrt{2}(r_B + r_X)} \quad (1.1)$$

$$\mu = \frac{r_B}{r_X} \quad (1.2)$$

Hybrid perovskites are semiconductors, which means that their valence band maximum (VBM) and conduction band minimum (CBM) are separated by an energy gap, called band gap (E_g) (Figure 1.2). The compositional diversity of hybrid perovskites, allows to achieve tunability in band gap values by simply changing ions at A, B, and X sites or their ratio [37]. B and X site components are crucial when tuning the band gap, since the contributions from p -states of X-site anion dominate the valence band of perovskites along with contributions from s -states of B-site cation, while conduction band is predominantly composed of $2p$ -states of B-site cation [38-41]. Thus, band gap values in range of ~ 1.2 eV – 3.5 eV can be generated by mixing appropriate ions in perovskite structure [42-48] (Figure 1.3). Another important factor to highlight is that hybrid perovskites are direct band gap semiconductors, which means that VBM and CBM occur at the same point in momentum space. This results into efficient charge carrier generation upon absorption of incident photons, due to favorable probabilities for transition between initial and final states, and makes perovskites very attractive for photovoltaic and light-emitting applications. In addition, hybrid perovskites have high absorption coefficient ($\sim 10^5$ cm $^{-1}$ [49]), which is comparable to materials that compose highly efficient solar cells [50, 51], and means that a thin layer of perovskite (just few hundreds of nanometers) is sufficient to absorb most of the absorbable incident solar light.

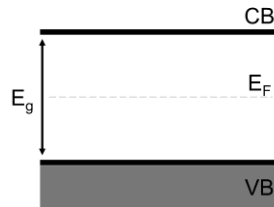


Figure 1.2. Energy level diagram of an intrinsic semiconductor with valence band denoted as VB , conduction band CB , Fermi level E_F and band gap E_g .

Perovskite thin films have variety of interesting transport properties. Despite effective masses of electrons and holes of about $0.2m_0$ [38] being comparable to other materials heavily used in photovoltaics [52, 53], the diffusion coefficients and mobilities for polycrystalline perovskite thin films are modest [54]. The diffusion coefficients are on the order of (0.05 – 0.2) cm 2 s $^{-1}$ [55-59], while charge carrier mobilities have been reported in the range of (1 – 30) cm 2 V $^{-1}$ s $^{-1}$ [60-62]. In spite of this, perovskite thin films possess good carrier lifetimes from 100 ns up to 1 μ s [58, 59, 61, 63, 64], which results in long carrier diffusion lengths from 100 nm to 1 μ m [60, 62, 65, 66]. Long diffusion lengths of carriers result in efficient collection of charges, since a photo-generated carrier can travel longer distances from the point of generation.

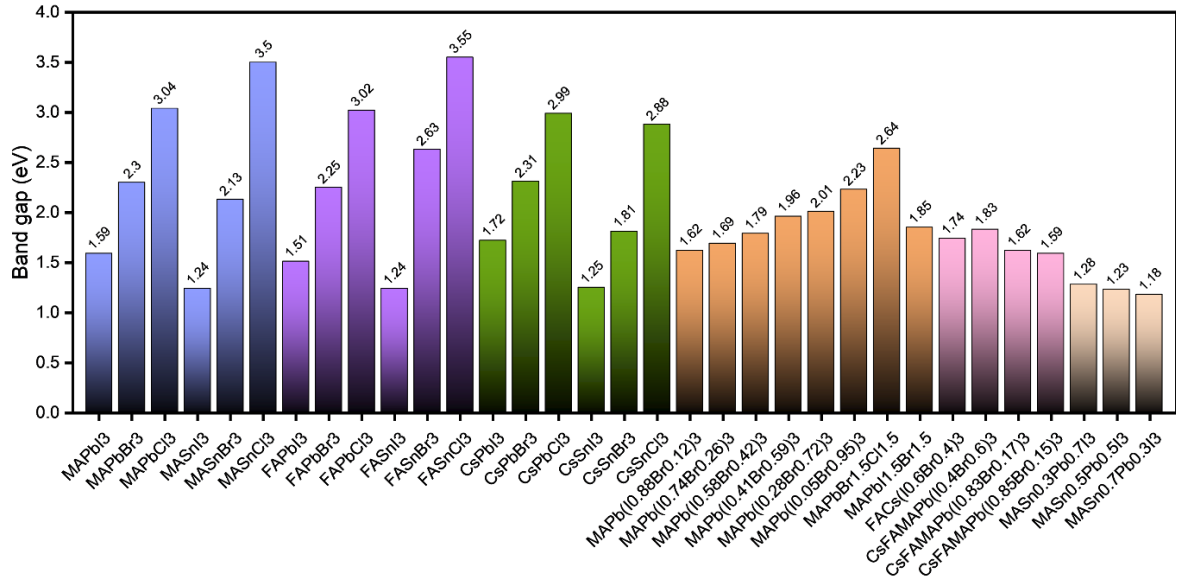


Figure 1.3. Band gap values for perovskites with different compositions. Data acquired from: Tao S. *et al.* for ABX_3 ($A = MA, FA, Cs, B = Pb, Sn, X = I, Br$) perovskites [42]; Kulkarni S. *et al.* [43], Zhang S. *et al.* [44], McMeekin D. *et al.* [45], Abdi-Jalebi M. *et al.* [46], Doherty T. *et al.* [47], Ogomi Y. *et al.* [48], for mixed compositions.

1.3 Perovskite thin film photovoltaics

Perovskite thin film that is sandwiched between other layers of the device, is the basis of perovskite solar cell. These thin films due to remarkable light absorption properties of hybrid perovskites as mentioned in Section 1.2, are usually fabricated with thicknesses of about few hundreds of nanometers, which is sufficient to absorb maximum amount of incident light. In order to fabricate perovskite thin films, various methods are typically used, which will be reviewed below.

1.3.1 Fabrication of perovskite thin films

Among the fabrication methods for hybrid perovskite thin films, the most popular are processing from solution: spin-, spray-, slot-die-, blade-, roll-to-roll-coating, inject printing [67-69] and processing from vapor (co-evaporation, sequential evaporation and flash evaporation) [70, 71]. Other types of hybrid exposure-assisted deposition (CVD, vapor conversion process, gas treated crystallization, soft-cover deposition, polyiodide-assisted conversion, etc.) [72-76] are also used, but are less popular. Spin-coating from solution remains the most common method that so far results in formation of films that demonstrate highest efficiencies in devices.

During the spin-coating, perovskite precursors are dissolved in a mixture of polar aprotic solvents (such as DMF, DMSO or GBL). The mixture is then deposited on a substrate that is spinning with controlled speed, acceleration and duration (see Figure 1.4 for schematic). During the spinning, an anti-solvent (such as chlorobenzene, diethyl ether, toluene, etc.) [77] can be introduced to facilitate solvent removal and initiate crystallization of the perovskite thin film. The nucleation density is important in this process as it pre-determines final size of crystalline grains: larger grains can be formed from lower nucleation density, while higher nucleaction density produces smaller grains. The concentration of precursor solution, evaporation rate of solvent, as well as deposition and annealing conditions, also impact the grain growth and final film coverage. In particular, annealing temperature becomes very important for morphology of the film with optimal temperatures established to be between 80°C and 100°C [78]. In this way, perovskite thin films with thicknesses of few hundreds of nanometers can be fabricated with grain sizes ranging from few hundreds of nanometers to micrometers.

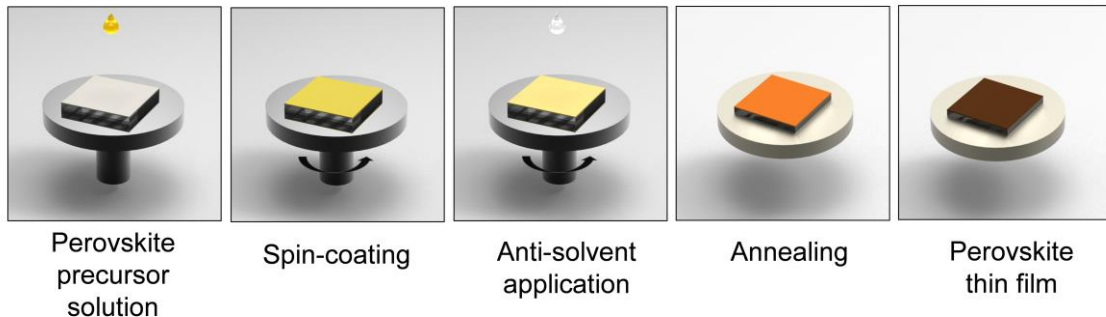


Figure 1.4. Spin-coating of perovskite thin film using anti-solvent treatment.

As has been discussed above, polycrystalline perovskite thin films grow forming grains that typically range in sizes from several hundreds of nanometers to several micrometers. While crystalline grains grow, their termination results in formation of high density of grain boundaries that will vary depending on the grain size. There is a lot of discrepancy in literature regarding the role of grain boundaries. While some reports highlight benign nature of grain boundaries [79-83], others are pointing out relation of grain boundaries to charge carrier trapping due to high concentration of defects [5, 84-88], and improved efficiencies of devices made of large-grain perovskite films [89-93] that have reduced density of grain boundaries. Also, decreased potential barrier [94], enhanced photo-current [95], lower carrier diffusion [96] have been observed at grain boundaries. Additionally, I-rich regions have been identified to be predominantly distributed at grain boundaries [97], while other studies reported grain boundaries to be PbI₂-rich [98]. It remains undetermined what is the exact role of grain boundaries in performance of perovskite thin films, and whether they concentrate centers of non-radiative recombination. In Chapter 3 of this thesis we will shed more light on possible formation of deep level traps at grain boundaries in triple cation mixed halide perovskite thin films.

1.3.2 Perovskite solar cells

Perovskite thin films are basis of perovskite solar cells. However, originally, the field of perovskite photovoltaics began in 2009 with the famous work of Miyasaka group [1] who employed hybrid perovskite as sensitizer on mesoporous TiO₂ electrodes in a typical geometry of a dye-sensitized solar cell (DSSC) (Figure 1.5). A DSSC consists of a layer of mesoporous TiO₂ that is covered with photosensitive molecular dye that absorbs incident light. The cell is then immersed into electrolyte solution together with Pt counter electrode. The working principle of a DSSC is straightforward: (1) incident light is absorbed by the dye; (2) photo-excitation of the dye generates electrons that are then injected to the TiO₂; (3) photo-generated electrons diffuse to the back electrode and then travel to the counter electrode through the external circuit; (4) at the counter electrode, electrons reduce redox mediator in electrolyte and recharge the dye; (5) the redox mediator in electrolyte oxidizes back and diffuses to the counter electrode. The devices in such configuration when used hybrid perovskite as visible-light sensitizer, showed power conversion efficiency of 3.8 % [1], and were reported to efficiently sensitize TiO₂. Only after this it has been realized that solid-state perovskite solar cells were the future direction, and perovskite solar cells in their current planar geometry were developed and started showing higher and higher efficiencies [99], reaching 25.7 % as of now [2].

A typical device structure of perovskite solar cell is shown in Figure 1.6, where perovskite thin film is sandwiched between electron- and hole transporting layers (ETL and HTL, respectively) and conductive contacts (transparent conductive oxide (TCO) and Metal contact). Upon absorption of incident sunlight, electron-hole pairs are generated in perovskite absorber layer (Figure 1.7). Due to the low exciton binding energy in perovskite [100], these bounded electron-hole pairs very quickly dissociate into free carriers, and electrons collected by the electron transport layer, move to the transparent contact, while holes that are collected by the hole transport layer, move to the metal electrode. There is a wide variety of materials that are utilized as efficient electron- and hole transport layers. Among the typical ETLs are meso- TiO₂, compact TiO₂, PCBM, NiO, SnO₂, ZnO, C₆₀, and PEDOT-PSS, spiro-OMeTAD, PTAA for HTLs [101].

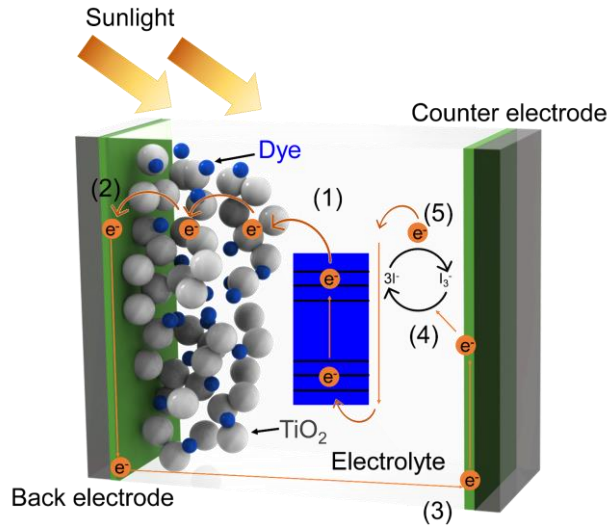


Figure 1.5. Schematic of a dye sensitized solar cell. (1), (2), (3), (4), (5) denote absorption of light by the dye, generation of electrons and their injection to TiO₂, diffusion of electrons to back electrode and to counter electrode, reduction of redox mediator in electrolyte at the counter electrode and recharging of dye, oxidation of redox mediator, respectively.

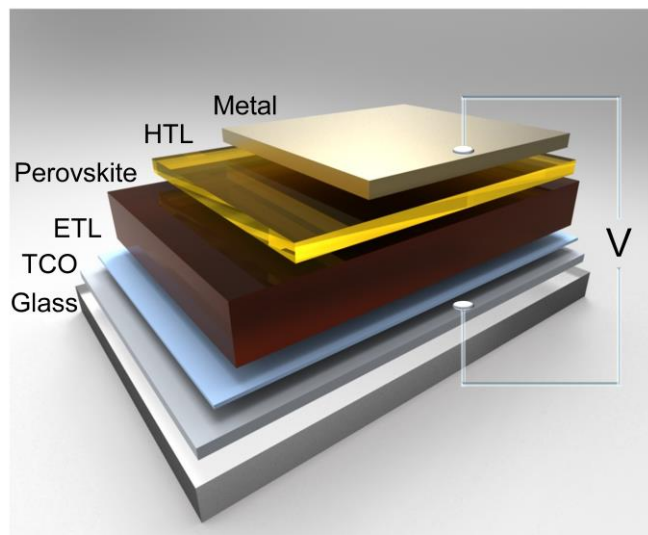


Figure 1.6. Schematic of a typical perovskite solar cell. *ETL*, *HTL*, *TCO* denote electron- and hole transporting layers, and transparent conductive oxide, respectively.

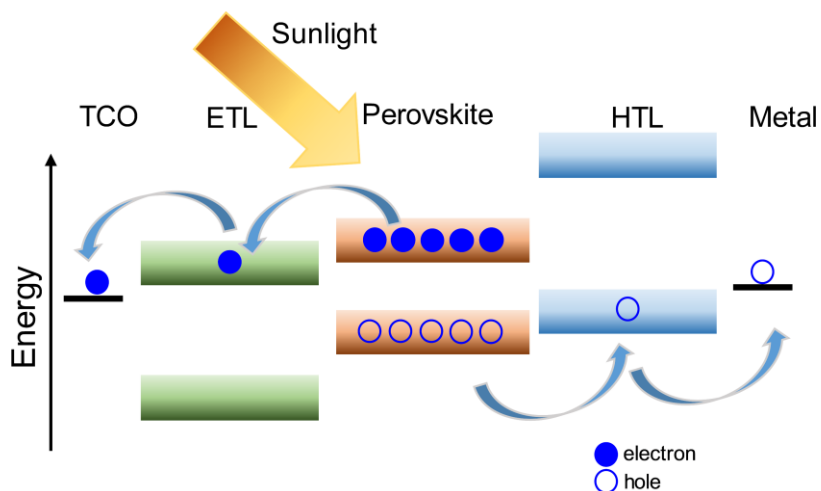


Figure 1.7. Working principle of perovskite solar cell. Upon absorption of sunlight, electrons in perovskite are promoted to higher energy levels, leaving holes behind. Photo-excited electrons move to electron-transport layer (*ETL*) and transparent conductive oxide (*TCO*), while holes move to hole-transporting layer (*HTL*) and are collected at metal electrode.

The fabrication process of perovskite solar cell starts with preparation of substrate. Typically, glass coated with a layer of conductive oxide (ITO or FTO) is used. There are studies that highlighted impact of substrate on quality of fabricated perovskite thin films [102], therefore, careful attention should be paid to this step. The substrates are typically first cleaned and an ETL is deposited. Depending on the type of ETL, it can be fabricated either by solution-based techniques (spin-, spray-coating), or vacuum-based techniques (vacuum sputtering, thermal evaporation). The substrates with deposited ETL might require annealing (*e.g.*, samples with mesoporous TiO_2 as ETL are typically annealed at high temperatures of about 500°C). The substrates with ETL are then subjected to the UV-ozone treatment to make surface more hydrophilic for subsequent spin-coating of perovskite layer. After deposition of perovskite, HTL is introduced by spin-coating, and metallic electrode is evaporated using a mask. The whole process can be as quick as a couple of hours depending on the preparation methods of choice. Spin-coating is a relatively fast fabrication method, however one is required to have a lot of practice in order to fabricate reproducible and reliable thin films and devices. Therefore, when it comes to assessment of performance of prepared solar cells, it is advised to make judgments across multiple devices, and not to rely on the output of a single device [103].

1.3.3 Performance of perovskite solar cells

Before proceeding with discussing performance of perovskite photovoltaics, let us review some important performance parameters in photovoltaic devices.

For a solar cell to be a good photo-converter, it should be made of a semiconducting material with an energy gap. The light absorption properties of this material should be superior, which will guarantee efficient absorption of incident photons and generation of charge carriers. This semiconductor should be contacted with other materials to achieve efficient charge separation and collection. For an ideal device, the losses occurring due to non-radiative recombination of photo-generated carriers at defects and impurities, should be minimized for all the layers and their interfaces with contacts.

The two important parameters that determine performance of the operating solar cell, are open circuit voltage (V_{oc}) and short circuit current (I_{sc}) [104]. The short circuit current depends on the area of solar cell. To remove this dependence, it is commonly represented through short-circuit current density (J_{sc}). V_{oc} develops when solar cell is switched on by light, but the terminals remain isolated, while J_{sc} is the current drawn when the terminals are connected together. Solar cell operates between 0 and V_{oc} and delivers largest current equal to J_{sc} . The photocurrent (J_{sc}) of the solar cell depends on the incident light and is defined through the quantum efficiency – probability that an incident photon will produce an electron to the external circuit. The V_{oc} depends on the saturation current and light-generated current of the solar cell (equation 1.3 – 1.5). The V_{oc} increases as the band gap E_g of the light absorbing material increases. Generally speaking, the lower the band gap of absorbing material, the more photons can be absorbed due to the shape of solar spectrum. However, lower band gap at the same time implies a lower V_{oc} [104]. Therefore, materials with optimum band gap should be considered according to specific application (e.g., single junction or tandem photovoltaics).

The detailed balance principle introduced by W. Shockley and H. Queisser in 1961 [105] for absorbed and emitted radiation, is putting unavoidable constraints on efficiency of solar cells by stating that it is impossible to convert 100 % of the incident light into electricity. The losses that are considered, arise from either not absorbed or thermalized photons that will not contribute to the photon-to-electron conversion in a solar cell. For example, for a single-junction device made from an “ideal” material with band gap of 1.4 eV, the detailed balance approximation gives limiting efficiency of about 33.7 % in a non-concentrated light. Among the strategies to overcome the Shockley-Queisser limit, are (i) concentration of incident solar light [106] when incident light is focused or guided by an optical element such that a high intensity beam shines on a small solar cell, (ii) use of tandem devices to cover as much of the solar spectrum as possible [107, 108], (iii) photon up conversion to utilize the below-band gap photons [109, 110], and many more. For perovskite devices, tandem configurations with Si [111-114], low-band gap perovskite [115, 116] or even organic photovoltaic devices [117, 118] become more and more popular, and will very likely occupy a substantial niche of application of perovskite photovoltaics in the near future.

The current voltage response of a solar cell is described with a current-voltage characteristic. A typical current-voltage characteristic of an ideal solar cell is shown in Figure 1.8, where J_{sc} and V_{oc} represent short circuit current and open circuit voltage, and the product of J_m and V_m gives maximum power point (P_m) at which device should be operated to achieve maximum PCE. The fill factor (FF) is then determined according to the Equation 1.3, and describes the “squareness”

of the J - V curve. Typically, the closer the FF value to 1, the less losses a solar cell is experiencing.

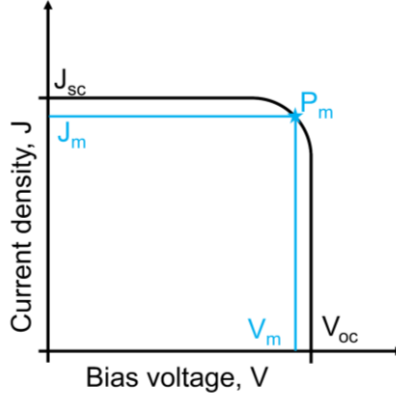


Figure 1.8. Current voltage characteristic of an ideal solar cell. J_m , V_m , P_m , J_{sc} , V_{oc} denote maximum current, maximum voltage, maximum power point, short circuit current and open circuit voltage, respectively.

The PCE (η) of the solar cell is determined as a ratio of the output power density delivered by the solar cell at operating point and input power density of the incident sun light P_s (Equation 1.4). Using FF, efficiency is related to the V_{oc} and J_{sc} (Equation 1.5).

$$FF = \frac{J_m V_m}{J_{sc} V_{oc}} \quad (1.3)$$

$$\eta = \frac{J_m V_m}{P_s} \quad (1.4)$$

$$\eta = \frac{J_{sc} V_{oc} FF}{P_s} \quad (1.5)$$

For a real solar cell, the J - V curve approaches the one of an ideal cell, however, the performance is influenced by parasitic resistances called series (R_s) and shunt (R_{sh}) resistances that arise due to contacts and current leakage around the edges of the device and between contacts.

The superior light absorption abilities of perovskites, imply that a fraction of solar light that the material absorbs, should be efficiently converted to charge carriers. However, the absorption coefficient as well as band gap, will vary for different compositions of perovskites. Therefore, depending on application, one should carefully select the composition of perovskite absorber. For example, devices with one of the highest PCE values as of now (exceeding 20 %) are fabricated using perovskites with mixed compositions, having three ions as A-site cation (MA, FA and Cs) and two halides as X-site anion (I, Br) [119, 120]. These devices have high V_{oc} values (~ 1.1 V– 1.2 V) due to relatively large band gap of perovskite absorber (~ 1.6 eV – 1.7 eV), and efficiently capture reasonable amount of solar light, resulting in high J_{sc} (~ 17 mA/cm² – 22 mA/cm²). The compositions yielding lower band gaps, such as FA-based, I-only perovskites [121], have also demonstrated high PCEs given their high values of J_{sc} , and have potential for application in single-junction or perovskite-perovskite tandem solar cells. Br-rich

perovskite absorbers are popular for applications in tandem devices where utilization of wide-band gap semiconductors is essential [44, 122, 123].

Even though hybrid perovskite solar cells have demonstrated a remarkable increase in efficiency over the past decade and are approaching efficiencies of conventional Si-based technologies that have been developing for more than 50 years now, perovskite solar cells still remain below the theoretically predicted values for PCE [10]. Moreover, over the recent years the efficiency values have been increasing rather slowly with each benchmark being slightly higher than previous, usually as a result of passivation of absorber layer or doping of charge transport layers [124-127]. This means that in parallel to trying out various strategies to polish up the efficiency, along with exploring the wide variety of material compositions and forms that hybrid perovskite family has to offer (such as 2D perovskite films [128], nanocrystals [129], single crystals [130]), we must turn into investigation of fundamental processes that limit the device performance. This will be the key to overcome any efficiency limitations and will provide a platform to further implement these materials for large scale, flexible and tandem applications.

1.4 Limitations of perovskite photovoltaics

The viability of photovoltaic devices typically includes such parameters as power conversion efficiency, long-term stability and ease of fabrication [131]. While the last condition can be somewhat satisfied for perovskites with a wide variety of low-temperature and low-cost fabrication methods, these preparation routes typically result in device efficiencies that still require improvement, meaning that some fabrication parameters need to be changed in order to improve the PCE. Which exact parameters to tweak is not so obvious and therefore requires a detailed study of factors that are predicted to limit the PCE from various perspectives. Some of these factors, in particular presence of charge trapping defects in perovskite absorber layer and their impact on device efficiency, will be discussed further in this thesis. The outcome of this study will add to the knowledge base and we hope will facilitate future development of immediate working tools to improve performance of perovskite solar cells. The long-term stability of perovskite solar cells remains outside of the scope of this thesis, however, has been approached by us via collaborative work with colleagues from Stranks Lab at the University of Cambridge who have pursued this direction thoroughly, with us participating in important experimental assessments [132].

Since the perovskite thin films have been first employed in solar cells, the number of publications on perovskite photovoltaic devices has been increasing rapidly every year and the “perovskite fever” began. When typing “hybrid perovskite” in a Web of Science search engine, over 9,000 results are generated as of today. Most of these works report on various fabrication approaches or film passivation methods, many of which led to new benchmarks in performance of perovskite solar cells. However, in parallel to suggesting and employing potential strategies to improve efficiencies - which often times do not deeply investigate on the reasons why they appeared successful, but rather report the improved performance – it is critically important to understand the underlying limitations of perovskites and develop meaningful and successful strategies to overcome them based on this knowledge. Especially important are processes that occur on micro- or nanoscale – or on the level of grains in polycrystalline perovskite films [4], where the variations of optoelectronic properties, such as in photoluminescence intensity [5, 6], local strain [133, 134], composition [135-137] have been observed and related to the film performance.

To understand how the research of hybrid perovskite thin films on grain level has been developing over years, we analyzed the number of articles published in peer reviewed journals in time frame from 2009 to 2021 (Figure 1.9, data acquired from [138-141] for 2014, [5, 79, 142-156] for 2015, [82, 136, 157-178] for 2016, [7, 80, 95, 98, 179-206] for 2017, [46, 96, 207-236] for 2018, [133, 134, 237-256] for 2019, [47, 94, 257-276] for 2020, [83, 114, 137, 277-297] for 2021). The articles reporting on layered 2D perovskites, perovskite nanostructures, single crystals, as well as works reporting efficiency-only and review papers have been excluded from the search. Thus, only the works covering various nano- and microscale investigation approaches applied to hybrid perovskite thin films have been accounted for in the search. When analyzing such reports, we found that pronounced research in this area started around 2015 - 2016. During this time, device efficiencies have already approached 20 % and initial rapid increase in efficiency began to slow down from approximately (3 - 4) % to about (1 - 2) % PCE improvement per year. Therefore, it was a high time to begin comprehensive assessment of limitations of perovskite photovoltaics on different length scales with the aim to improve efficiencies even further by overcoming crucial limitations. Similarly, the work on this thesis

has started with the goal to contribute to understanding of nano- and microscale processes that are acting as obstacles for perovskite photovoltaics from reaching their ideal performances. In our case, we have chosen a powerful approach that allowed us to directly probe the sites of poor performance. More details will be provided later on in following chapters of this thesis.

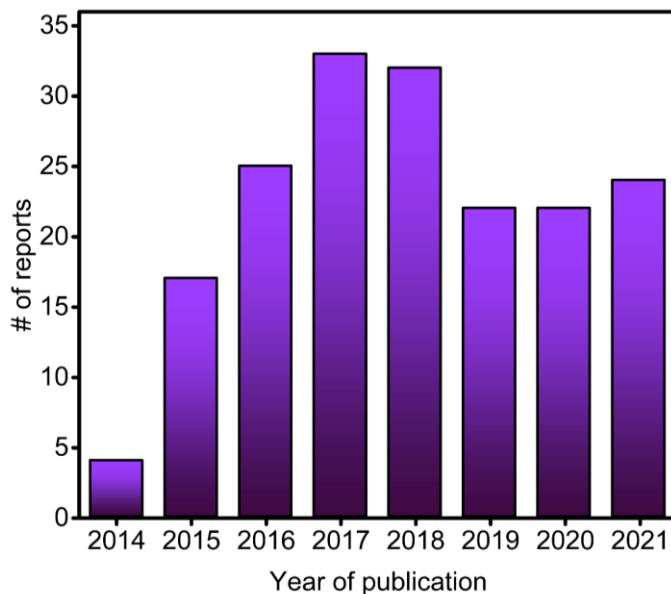


Figure 1.9. Number of literature reports that researched properties of hybrid perovskite thin films on micro- and nanoscale (shown in time frame from 2014 to 2021). Data acquired from [5, 7, 46, 47, 79, 80, 82, 83, 94-96, 98, 114, 133, 134, 136-297].

1.4.1 Defects in hybrid halide perovskites

Hybrid perovskite thin films are commonly processed using low-temperature solution-based methods that are known to result in formation of unintentional defects and impact performance of perovskite solar cells. Even films that are used to fabricate devices with high efficiencies, contain non-negligible amount of defects that result in inability of perovskite devices to reach their thermodynamically predicted efficiency limits [9, 13]. Typically, defects in semiconductors represent interruptions to perfect arrangement of atoms in crystal lattice. They can appear in a form of point- (vacancies, interstitial atoms, anti-site substitutions) or higher dimensional defects (dislocations, stacking faults, precipitates, grain boundaries). Energetically, defects can be categorized into shallow level- that open states closer to the band edges, or deep level defects that lay in the mid gap. Shallow defects in perovskites can cause doping, however, due to their fast charge trapping-de-trapping nature, they typically do not act as centers of non-radiative recombination [18]. In turn, deep level defects are known to participate in charge carrier trapping and impact charge generation, separation and collection at contacts [15, 17, 87].

According to theoretical works that have calculated the energy-level positions of some common point defects that can form in hybrid perovskites, deep level defect states can be opened by I interstitials (I_i), Pb vacancies (V_{Pb}) [15, 20, 21] and various anti-site occupations (Pb_i , I_{Pb}) [19,

298]. In addition to common point defects that are usually heavily discussed from perspective of limiting perovskite efficiency, we cannot exclude formation of higher dimensional defects, such as twinning defects, stacking faults or dislocations, and their potential impacts on performance of the film. Given the high sensitivity of perovskite films to electron beam probes that are typically used to visualize structural defects, the relationship between presence of specific types of defects and perovskite performance remain poorly understood. Only recent works employing mild doses of electron beam probes in transmission electron microscopy, began showing very promising results in this direction [227, 269, 287, 299]. Given the variety of defects that can form in perovskite thin films, one important area of research is to understand and control these defects.

1.4.2 Defect-induced limitations in perovskite thin films

One of the unfavorable effects that deep level defects can introduce in perovskite thin films, is trapping of photo-excited charges. This means that upon photoexcitation, a portion of electrons or holes will not reach the charge transport layers and contacts, but will be trapped at defective sites. This leads to non-radiative recombination of trapped charges and directly reduces efficiency of devices. Moreover, deep level defects can impact band alignment at interfaces with charge transport layers, or create obstacles for charge transport, as they can act as scattering centers for charges that are accelerated by the electric field.

When studying defect-induced limitations, it is important to use appropriate tools that allow to probe them directly. One common approach to investigate non-radiative recombination is to employ time-resolved photoluminescence spectroscopy (TR-PL) [5, 7, 14, 300-302]. In particular, TR-PL accounts for both radiative and non-radiative recombination, and fitting of TR-PL decay dynamics, allows to estimate both. If extend this model even further, third-order processes such as Auger recombination should be also considered. The non-radiative time constants can be extracted and compared for different films to estimate the contributions from defects. One challenge of this method, similarly as for many spectroscopy tools, is spatially-averaged nature of results. Considering that perovskite thin films have polycrystalline nature, it is useful to employ tools with good level of spatial resolution to be able to compare different regions of the film, *e.g.*, grains *versus* grain boundaries.

When employing microscopy techniques for perovskite films, inhomogeneous photoluminescence intensity, as well as non-radiative decay parameters were found. For example, works by deQuilettes *et al.* [5-7, 157] combining photoluminescence- and scanning electron microscopies, first highlighted that perovskite films contain “bright” grains with good photoluminescence and “dark” grains showing poor photoluminescence intensity. Such spatially inhomogeneous behavior of perovskite films implies the presence of hidden centers of non-radiative recombination that occur on grain level (nano- or microscale) and contribute to local limitations of perovskite performance.

Furthermore, aside from inhomogeneous photoluminescence, spatial heterogeneities of other properties such as photo-response [164], open circuit voltage [184], contact potential difference [248, 255], crystallographic orientation [134], composition [135, 136, 238, 251], have also been reported for hybrid perovskite thin films. Many of these have been related either to presence of charge trapping defects, or were explained via other mechanisms such as ion migration, phase segregation, etc. For example, non-radiative defect-mediated photoluminescence losses have

been correlated with presence of local strain in perovskite thin films [133]. All this suggests that in order to understand the limitations of perovskite thin films, one needs to zoom in to micro- or even nanoscale and investigate defect-mediated processes. Moreover, given the ultrafast nature of charge trapping by deep level defects, having opportunity to employ time-resolved measurements, becomes equally as important. Therefore, when designing experimental methodologies to characterize defects in perovskites, both high levels of spatial and temporal resolutions are required.

To study defects in hybrid perovskites with both spatial and temporal resolution, in our group, we have been developing application of time-resolved photoemission electron microscopy (TR-PEEM) [47, 303]. TR-PEEM benefits from spatial resolution of photoemission electron microscope (about 20 nanometers) and temporal resolution of optical pulses (about a few hundreds of femtoseconds) that are used to create photo-excited state and monitor the response of selected energy states in material (more details in Chapter 2).

By employing PEEM, we have previously shown that we were capable of imaging spatial distribution of defect states in perovskite thin films as nanoscale clusters [47, 303]. We have also correlated them with local photoluminescence losses and found general trends in trapping of photo-excited charges at these nanoscale defect sites. However, much remains unknown about these defects. In particular, more work is required to determine location of the defects with respect to surface microstructure, to categorize defects according to their types, to understand their exact roles in charge trapping and finally, to understand their response to passivation strategies. Such comprehensive assessment is important to design legitimate strategies to engineer the undesired defects and to improve the viability of perovskite solar cells.

1.5. Thesis objectives and overviews

The main objectives of this thesis are: (i) to visualize nanoscale defects in polycrystalline hybrid perovskite thin films and to identify their formation sites; (ii) to categorize the visualized defects based on their morphological arrangement and spectroscopic signature into different types; (iii) to probe the spatio-temporal charge carrier trapping dynamics of different defect types upon photo-excitation, and relate this behavior to the role of defects in performance of perovskite thin films; (iv) to directly probe how specific strategies known to improve performance of perovskites, impact nanoscale defects and their charge trapping dynamics.

In order to achieve goals of this thesis, we utilized time-resolved photoemission electron microscopy as a main characterization tool, and supported our work with the help of supplemental solid state characterization microscopy techniques, such as scanning electron-, atomic force-, and photoluminescence microscopies.

In Chapter 3, we provide detailed description about imaging of the spatial distribution of nanoscale defects with photoemission electron microscopy. We found that the defects in triple cation mixed halide perovskite thin films ranged in sizes from few tens to few hundreds of nanometers. We also observed that these defects had very different spatial arrangement with respect to surface microstructure. The smallest defects of few tens of nanometers in sizes, were predominantly distributed at grain boundaries, while larger ones of few hundreds of nanometers in sizes, were associated with entire grains. In this Chapter we started classifying defects into different types based on their relation to surface microstructure.

In Chapter 4, to further define different types of visualized defects, we employed energy-resolved imaging with PEEM. This allowed to plot photoelectron spectra for individual defects and estimate their energy level positions and variation of work function at defective sites as compared to pristine regions. By relating spectral characteristics and spatial arrangement of defects, we were able to further categorize the observed defects.

In Chapter 5, in order to understand behavior of nanoscale defects upon photoexcitation, we employed time-resolved PEEM. TR-PEEM allowed to visualize charge carrier trapping at defective sites in space and monitor the sub-nanosecond trapping dynamics in time. We found that grain boundary and one type of intra-grain defects participated in trapping of photo-excited holes, while another type of intra-grain defects, was relatively benign and did not trap charges when photo-exciting perovskite. Moreover, the types of defects that showed trapping behavior, had very different trapping dynamics, which implied presence of different mechanisms for charge trapping for each defect type.

Finally, Chapter 6 describes how these different types of defects can be impacted when subjected to treatments known to improve performance of perovskite films. After exposing films to controlled amounts of oxygen under illumination, we found that even upon very mild treatments, trapping by the grain boundary defects was suppressed, while intra-grain defects remained largely unaffected. Additionally, we found that upon mixing specific additives to perovskite precursor solution, such as potassium iodide, some of the defects can be effectively passivated. We concluded, that given the varied response of defects to treatments, it is likely that a combination of approaches might be required to engineer defects, including careful control of film crystallization and application of targeted post-treatment strategies.

Through careful study and assessment, the work done in this thesis provides detailed knowledge about the nanoscale defects in perovskite thin films and their role in film performance. We hope that our results will benefit perovskite photovoltaic community and will provide more insights into improving film fabrication methodologies as well as other approaches to eliminate formation of undesired defects in hybrid perovskite thin films. We hope our work will help enhance viability of perovskite photovoltaics for successful commercialization in the near future.

Chapter 2

Time-resolved Photoemission Electron Microscopy

2.1. Abstract

In order to achieve goals of this thesis, we utilized time-resolved photoemission electron microscopy as a main characterization tool. PEEM allows us to visualize electrons photo-emitted from various occupied states in material. When coupled with time-resolution of optical pump-probe experiment, PEEM allows us to trace the evolution of photo-excited charges in space and time. In this chapter, we will introduce time-resolved PEEM (TR-PEEM) as a suitable technique for studying semiconducting thin film samples. In Section 2.2, we will discuss general aspects of our experimental set-up, main components of PEEM, optical set-up for generation of ultraviolet light required for PEEM experiments. In Sections 2.3 and 2.4, we will cover design and operation of TR-PEEM experiment and interpretation of TR-PEEM signal.

2.2. Photoemission electron microscopy

Photoemission electron microscopy is a powerful technique that can be utilized to characterize electronic states of metallic and semiconducting materials [304]. In PEEM, electrons are photo-emitted from sample surface with incident ultraviolet or X-ray photons and are imaged with electron optics of the microscope. PEEM is a surface-sensitive technique capable of studying properties of materials with high spatial and energy resolution. Nowadays, PEEM instruments are employed to study semiconductors [305-310], plasmonic surfaces [311-315], various magnetic materials [316-318] and even biological samples [319, 320]. Adding temporal resolution to PEEM experiments, opened a new field of time-resolved PEEM which allowed to visualize the excited state dynamics in space and time [306, 308, 310, 321].

2.2.1. General aspects of photoemission

The basic principle of PEEM operation is photoelectric effect [304]. The photoelectric effect was discovered back in late 1880s by Heinrich Rudolf Hertz and since then the knowledge was gradually expanding and led to a Nobel Prize awarded to Albert Einstein in 1921. Photoelectric effect occurs when electrons are liberated from the surface of material upon shining light of energy that is enough to overcome material's work function (Figure 2.1a). In particular, electrons that populate core levels and valence states are promoted to the free electron states in the vacuum level upon absorption of UV radiation, as shown in Figure 2.1b. Nowadays, photoelectric effect finds application in electronic devices (photodiodes, etc.) and also in electron microscopy such as PEEM, XPEEM and in spectroscopy including XPS and UPS. In particular, when illuminating material with photons of high energies one can obtain compositional information about the material [322].

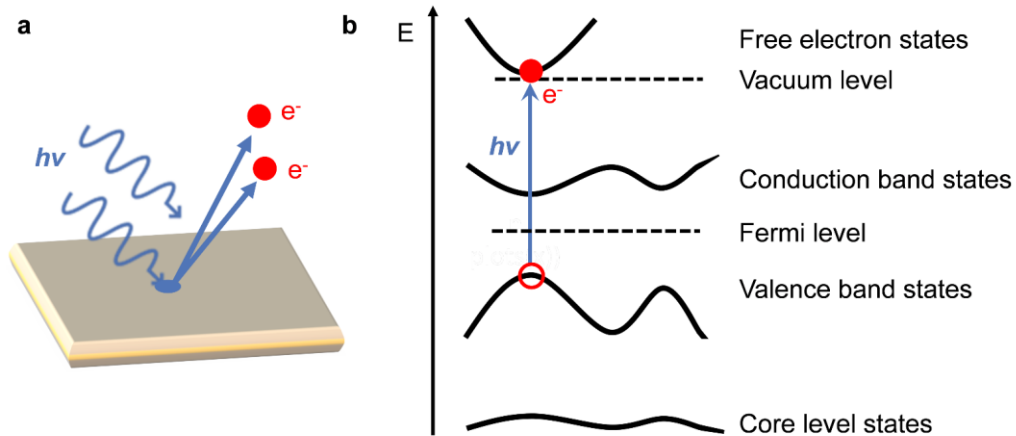


Figure 2.1. Diagram of photo-emission process. (a) UV light ($h\nu$) causes photo-emission of electrons (e^-) from the surface of a solid (photoelectric effect). (b) Upon absorption of UV photons, electrons (filled red circle) are promoted from the valence band, conduction band and core level states to free electron states above the vacuum level, leaving holes (hollow red circle) behind.

Photoemission from solids is typically described with a three-step model that was first introduced by C. Berglund and W. Spicer [323] (Figure 2.2). Those three steps are: (i) photoexcitation of an electron from the solid; (ii) propagation of the photo-excited electron to the surface; (iii) escape of the electron from the solid. For each of these steps strict conditions should be satisfied in order for the photoemission event to be successful. Step (i) can be described by quantum - mechanical selection rules and requires transition (with transition probability ω) between initial state (Bloch state of the solid Ψ_i) and final state (free electron state Ψ_f) to be favorable (Equation 2.1). During the (ii) step, when photo-excited electrons propagate to the surface, in order to be photo-emitted, electrons need to overcome scattering and collisions with other particles in the solid. The step (iii) for example, demands conservation of parallel component of momentum vector $k_{||}$, and electrons also need to overcome work function of the material. This three step model is a commonly used approximation to explain complex photoemission processes to large audience in an intuitive manner. The description of a more “correct and accurate” yet far more complicated one-step model, that introduces a damped final state, can be found in the book by S. Hüfner [324].

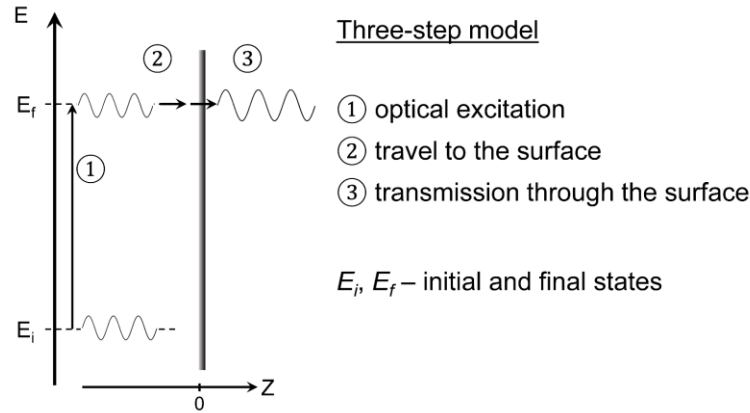


Figure 2.2. Three-step model of photoemission. Adapted from Hüfner S. “Photoelectron spectroscopy: principles and applications” [324].

$$\omega \propto \frac{2\pi}{\hbar} |\langle \Psi_f | \Delta | \Psi_i \rangle|^2 \delta(E_f - E_i - \hbar\nu) \quad (2.1)$$

The electrons that escape from the sample surface have kinetic energies (E_{kin}) defined according to the (Equation 2.2), where E_B is the binding energy of the photo-emitted electron, Φ is a work function of the material and $h\nu$ denotes incident photon energy.

$$E_{kin} = h\nu - E_B - \Phi \quad (2.2)$$

When performing photoelectron spectroscopy, kinetic energies of photo-emitted electrons are being recorded, which allows to extract their binding energies. In this way, one can obtain chemical information about material. Apart from measuring kinetic energies, by resolving the emission angle of photo-emitted electrons, one can employ technique called angle-resolved photoemission spectroscopy (ARPES) [325] to map electronic band structure of material.

2.2.2. Photoemission electron microscope

The development of photoemission electron microscopes started in 1930s with the work of E. Brüche, who designed the first system for imaging with photoelectrons, known as the first PEEM [326]. These first microscopes were used to study metallic and mineral samples. Such systems operated at poor vacuum conditions and suffered from sample contamination. This type of PEEM was followed by development of ultrahigh vacuum (UHV) microscopes. UHV PEEM was developed in 1970s with efforts of surface scientists [327]. This generation of PEEM allowed to reach vacuum of about 10^{-9} mbar, which prevented sample contamination and condensation. This improvement allowed to study adsorption of oxygen on metallic surfaces, growth of metals on polycrystalline substrates, chemical reactions on metal surfaces, as well as doping of semiconductors [328-330]. Since then the development of PEEM progressed to include different imaging regimes by introducing sets of electromagnetic lenses and a hemispherical energy analyzer [304, 327]. A modern spectroscopic PEEM (SPELEEM), which operates in imaging and spectroscopy modes, has been around since the end of 1980s. These instruments were used with synchrotron radiation to produce images of core and secondary photoelectrons, as well as to carry out micro-photoelectron diffraction (μ PED) and micro-XPS (μ XPS) experiments. In 2000s, the original spectroscopic SPELEEM was commercialized by Elmitec. Since then, modernized PEEM instruments, are used in various ways to realize XPEEM, μ PES, μ XPS and in combination with LEEM to study metallic, semiconducting, and even amorphous samples.

The work in this thesis has been done using SPELEEM III microscope manufactured by Elmitec. The schematic of this instrument is shown in Figure 2.3. A typical microscope consists of a load lock, preparation chamber, main UHV chamber, illuminating-, imaging- and projective electron optics. The main chamber of the microscope is kept under high vacuum ($10^{-10} - 10^{-11}$ Torr or better) and is connected with preparation chamber via an UHV gate valve. The sample is transferred between the chambers using a transfer arm. The preparation chamber is typically used for sample storage and preparation of sample for the PEEM measurements, such as heating or cleaving. SPELEEM III is also equipped with an electron gun for operation in low energy electron microscopy (LEEM) mode. When operating in LEEM mode, electron beam is directed to the sample through the beam separator that separates the incoming incident and outgoing backscattered electrons. In PEEM mode, an external UV photon beam that is coupled through an UV viewport, hits the sample under grazing angle. The photo-emitted electrons are then collected by a magnetic objective lens and directed to the imaging column of the microscope. In order to obtain high spatial resolution, high potential difference of 20 kV is applied between the sample and objective to accelerate photo-emitted electrons into the objective lens. After passing through the imaging optics, photo-emitted electrons enter hemispherical energy analyzer that disperses electrons depending on their kinetic energies. Finally, after the energy analyzer, electrons reach projective system and image detector (microchannel plate, phosphorous screen and camera). In this way, one can acquire energy-resolved images of sample with spatial resolution of about 20 nm and measure photoelectron spectra with energy resolution of about 125 meV.

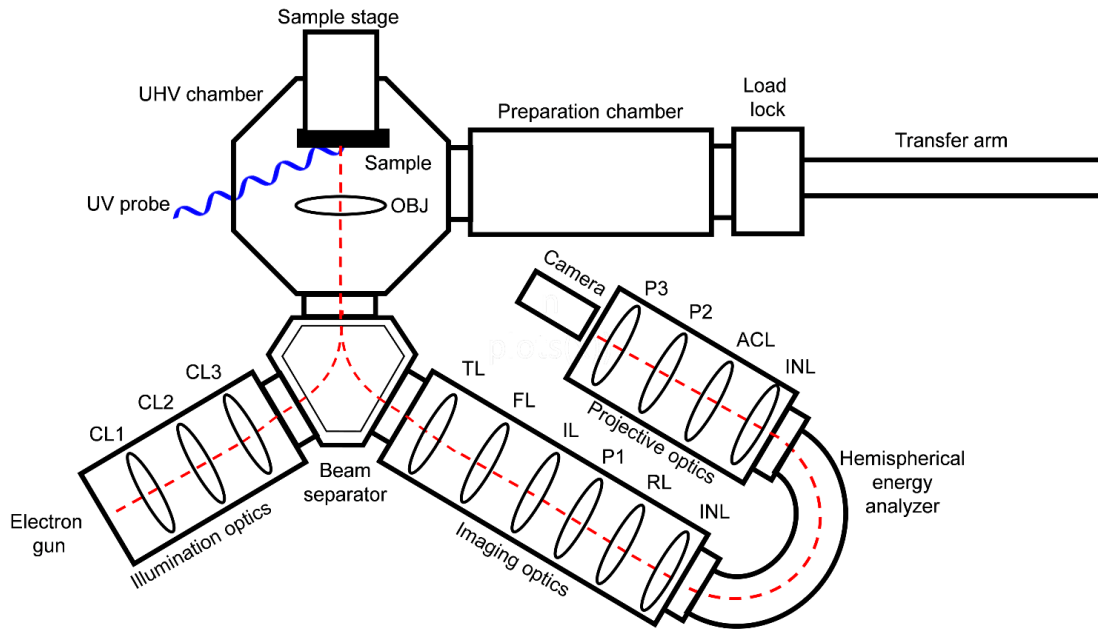


Figure 2.3. Diagram of photoemission electron microscope. Electro-magnetic lenses are marked with ellipses. *CL1*, *CL2*, *CL3*, *OBJ*, *TL*, *FL*, *IL*, *P1*, *RL*, *INL*, *ACL*, *P2*, *P3* denote Condenser lens 1, Condenser lens 2, Condenser lens 3, Objective lens, Transfer lens, Field lens, Illumination lens, Projective lens 1, Retarding lens, Intermediate lens, Acceleration lens, Projective lens 2, Projective lens 3.

PEEM contains many different apertures and slits that can be inserted in electron beam path. Illumination aperture is used to limit the electron beam size when operating in LEEM mode. Field limiting (selected area) aperture allows to limit the size of the image in the energy analyzer by selecting small region of the sample surface. This becomes important for angle-resolved spectroscopy of small samples, and also allows to improve energy resolution. Contrast (diffraction) aperture serves to improve the contrast and spatial resolution. This is a small-opening that blocks electrons photo-emitted at large angles, and prevents them from contributing to aberrations. Energy slit is used for photoemission spectroscopy and serves to select electrons within a limited energy window. By scanning the whole energy spectrum of photo-emitted electrons through the slit, we can collect energy-resolved images.

The typical modes of operation of the PEEM, are shown in Figure 2.4. Among them are: (i) imaging mode, (ii) spectroscopy mode and (iii) diffraction mode. The imaging mode allows to produce an image from photo-emitted electrons. By using spectroscopy mode, one can record energy-resolved images and collect photoelectron spectra. Finally, the diffraction mode is used to collect diffraction pattern from an area of interest. This mode requires the use electron gun as illumination source. Using a combination of different modes, other type of experiment such as angle-resolved photoemission spectroscopy can be realized. ARPES allows to visualize electronic band structure by recording the emission angles and kinetic energies of photo-emitted electrons. The work in this thesis heavily relies on a part of these capabilities, in particular, on PEEM imaging and photoelectron spectroscopy.

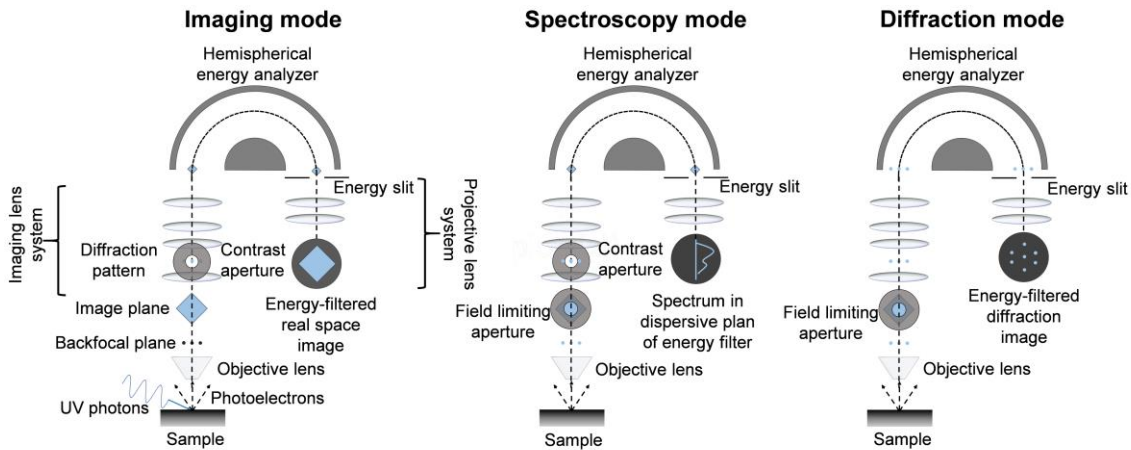


Figure 2.4. Typical working modes of LEEM/PEEM photoemission electron microscope (adapted from Menteş T. and Locatelli A. [325]).

2.2.3. UV photon sources

In PEEM, UV photons are typically utilized to liberate electrons from the sample surface. The energy of these photons should be sufficient to overcome work function threshold of materials (at least 4 eV for most materials). The most commonly used laboratory based photon sources for PEEM are mercury- (6.7 eV or 4.9 eV), deuterium- (10 eV) or He lamps (21.22 eV or 40.81 eV). When used with synchrotron radiation with X-ray photons of much higher energies, XPEEM can be realized to photo-emit core-level electrons and obtain chemical information about the sample.

Another source of UV light are pulsed lasers. Pulsed laser UV light sources were introduced in 1980s by Jones *et al.* [331] who used a Q-switched Nd:YAG laser (1064 nm) and produced fourth harmonic radiation of 4.66 eV with nonlinear crystals. Their laser system operated in the kHz regime producing high peak power pulses. It was later on shown that high laser power decreases image resolution in PEEM due to space charge effects [332, 333]. Therefore, MHz laser systems with lower pulse energies have been reported to be better for PEEM imaging due to minimized space charge effects [304].

To generate UV probe photons for PEEM experiments in this thesis, we employed non-linear frequency conversion of fundamental output (800 nm) of a 4 MHz Ti:Sapphire laser (Femto Lasers XL:650) with pulse energy of 650 nJ and pulse duration of 45 fs. Via frequency mixing using nonlinear BBO crystals [308, 334], we generated about 5 mW of third (266 nm or 4.65 eV) and about 0.5 mW of fourth (200 nm or 6.2 eV) harmonics by sending 500 mW of fundamental 800 nm. Such amounts of generated harmonics were sufficient for actual PEEM experiments, as will be discussed in Chapter 3. The schematic of the optical set-up is shown in Figure 2.5. The generated UV photon beam was coupled to the PEEM via a fused silica window. The design of the microscope allows to send the laser beam under a grazing angle θ of about 17° for our setup. The reflected beam after the sample, passes through the window on opposite side and is blocked by a beam dump.

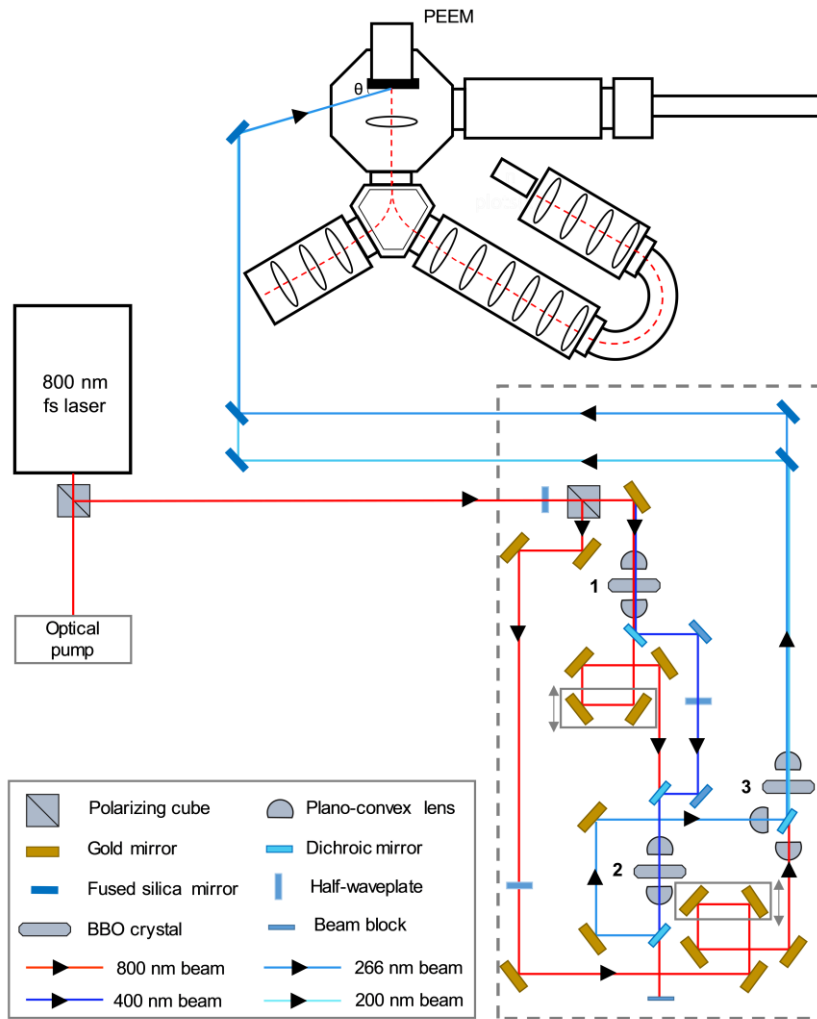


Figure 2.5. Diagram of PEEM experiment. Output beam of a femtosecond pulsed laser source enters the UV light generation set-up (highlighted with grey dashed line). 266 nm and 200 nm light is generated by frequency conversion using nonlinear BBO crystals (1, 2 and 3). The UV beams are coupled to the PEEM through the side window.

On a side note, early on, at the beginning of the work on this thesis, we have also employed similar design to generate 266 nm light via tripling fundamental output of an 80 MHz pulsed Ti:Sapphire laser system (Spectra Physics MaiTai) with pulse energy of 31 nJ. In order to induce nonlinear processes for frequency up-conversion with low pulse energy laser systems, it is important to achieve tight focusing and minimize losses via employing of achromatic lenses mounted on high precision lens mounts. Although it was challenging to generate 200 nm light, we have successfully generated 266 nm light with 80 MHz laser system.

2.2.4. PEEM resolution and probe depth

The PEEM that was used in this thesis allows imaging with photoelectrons with spatial resolution below 20 nm. The spatial resolution will heavily depend on the sample surface, alignment of the microscope, the use of apertures and, importantly, on the dose of incident UV light. For example, for XPEEM experiments, the spatial resolution can be as good as few tens of nanometers due to high energy of the pulsed probe photons [335]. We used 84% 16% method to estimate the resolution of high quality PEEM images obtained in this work and found that for the best alignment with contrast aperture, we were able to achieve about 18 nm spatial resolution for perovskite samples (Figure 2.6a). PEEM image with poor spatial resolution (~ 46 nm) due to space charge effects and poor alignment is shown in Figure 2.6b for comparison.

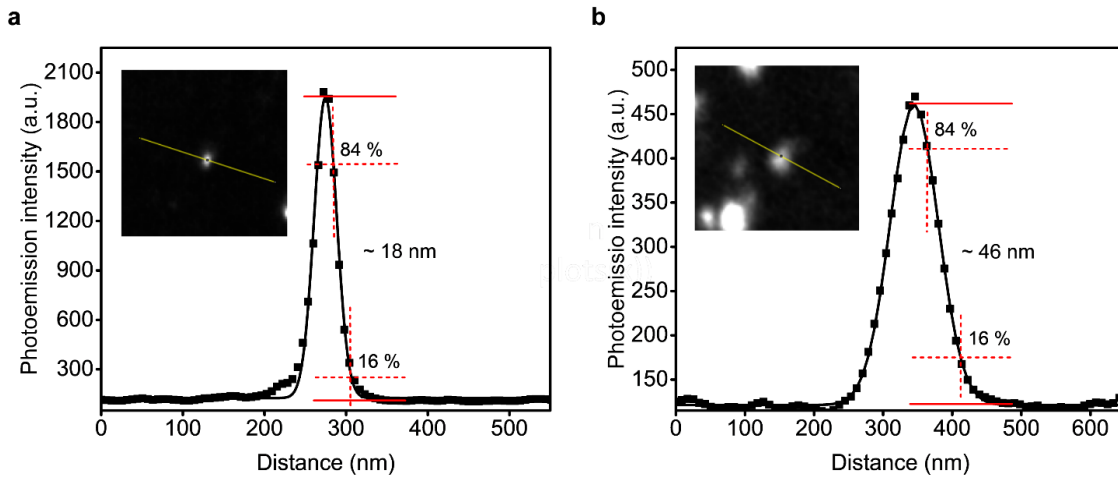


Figure 2.6. Spatial resolution of PEEM imaging. (a) 84 % 16 % profile for perovskite thin film sample with good alignment showing best resolution of 18 nm. (b) 84 % 16 % profile for perovskite sample with poor alignment and space charge effects showing decreased spatial resolution of 46 nm.

PEEM is known to be a surface-sensitive technique. Therefore, it is important to discuss the probe depth of the PEEM measurements. Here we will discuss two important parameters: inelastic mean free path of an electron escaping from the material and absorption depth of the optical probe beam in the material. The electron inelastic mean free path (the path electron travels before losing its energy) is described by the universal curve [336, 337]. This law was established in 1979 by compiling published data for inelastic mean free paths for elements, inorganic and organic compounds [336]. In our PEEM experiments we use probe photon energies of 4.65 eV and 6.2 eV, which result in low kinetic energies of photo-emitted electrons. Such electrons have escape depths of up to few tens of nanometers according to the universal curve [336, 337]. Based on optical constants for $\text{CH}_3\text{NH}_3\text{PbI}_3$ perovskite, reported in refractive index database [338], we estimate the penetration depth of 266 nm UV photons to be on the order of 12.5 nm, and of about 14.7 nm for 200 nm photons. Therefore, the probe depth of our experiment will be mostly determined by the absorption depth of the UV photons in the material. Given the geometry of our experiment (*e.g.*, incident angle of probe photons) and variation in optical constants for different perovskite compositions, we roughly estimate the probe depth of our experiment to be on the order of 10 nm.

2.3. Time-resolve photoemission electron microscopy

Time-resolved PEEM is a novel technique that allows to follow the spatio-temporal evolution of the excited state in materials. TR-PEEM is realized when nanometer spatial resolution of PEEM is coupled with femtosecond time resolution of optical pump-probe spectroscopy. The first attempts of TR-PEEM began in 1990s with works researching time dependence of melting, crystallization and alloying of Al films [339], electron excitations in GaAs covered with Ag patterns [340]. Among more recent applications are ultrafast carrier dynamics in two-dimensional materials [310, 341], ultrafast electron dynamics in semiconducting nanowires [309], charge carrier trapping in hybrid perovskite thin films [47] and microcrystals [307].

2.3.1. General aspects of TR-PEEM

During TR-PEEM experiment, sample in the PEEM chamber is photo-excited by the incoming pump pulses, similar to ultrafast optical spectroscopy [342]. However, instead of monitoring the changes in transmission or reflection of optical probe, in TR-PEEM we collect electrons photo-emitted with the UV probe pulses (Figure 2.7a, b). By accurately controlling the time delay between pump and probe, we can record snapshots of electrons photo-emitted from specific energy levels in material at each time delay between pump and UV probe and create movies of electron motion in space and time (Figure 2.7c).

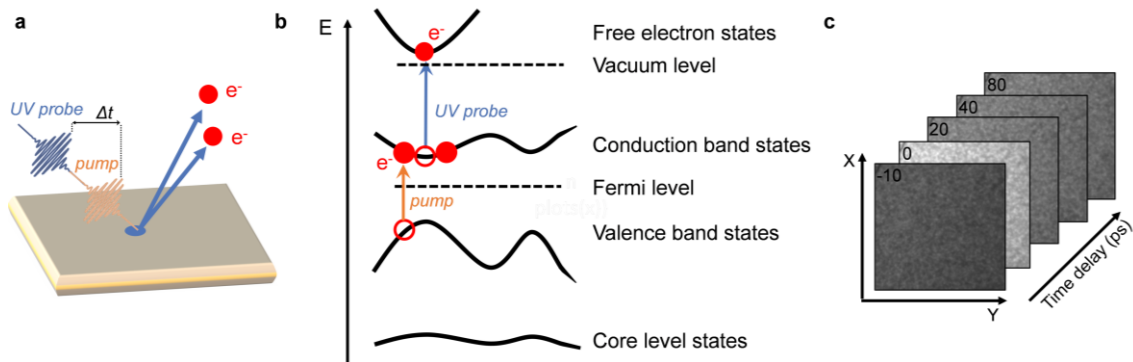


Figure 2.7. Diagram of time-resolved photoemission. (a) The UV light (*UV probe*) arrives after the sample was photo-excited with pump pulse (*pump*) and causes photo-emission of electrons (e^-) from the surface of a solid. (b) Upon absorption of pump photons, electrons (red circle) from the valence band states are promoted to conduction band leaving holes (hollow red circle) behind. The UV probe pulses photo-emit electrons from the conduction band to the free electron states above the vacuum level. (c) Snapshots of electron motion at selected time delays between pump and UV probe pulses in TR-PEEM.

To set up TR-PEEM experiment, the output of the laser was split into two paths (Figure 2.8): (i) probe beam that entered the UV generation setup and (ii) pump beam that was directed to the mechanical delay stage, similar to the geometry of optical pump-probe spectroscopy. The UV light was generated by frequency up-conversion using nonlinear BBO crystals, as was discussed in Section 2.2.3. Both pump and UV probe pulses were directed on the sample by passing through fused silica window of the main chamber of the microscope. The path lengths for both pump and probe should be precisely equal to achieve temporal overlap of pulses on the sample. In addition to temporal overlap, spatial overlap of pulses was also required. Due to the geometry of PEEM experiment, our photon beams were hitting the sample under an angle and therefore, were stretched along one axis. The spot size for the pump in our experiment was measured to be about $60\ \mu\text{m}$ by $150\ \mu\text{m}$ (full width of half maximum of the short and long axes of elliptical spot). The probe beams were measured to be $80\ \mu\text{m}$ by $120\ \mu\text{m}$ for $4.65\ \text{eV}$ and $40\ \mu\text{m}$ by $80\ \mu\text{m}$ for $6.2\ \text{eV}$.

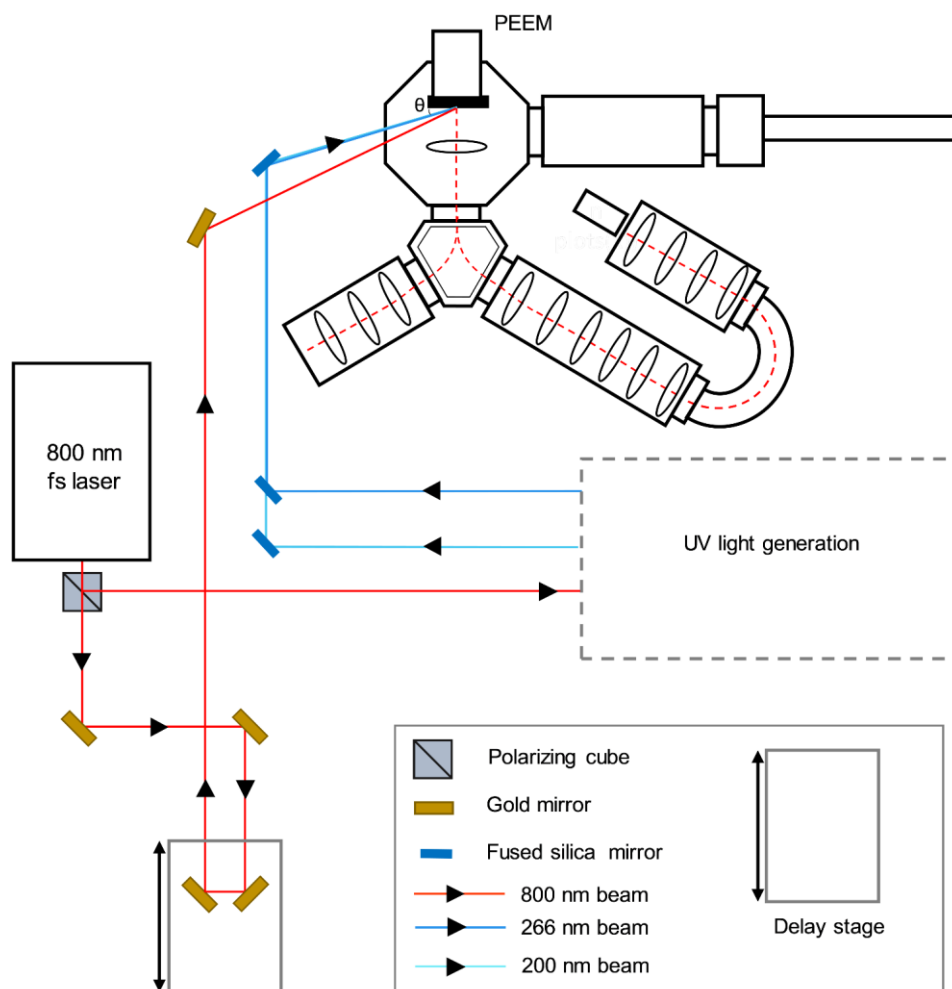


Figure 2.8. Diagram of TR-PEEM experiment. Output beam of a femtosecond pulsed laser source is split for the generation of UV light (highlighted with grey dashed line) and for the optical pump. Pump beam passes through a mechanical delay stage and is focused on the sample through the side window of PEEM.

The choice of pulsed laser system for TR-PEEM measurements is also important to discuss. Here, some of the aspects of ultrafast spectroscopy are applicable. For example, the repetition rate of the laser system which dictates the time separation between the pulses should be chosen according to the experimental requirements. For semiconducting materials, the lifetimes of photo-excited carriers span between few tens of nanoseconds to microseconds. This implies that in order to avoid introducing measurement artifacts, such as for example occurrence of subsequent photo-excitation event before the charge carriers fully relaxed back to the ground state, one needs to carefully select laser system with appropriate time separation between pulses. For example, a laser system with 2 MHz repetition rate has 500 ns separation between pulses and will be suitable to study materials with charge carrier lifetimes lasting for up to a couple of hundreds of nanoseconds. Although kHz systems with pulse separation up to millisecond would allow to study materials with long-lived charges, there are limitations to using such laser systems in TR-PEEM. One large issue are space charge effects that occur when exposing the sample to high probe doses. Typically, kHz lasers are amplifier systems, which means that they have very high energies per pulse. For example, a typical 1 kHz laser system (Spectra Physics Spitfire Ace) produces pulses with energy equal to 5 mJ, which will inevitably result in spectral broadening in PEEM due to Coulomb repulsions between the photo-emitted electrons. Therefore, it is generally better to use MHz lasers for TR-PEEM [305]. Moreover, MHz systems imply that electrons photo-emitted by each pulse will hit PEEM detector more frequently, thus resulting in moderately fast image acquisition times.

In our TR-PEEM setup, we used Ti:Sapphire pulsed laser system (FemtoLasers XL:650) with 45 fs pulse duration, operating at 4 MHz repetition rate and supplying pulses of 650 nJ in energy. Such parameters were suitable for TR-PEEM experiments on our hybrid perovskite samples and allowed to acquire data reasonably fast and avoid space charge regime when using moderate fluences for both pump and probe. The layout of our experiment follows the schematic introduced in Figure 2.8. We used the fundamental output of the laser system (800 nm or 1.55 eV) as pump and frequency tripled and quadrupled photons (266 nm or 4.65 eV and 200 nm or 6.2 eV) as probe. Details about generation of probe photons were discussed in Section 2.2.3. We used the delay stage allowing to achieve maximum time delay between pump and probe of about one nanosecond.

2.4. Interpretation of TR-PEEM signal

TR-PEEM signal interpretation is another important aspect to discuss. Typically, in PEEM depending on the energy of the probe photons, we can image electrons photo-emitted from the onset of the valence band, or from core levels. By using energy slits, we can pre-select the particular energy range to image. When the pump pulse is introduced, electrons are promoted to the conduction band, and by sending follow-up UV pulses, we can image this photo-excited state. These processes can be explained on example of GaAs – a semiconducting material that we typically use to obtain temporal overlap between pump and UV probe pulses for TR-PEEM experiments. We will discuss here specifically the case of two probe energies (4.65 eV and 6.2 eV) available in our experimental set-up.

For TR-PEEM experiment, we first need to create a population of photo-excited electrons in the conduction band of GaAs. GaAs is a semiconducting material with band gap of about 1.4 eV. The pump photons of 1.55 eV in energy produced by our laser system, are sufficient to photo-excite electrons from the valence band to the conduction band of GaAs. By choosing the energy of probe photons, we can study different electronic states of GaAs. For example, the probe photons of 6.2 eV in energy, couple to the transitions from the onset of the valence band of GaAs (Figure 2.9a), and therefore, can be used to visualize these transitions. This will provide information about population of valence band states of GaAs. After the photo-excitation with pump photons, electrons from the valence band states are promoted to the conduction band states, and the overall population of electrons at the onset of the valence band decreases. In TR-PEEM, by utilizing 6.2 eV probe photons, we can visualize this reduction in population of valence band states, as seen from the sharp decrease in photoemission intensity after photo-excitation (Figure 2.9b and c). In Fig. 2.9c, we show typical TR-PEEM images of GaAs acquired with 6.2 eV photons at several selected time delays between pump and probe after the photo-excitation. For better clarity, we plot the difference signal $[I(t) - I_0]$ and color-code the negative change in photoemission intensity that indicates reduction in population of electronic states with blue, and the increase in photoemission intensity, or increased population of electronic states, with red. Since we are not using energy filter, the signal is dominated by the photo-emission from the valence band states, and the probe photons are either not coupling strongly to the transitions from conduction band states, or the population of photo-excited electrons is low. Figure 2.9b shows integrated photoemission intensity from Figure 2.9c as a function of pump-probe time delay. It is clearly seen that photoemission intensity decreased at the instance of photo-excitation.

In contrast to 6.2 eV probe photons, when employing 4.65 eV photon probe, upon arrival of pump pulse we observe a sharp increase in the photoemission signal (Figure 2.9e and f). This means that with photons of 4.65 eV in energy, we are capable of probing the photo-excited state created by the arrival of pump pulse. The 4.65 eV photon energy is not sufficient to probe the onset of the valence band of GaAs, as seen from the energy-level diagram in Figure 2.9d, however, is sufficient to couple to transitions from the conduction band states. This explains a growing population of conduction band states after the photo-excitation that is seen from the increase in photoemission intensity in Figure 2.9(e and f). For better visualization, we plotted the difference signal $[I(t) - I_0]$ and color-coded the increase in photoemission intensity with red (Figure 2.9f). The sharp increase of the integrated signal shown in Figure 2.9e indicates that at the instance of photo-excitation, the excited state population is created, which we probe with 4.65 eV photons.

Similar approach can be applied for other semiconducting samples. The decrease in photoemission intensity will indicate the loss of electrons due to either photo-excitation or charge transfer, while increase in photo-emission intensity will be a signature of increased electron population. The exact interpretation of signal, of course, will depend on the material and the exact electronic states that are being probed.

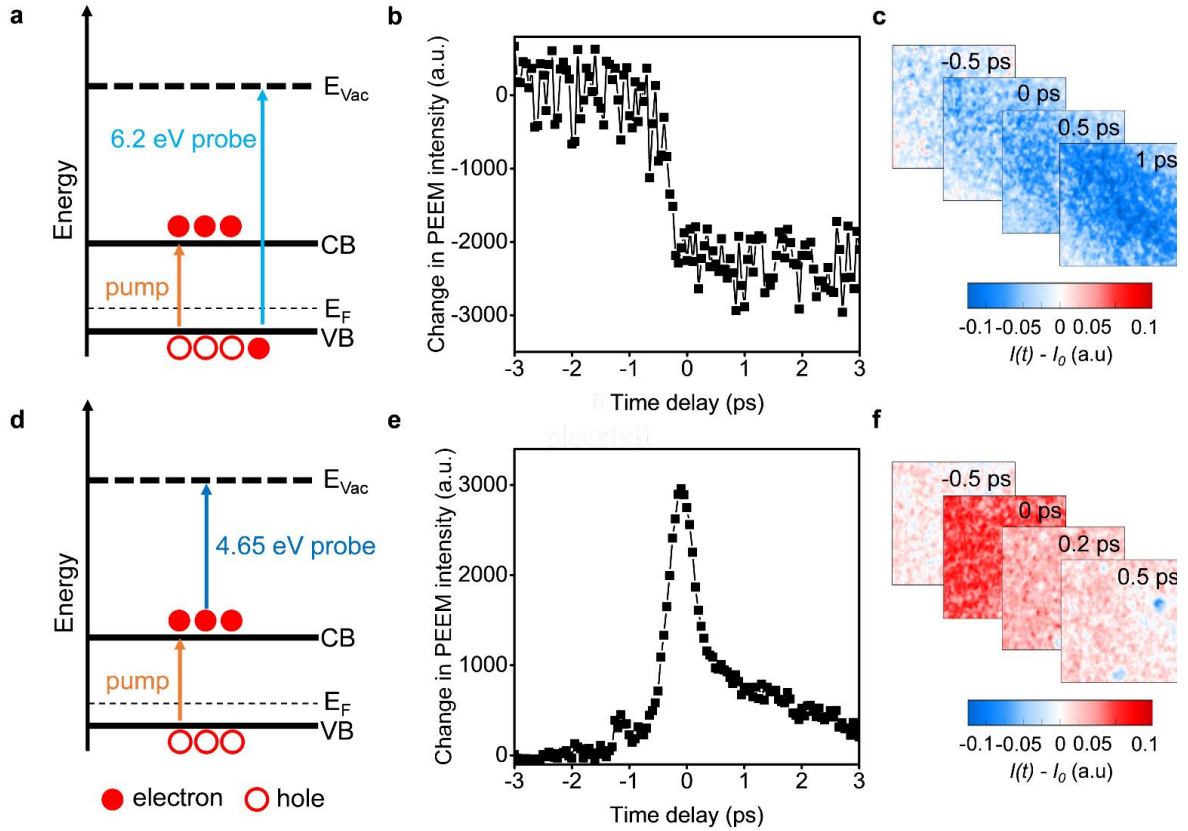


Figure 2.9. Interpretation of TR-PEEM signal. (a) Energy level diagram of p-doped GaAs sample. Upon photo-excitation with pump photons (*pump*), electrons (filled red circles) are promoted from valence band (*VB*) to the conduction band (*CB*), leaving holes behind (hollow red circles). UV probe photons (6.2 eV probe) cause photo-emission of remaining electrons from valence band states to the vacuum level (E_{Vac}). By changing time delay between pump and probe pulses, the evolution of the population of valence band states can be traced. (b) TR-PEEM decay curve for the process described in (a). Because electrons are promoted from the valence band states to the conduction band states, the population of valence band decreases, and change in photoemission intensity is negative. (c) TR-PEEM images for selected time delays in (b), showing a clear decrease in photoemission intensity colored with blue. (d) Energy level diagram for GaAs sample when probed with photons of lower energy (4.65 eV probe). Again, pump photons (*pump*) cause photo-excitation of electrons from valence band (*VB*) to conduction band (*CB*). Here, however, the lower energy photons photo-emit the photo-excited electrons from the conduction band to the vacuum level (E_{Vac}). (e) TR-PEEM decay curve for the processes described in (d). Because here we are probing conduction band states that were populated after the photo-excitation, the change in photoemission intensity is positive. (f) TR-PEEM images for selected time delays in (e), showing clear increase in photoemission intensity after photo-excitation colored with red.

2.5. Conclusion

In this Chapter we have discussed operational principles of photoemission electron microscopy. We covered operating modes of PEEM, general aspects of PEEM imaging that are important when planning photoemission microscopy experiments. Additionally, we discussed time-resolved photoemission electron microscopy - a rather novel, yet very powerful approach to combine spatial resolution of PEEM with temporal resolution of optical pump probe spectroscopy. We provided considerations for successful TR-PEEM experiments, as well as showed some of the limitations of the technique that should be kept in mind when investigating particular properties of materials. We showed that PEEM and TR-PEEM can be applied to directly visualize electrons photo-emitted from various occupied states in the material. The work in this thesis will heavily rely on capabilities of PEEM and TR-PEEM to characterize nanoscale surface defects in hybrid perovskite thin films.

Chapter 3

Photoemission Electron Microscopy of Hybrid Perovskite Thin Films

3.1. Abstract

The presence of defects in hybrid perovskite thin films has been reported to be a crucial performance-limiting factor for perovskite solar cells [9]. However, much remains unknown about these defects. In particular, more understanding is required about the nature of these defects, their formation sites, distribution and exact roles in performance of the film. In this Chapter, we employ photoemission electron microscopy to visualize nanoscale surface defects in triple cation mixed halide perovskite thin films. Via correlating PEEM images of defects and surface microstructure of the film, acquired with photoemission electron-, atomic force- and scanning electron microscopies, we will establish the location of defects with respect to the surface microstructure.

3.2. Nanoscale distribution of defects

As discussed in Chapter 1, to study processes that occur on micro- and nanoscale but impact performance of the whole film, it is essential to utilize tools with high spatial resolution, such as microscopy techniques. This approach becomes very powerful when we want to understand defect-induced behavior in polycrystalline perovskite thin films. Here we employ photoemission electron microscopy to study hybrid perovskite thin films. By selecting appropriate energy of probe photons, in PEEM, we can directly probe the occupied mid gap (defect) states and study their spatial distribution.

3.2.1. Sample preparation and mounting for PEEM

Perovskite thin film samples have been prepared at the University of Cambridge by our collaborators from the group of Prof. S. Stranks, and shipped to Okinawa Institute of Science and Technology Graduate University in well-sealed packaging to avoid exposure to ambient air. During the preparation and subsequent mounting and transfer for PEEM imaging, samples were handled in N₂-filled glovebox.

To prepare the perovskite thin films with composition (Cs_{0.05}FA_{0.78}MA_{0.17})Pb(I_{0.83}Br_{0.17})₃, formamidinium iodide (FAI) (1 M), methylammonium bromide (MABr) (0.2 M), PbI₂ (1.1 M), PbBr₂ (0.22 M) were dissolved in anhydrous dimethylformamide/dimethyl sulfoxide (DMF:DMSO 4:1 (v:v)). CsI in DMSO (1.5 M) was then added to the precursor solution. The precursor solution was spin-coated on clean ITO substrates (up to 1 cm by 1 cm in size) in a two-step process: first 2,000 rpm for 10 s, then 4,000 rpm for 35 s, with addition of 100 µl of chlorobenzene 30 s before the end of the second step. After spin-coating, the films were annealed at 100°C for 1 hour. Notice that for PEEM imaging, it is important to deposit samples on conductive substrates to prevent sample from charging.

For PEEM imaging, sample was mounted on special PEEM sample holder (Figure 3.1a) that was kept in N₂-filled glovebox. The mounting required careful attention, especially when working inside the glovebox. The sample on the sample holder (cartridge) was fixed and covered with a cap, leaving out an open region of approximately 0.8 cm by 0.8 cm, that could be explored in PEEM by moving the sample stage in X and Y directions with microscope manipulator. During sample mounting, it is important to keep the sample surface as flat as possible. This implies avoiding overtightening the screws on one side when fixing the cap, as this will introduce sample tilt, cause distortions and reduce resolution during PEEM imaging. Typically, the first step of PEEM imaging is tilt correction, which is done manually in the Elmitec SPELEEM III microscope that we utilized for the work in this thesis. Such tilt correction allows electron beam to go through the optical axis of the objective and prevents image distortions. Only a limited amount of tilt can be compensated in this way – therefore, it is important to make sure the sample was mounted as flat as possible from the beginning. In order to secure sample from moving on the cartridge, it is convenient to apply a little piece of carbon tape to the edges of the sample, as shown in Figure 3.1b, although is not a requirement. Small amount of carbon tape did not cause any outgassing issues in the imaging chamber of the microscope during the work on this thesis.

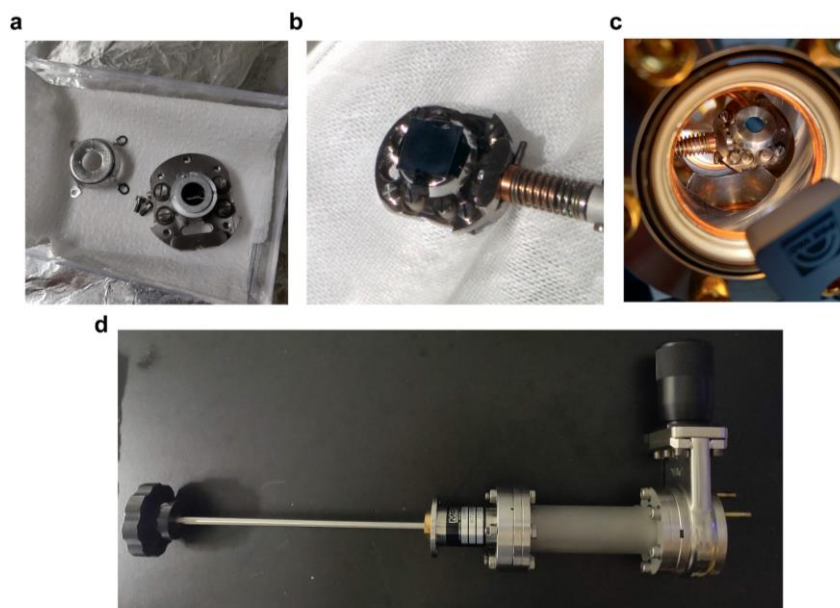


Figure 3.1. PEEM sample mounting. (a) Sample holder that consists of a cartridge and a cap. (b) Perovskite thin film sample on glass/ITO substrate positioned on the sample holder before covering with cap. (c) Sample holder with perovskite sample inside the preparation chamber of PEEM. (d) Hermetically sealed suitcase for transferring air-sensitive samples to PEEM.

After the sample was mounted, the cartridge was transferred to the PEEM (Figure 3.1c) inside of a hermetically-sealed suitcase (Figure 3.1d). In this way we ensured no exposure to ambient environment that is known to have a negative impact on stability of perovskites [343].

One important step before mounting perovskite samples for PEEM imaging, was to assess the film surface with optical microscopy. Using optical microscope, we can quickly check the film coverage, as well as mark regions for PEEM imaging. A typical optical image of a good quality perovskite thin film, is shown in (Figure 3.2a). A sample with poor coverage and morphology, can be immediately identified from optical microscopy.

To correlate the areas of interest after PEEM imaging with other imaging techniques, we deposited fiducial gold markers on the surface of perovskite films (Figure 3.2b). This approach appeared to be quite useful in multiple projects, and was first implemented and best described in the work by Jones *et al.* [133]. These uniquely-shaped micrometer-scale gold hexagons, pentagons and triangles were easily recognizable through different microscopy techniques and served for multiple purposes. Fiducial gold markers were used as guides to locate regions of interest, helped establish Fermi level for photoelectron spectroscopy measurements, and were used to remove laser intensity fluctuations in time-resolved measurements. The deposition of gold markers did not affect our measurements or interpretations of our results [47].

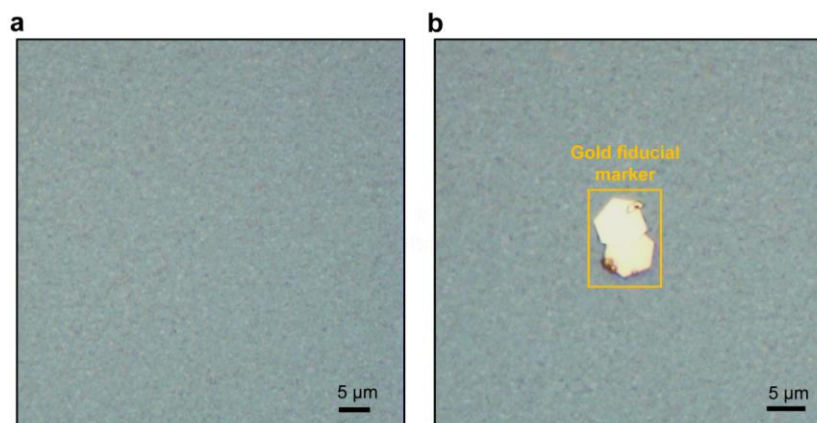


Figure 3.2. Optical microscopy images of a perovskite thin film sample. (a) A uniform film surface, typically expected for good-quality perovskite films. (b) Gold fiducial markers deposited on the film surface for guidance in correlative measurements.

3.2.2. *Imaging of nanoscale defects in perovskite thin films with PEEM*

We performed PEEM imaging of perovskite thin film in the main chamber of PEEM, where we applied high voltage between the objective lens and sample. High voltage was raised in small increments from 0 to 20 kV to avoid discharge – an electric arc that can occur between the sample and objective lens. We used 4.65 eV photons as a probe to access mid gap states in perovskite (see Figure 3.3a for schematic). Upon absorption of probe photons, electrons were liberated from these mid gap states, and imaged with electron optics of the microscope.

A typical PEEM image of defects in triple-cation mixed halide perovskite samples, is shown in Figure 3.3b. These defects appeared as nanoscale clusters of various sizes (defects colored with green in Figure 3.3b). These nanoscale defects were present in all measured perovskite films. Pristine areas that did not contain defects, remained dark in PEEM images. Excluding the areas with nanoscale defects, most of the surface area of perovskite thin films was pristine.

To obtain high resolution images, it is recommended to use low dose of UV probe photons to avoid overexposing sensitive perovskite samples. We generally kept the fluences of 4.65 eV probe photons below 100 nJ cm^{-2} for all the PEEM measurements. Upon using such low probe fluences, we did not observe any obvious probe-induced sample damage throughout our experiments. High resolution PEEM images of defects were acquired at $10 \mu\text{m}$ field of view and with contrast aperture to optimize image resolution. PEEM images of defects have been taken with typical imaging conditions of 10 - 15 seconds exposure per frame, and averaged between 25 - 35 frames. Each PEEM image has been processed with flat field method to remove inhomogeneity originating from detector part of the instrument. Multiple image frames were drift-corrected before averaging.

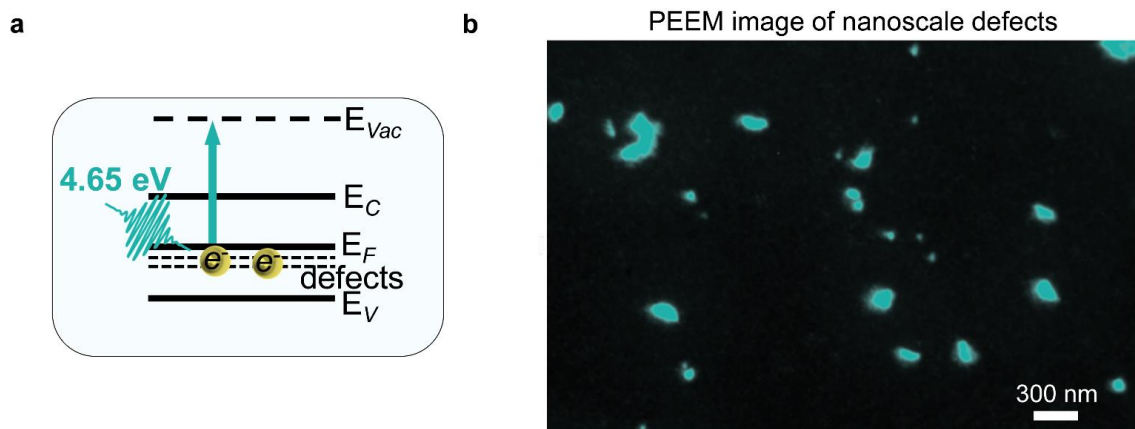


Figure 3.3. PEEM imaging of nanoscale defects in perovskite thin films. (a) Energy-level diagram of perovskite sample: green arrow indicates transition from defect states (*defects*) below the Fermi level (E_F) to vacuum states with E_{Vac} when probing of sample with photon energies of 4.65 eV; valence band states are indicated with E_V , conduction band states with E_C . (b) PEEM image visualizing nanoscale distribution of defect clusters (colored with green) on the surface of triple-cation mixed halide perovskite thin film. Pristine regions without defects, do not show PEEM intensity upon probing with 4.65 eV photons.

Alternatively, one can visualize defect states by performing energy-resolved imaging in PEEM (Figure 3.4) using photons with higher energies (see Chapter 4 for more details). Photons of higher energies allowed to access onset of the valence band, and photo-emit electrons from there. By energy-filtering contributions from only mid gap states using energy slit and hemispherical energy analyzer, we collected signal selectively only from the mid gap states in perovskite samples. Thus, via energy-resolved imaging with higher energy photons, we imaged occupied defect states as nanoscale clusters, similarly to Figure 3.3b. The acquisition time in this mode is typically longer, since with energy filter, we are only accessing a narrow portion of the energy spectrum. Therefore, signal to noise ratio for one frame is typically lower. Also, given the low signal-to-noise ratio, microscope alignment in this mode is more difficult, therefore the image resolution can be considerably lower comparing to Figure 3.3b. Throughout this thesis, all the high resolution images of defects were acquired using 4.65 eV probe photons, unless specifically indicated otherwise.

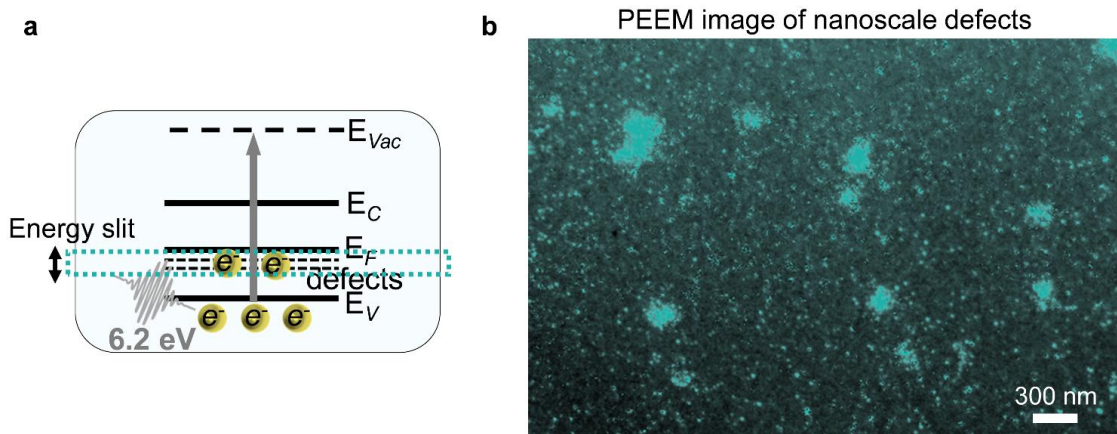


Figure 3.4. PEEM imaging of nanoscale defects with energy-filtering. (a) Energy-level diagram of perovskite sample: grey arrow indicates transitions from valence states (E_V), defect states (*defects*) below the Fermi level (E_F) to vacuum states (E_{Vac}) when probing of sample with photon energies of 6.2 eV; conduction band states are marked with E_C . (b) Energy-filtered PEEM image visualizing nanoscale distribution of defect clusters on the surface of triple-cation mixed halide perovskite thin film. The image was acquired using energy analyzer and with an energy slit to collect only contributions from mid gap states, as indicated with green dashed box in (a).

3.2.3. Considerations for PEEM imaging

To obtain high quality PEEM images of nanoscale defects in hybrid perovskite thin films, a few important points need to be considered.

(i) *Space charge.* Space-charge effects are very likely to occur during PEEM imaging if using high probe fluences. These effects originate from Coulomb repulsions between many photo-emitted electrons. This results into modification of their trajectory and kinetic energies [332, 333, 344] and causes spectral broadening (broadening of kinetic energy distribution) and energy shifts in photoelectron spectroscopy. In PEEM images, space charge effects can be seen as image blur and loss of spatial resolution.

The laser system used in this thesis, was a 4 MHz Ti:Sapphire laser, the fundamental output of which was tripled and quadrupled to generate harmonics used for imaging (4.65 eV and 6.2 eV), as discussed in Chapter 2. In the reported estimations [332], the limit for space-charge-less imaging is on the order of ($10^6 - 10^7$) photons/pulse to stay within 1 electron/pulse regime. In our case, for a 4 MHz laser system, this corresponds to approximately 10^{13} photons/s. Our fourth harmonic generation set-up can output on the order of 10^8 photons/pulse for 6.2 eV photons, which implies that we should pay careful attention to use a low photon dose to avoid experiencing space charge effects. Therefore, for PEEM imaging, we used approximately 10 nJ cm^{-2} of 6.2 eV photons or $\sim 10^5$ photons/pulse. For the 4.65 eV, our setup is capable of generating 10^9 photons/pulse. During the PEEM imaging, we only used on the order of 100 nJ cm^{-2} of 4.65 eV photons, or $\sim 10^6$ photons/pulse to avoid space charge. These values of number of photons per pulse for both 6.2 eV and 4.65 eV photons in our experiments indicated that we

stayed below the space charge limit. Therefore, we do not expect space charge effects to influence our data analysis and interpretation.

(ii) *Image acquisition.* Due to the low fluence of probe photons that is required to avoid space charge and loss of resolution, the image acquisition time becomes relatively prolonged. To obtain high-enough contrast for each image, exposure times far exceeding a few seconds are typically required for perovskite samples, especially when using contrast aperture for high-resolution imaging. Even then, in order to obtain enough contrast and resolve small features, it is better to accumulate several images and average them together to enhance signal to noise ratio. In this case, it is advised to drift-correct each image in the sequence prior to averaging to remove small sample drift that can occur over time during multiple exposures. Alternatively, one can average images right away using image acquisition tools available in the instrument software without any drift correction. Although this method is faster (does not require post-processing), it does not provide a chance to remove sample drift, which is an important part of obtaining high-quality images. For this thesis, sequences of PEEM images have been acquired, drift-corrected and averaged to generate each image frame. The spatial resolution of PEEM was measured to be about 18 nm for the best quality data (see Chapter 2).

(iii) *Image processing.* As has been mentioned above, it is critical to apply drift-correction tools to the PEEM images to avoid losses in resolution due to sample drift. In this thesis, a home-written Matlab script was used for this task. Alternatively, some open source software, such as ImageJ etc., can also be used for drift-correction. Additionally, we often applied flat field correction to our images to remove non-uniform response from the detection system of the instrument.

3.2.4. Defects in triple cation mixed halide perovskite thin films

In Section 3.2.2, we discussed general aspects of visualizing defect states in hybrid perovskite thin films with PEEM. In this Section, we aim to shed more light on the distribution of these nanoscale defects in triple cation mixed halide perovskite films. To achieve this, we have carefully analyzed our PEEM images, specifically looking at possible preferential location of defects and their related sizes.

As has been revealed from our PEEM images, the triple cation mixed halide perovskite thin films with composition of $(\text{Cs}_{0.05}\text{FA}_{0.78}\text{MA}_{0.17})\text{Pb}(\text{I}_{0.83}\text{Br}_{0.17})_3$, contained defects that varied in sizes from few tens to few hundreds of nanometers (Figure 3.5a, b) [284]. We did not observe defects accumulating in specific parts of the film, but rather distributed throughout the entire film. We confirmed this by imaging multiple areas of one sample and by imaging multiple samples.

The smallest defects we have imaged in PEEM, were about few tens of nanometers in sizes (Figure 3.5c, green box), which already approached the limits of our spatial resolution. We do not exclude presence of even smaller (point) defects, however these would be impossible to identify due to the spatial resolution limits in our PEEM instrument. Besides small defects, we also observed much larger defects of up to few hundreds of nanometers (Figure 3.5c, red and blue boxes). Given the average grain size in our films of up to few hundreds of nanometers, larger defects were likely approaching the grain size.

We did not observe any preferential spatial orientations of the imaged defects. In fact, the presence of some preferential orientation for all the features in image, could be a signature of stretch originating from astigmatism in the image which can result from poor alignment of PEEM objective stigmators or from uncorrected sample tilt (for example, circular features could appear elliptical in the image).

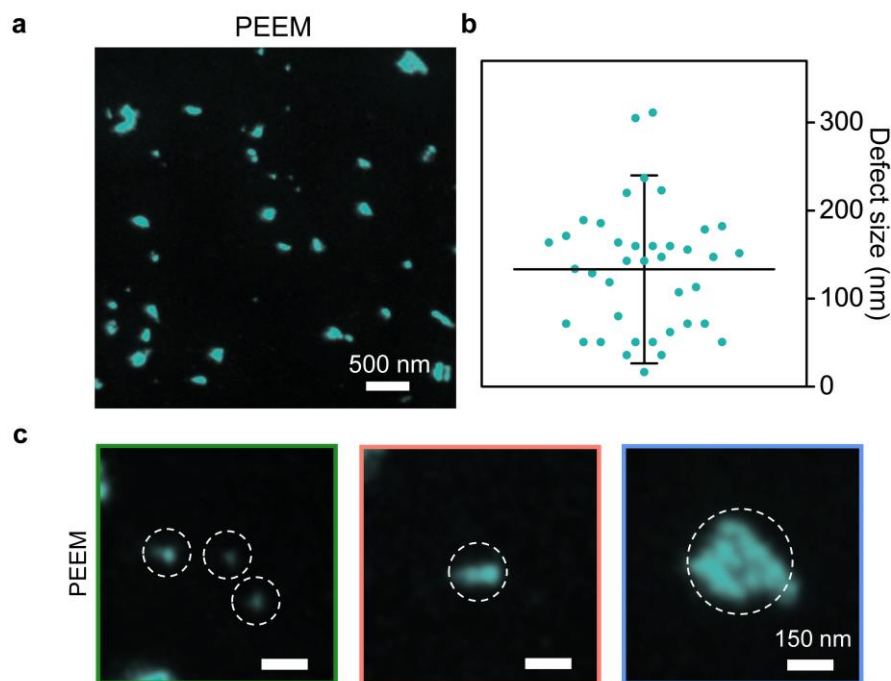


Figure 3.5. Size distribution of nanoscale defects in perovskite thin films. (a) A typical PEEM image of defects. (b) Size distribution of defects (from a $6\ \mu\text{m}$ by $6\ \mu\text{m}$ area). (c) Magnified PEEM images of defects of different in sizes, from few tens to few hundreds of nanometers.

After visualizing these nanoscale defects, the immediate question that appeared was regarding their origin. Given the polycrystalline nature of perovskite thin films, one particularly interesting question was how the observed defects were related to the surface microstructure. It would be especially beneficial to correlate the imaged defects with surface microstructure to shed more light on the contradicting question in perovskite community: whether the grain boundaries were defective, or the grains themselves were sources of electronic losses. Our results on such correlation, will be further discussed in Sections 3.4 and 3.5.

As a side note, throughout the work on this thesis, we also studied other spin-coated triple cation perovskite samples with I-only compositions and double cation mixed-halide thin films deposited using evaporation methods. In both cases, we also imaged nanoscale defects of different sizes [132]. These studies are parts of ongoing projects led by our colleagues from the Stranks Lab at the University of Cambridge, and therefore will not be discussed in detail in this thesis. We briefly mention these results here to stress that according to our observations, the nanoscale defects appear in perovskite samples regardless of their composition and fabrication methods.

3.3. Surface morphology of perovskite thin films

In general, we typically utilize scanning electron- or atomic force microscopies (SEM and AFM, respectively) to visualize surface morphology of materials. Due to the sensitive nature of perovskites towards electron beam probes [345] (for example, high doses of electron beam may cause structural changes to perovskite samples), scanning electron microscopy is usually conducted on samples as a last measurement. Additionally, mounting and transfer of perovskite samples to these microscopes, involve exposing samples to ambient environment, and may cause irreversible changes to the perovskite film. This is undesirable if there is a need to continue measurements on the same sample to correlate with previous experiments.

In this thesis, we developed a protocol to image surface microstructure of perovskite thin film samples in PEEM. For this, we utilized probe photons of higher energies (6.2 eV) that allowed to photo-emit electrons from the onset of the valence band. The benefits of this approach are following: (i) we can avoid using SEM or AFM to obtain good quality images of surface morphology of perovskite samples (especially important given the sensitivity of perovskites towards electron beam probes and exposure to ambient environment, described above); (ii) this method is non-destructing – we use controlled dose of 6.2 eV photons for imaging and eliminate sample damage, unlike when using electron beam probe in SEM; (iii) this approach allows for more flexibility to conduct multiple PEEM experiments on the same sample (photoelectron spectroscopy, time-resolved PEEM); (iv) this method also provides ability to superimpose obtained images of defects and surface microstructure with high accuracy without facing issues of magnification and resolution of different instruments. Such characterization does not exclude possibility to utilize other types of microscopies on perovskite samples after PEEM.

3.3.1. *Imaging surface morphology in hybrid perovskites with PEEM*

In PEEM, in contrast to scanning electron microscopy, surface topography can be imaged without scanning, using a loosely focused UV probe photon beam to illuminate a wide area of the sample surface (typically, up to 100 μm). In the case of PEEM measurements on polycrystalline perovskite samples, electrons that are photo-emitted from the valence band states (Figure 3.6a), can be imaged as grains (Figure 3.6b).

To image surface microstructure of perovskite films, we used 6.2 eV probe photons and utilized hemispherical energy analyzer to filter-out electrons that were photo-emitted from the mid gap states to image only electrons photo-emitted from the onset of the valence band.

A high resolution PEEM image of surface morphology of perovskite sample, is shown in Figure 3.6b. The overall image quality approaches the quality of an SEM image (see Figure 3.12 for comparison). Features, such as grain boundaries and grains, are visualized clearly. There is occasional loss of contrast that could be originating from local energetic heterogeneities or small variations in surface roughness, as will be discussed in Section 3.3.2. The images of surface microstructure will be later on used to correlate the spatial arrangement of defects with the film morphology.

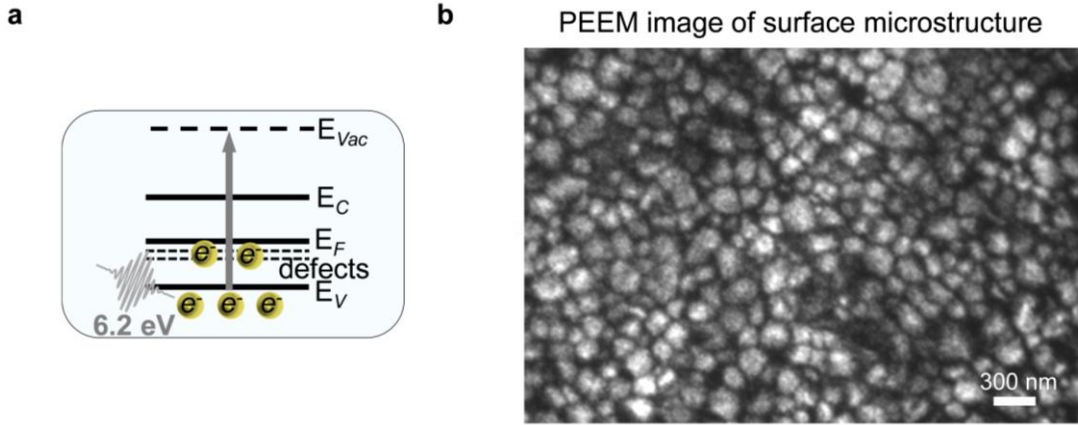


Figure 3.6. PEEM imaging of surface microstructure of perovskite thin films. (a) Energy-level diagram of perovskite sample: grey arrow indicates transitions from valence band states (E_V) to vacuum states (E_{Vac}) when probing of sample with photon energies of 6.2 eV; Fermi level is indicated with E_F , and conduction band states are indicated with E_C . (b) High-resolution PEEM image of grains of the same area that was shown in Fig. 3.3.

3.3.2. Considerations for imaging polycrystalline films in PEEM

There are a few important points to consider when we image surface microstructure of perovskite thin films in PEEM.

(i) *Interplay between the dose of probe photons and image acquisition.* When the onset of the valence band is imaged in PEEM, a large number of electrons are photo-emitted from the valence states. These electrons can interact with each other via Coulomb repulsions and cause space charge. Therefore, it is very important to use low doses of probe photons to avoid loss of image resolution due to space charge. At the same time, upon using low doses of probe photons, it becomes very challenging to monitor image in real time, as prolonged exposure is required to acquire an image. This is important to keep in mind when aligning the microscope and adjusting the focus. Essentially, each time when the objective focus is adjusted, long exposure is required to visualize grains and assess the quality of the image, and therefore, many iterations are needed to find appropriate setting for the objective lens to bring the image in focus. Even though this process is time consuming, it is essential for energy-resolved imaging for photoelectron spectroscopy that will be discussed in Chapter 4.

Typical image acquisition times when imaging grains, were about 60 seconds per frame. Multiple frames (typically, 15 - 20) were acquired, drift-corrected and averaged together to enhance signal to noise ratio of the final image. We used small energy-analyzer slit (125 meV) to avoid collecting signal from mid gap states, and a contrast aperture. Typically, when using energy slit and contrast aperture, the number of photoelectrons that reach the detector of the instrument is reduced. Due to this, the image acquisition time becomes prolonged. However, the fluence of probe photons should not be increased to compensate and reduce the image acquisition time, or else the space charge effects will occur on an overexposed sample. To avoid sacrificing image resolution, very careful attention must be paid to keep the dose of probe photons low, even on the expense of prolonged imaging time.

(ii) *PEEM contrast.* Perovskite thin films have polycrystalline nature, which means that samples are not uniformly flat, instead, the film grows forming grains. Since PEEM is widely known to work well for what is considered flat surfaces, it is worth briefly discussing what goes into PEEM contrast for polycrystalline films that have large density of grain boundaries. In particular, the edge contrast deserves attention here. While most of the contrast in PEEM image of perovskite films, is coming from electrons that are photo-emitted from the valence band states, the grain boundaries are visualized very clearly due to the so-called edge contrast. This contrast mechanism has been explained by Siegrist *et al.* [346]. The edge contrast can be explained with example of a sample having a step-wise morphology, such as patterned features on wafers. Lateral field develops in the vicinity of the step edge. Such effects appear due to strong acceleration field used for imaging when there is a potential difference between different grains. This lateral field is strong enough to deflect photo-emitted electrons, as it causes electrons that are photo-emitted from step edges (grain boundaries in our case) to be displaced from the image collection volume. The edge contrast will also increase with the step height, and in our case, the depth of grain boundary, as the lateral field strength increases.

Besides contrast at the grain boundaries, variations of PEEM intensity have also been observed among grains. The PEEM intensity of grains, however, does not provide information about the heights of the features, as can be seen from AFM and PEEM images of the same regions (Figure 3.7). Only the small local regions that showed obvious voids in AFM, also exhibited losses in PEEM intensity, likely because those areas were not in focus. Therefore, our PEEM contrast for perovskite thin films, consists of photoemission signal from the valence states that is imaged as grains, plus the edge contrast that outlines the grain boundaries.

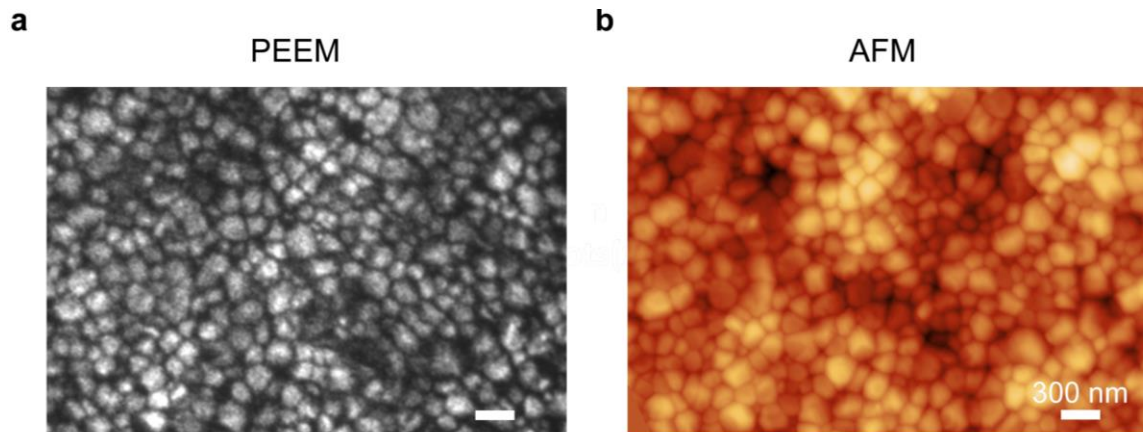


Figure 3.7. Topological contrast in PEEM and AFM imaging. (a) PEEM image of surface microstructure of perovskite thin film. (b) AFM image of surface height variation of the same region of perovskite sample as shown in (a).

3.4. Correlation of surface morphology with defect location

The most essential part of being able to acquire PEEM images of surface morphology, is the ability to accurately correlate them with locations of defects. In PEEM, both images of grains and defects are taken under the same magnification and in the same instrument. This significantly simplifies the superposition of images, since image magnification and resolution issues are eliminated.

To correlate the images of defects and images of grains, we utilized gold fiducial markers as position references. The unique shapes of markers served as guide points for overlaying between different PEEM images of defects and grains.

Below we will discuss how surface morphology correlated with nanoscale defects, as seen from PEEM measurements. In addition to PEEM, we also performed SEM and AFM on the same sample regions and correlated the local morphology with the presence of defects.

3.4.1. Photoemission electron microscopy measurements

PEEM images of defects and grains have been collected according to the procedures described in Section 3.3.1, and overlaid using ImageJ software using gold fiducial markers as position references.

PEEM image of defects taken with 4.65 eV probe, is shown in Figure 3.8a. The image shows nanoscale defects that are colored with blue. The dark areas in the image are pristine. The PEEM image of surface morphology taken with 6.2 eV probe photons from the same area in the sample, is shown in Figure 3.8b. This image visualizes morphology of polycrystalline perovskite sample as grains that are of about 100 nm – 300 nm in sizes. The grain boundaries in this image appear darker as compared to the grains, as has been discussed in Section 3.3.2. Since both images of defects and grains were taken from the same area of the sample, in the same microscope under the same magnification, it is convenient to superimpose these images to learn more about the location of the defects with respect to surface microstructure. For this, we utilized ImageJ software and used gold fiducial markers as position references for the overlay. In Figure 3.8c, we show a superimposed image, where the defects are colored with blue and grains are shown in grey contrast. From this overlay, we found that the smallest defects of just few tens of nanometers in sizes, appeared predominantly at boundaries of morphological grains [47]. For better visualization, in Figure 3.8d, we show a magnified area from the overlaid image in Figure 3.8c that shows a nanoscale defect that is situated at grain boundary.

To further emphasize the position of defects at grain boundaries, we plotted line profiles, where we extracted intensities from PEEM images of grains and defects through the locations of defects (Figure 3.8e) [47]. We clearly observed that the nanoscale defects had highest photoemission intensity at the junction between grains (grain boundary) where the photoemission intensity of grains was lowest.

As has been discussed in Chapter 1, there are a lot of discrepancies in literature regarding the role of grain boundaries. While some reports emphasized on defective nature of grain boundaries, others reported them to be largely benign. In our study, we revealed that only specific grain boundaries were associated with nanoscale defects, which could be one of the explanations to the current inconsistent reports. Additionally, we observed that defects were not

distributed uniformly throughout all the grain boundary, but were rather found as localized clusters. In our study, we did not observe obvious relations between appearance of defects and specific morphological arrangement of grains. For example, we did not find defects to form at the junction of only small-sized grains, or only large grains.

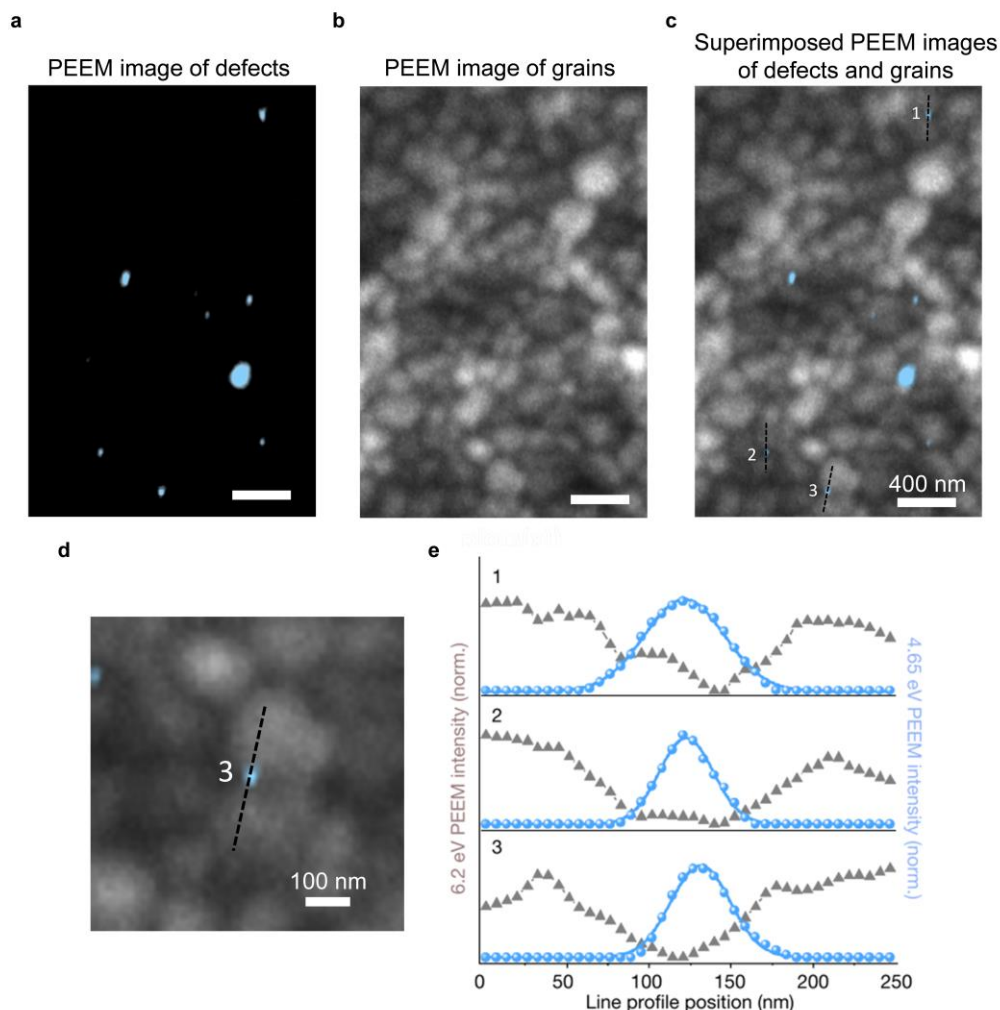


Figure 3.8. Spatial distribution of defects with respect to surface morphology. (a) PEEM image acquired with 4.65 eV probe photons showing nanoscale defects (blue). (b) PEEM image acquired with 6.2 eV probe photons showing grain morphology of the same region of the film as in (a). (c) Superimposed PEEM images of defects (blue) and grains (grey). (d) Magnified region from (c) showing a nanoscale defect situated at boundary between two morphological grains. (e) Line profile of the intensity from the 4.65 eV PEEM image (blue) against the intensity from the 6.2 eV PEEM image (grey). Numbering corresponds to regions of interest in (c).

We performed more in-depth analysis of the overlaid PEEM images and found that while very small defects (of about few tens of nanometers in sizes) were predominantly spatially situated at grain boundaries (“Grain boundary defects” in Figure 3.9a, b), this did not apply to larger defects of few hundreds of nanometers in sizes. We found that those defects were associated with morphological grains (Figure 3.9a, “Intra-grain defects”) [284]. For better visualization, in addition to superimposed images of defects and grains in Figure 3.9a, we show images of just grain morphology and mark the grains that were associated with defects with white dashed circles (Figure 3.9b, “Intra-grain defects”). We thus categorized these defects as intra-grain defects, implying that they were associated with morphological grains.

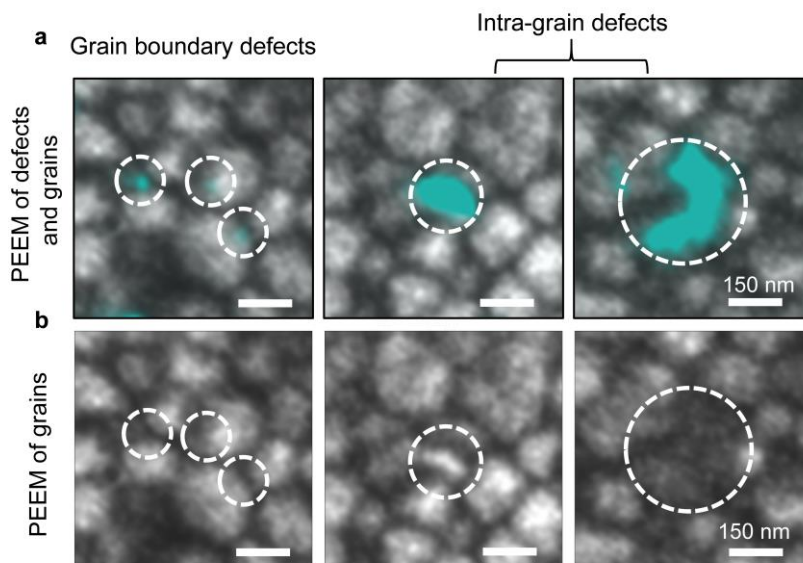


Figure 3.9. Spatial arrangement of nanoscale defect clusters. (a) PEEM overlays of 4.65 eV images of defects (green) and 6.2 eV images of grains (grey). Smaller defects were found to be located at specific grain boundaries (“Grain boundary defects”), while larger defects were associated with entire grains (“Intra-grain defects”). (b) PEEM images of grain morphology. White circles are showing the locations where defects are situated.

3.4.2. Atomic force microscopy measurements

In addition to PEEM imaging, we also utilized other conventional techniques to characterize surface of our perovskite thin films. One of these methods was atomic force microscopy (AFM).

We utilized AFM to (i) image surface morphology of perovskite samples and compare it with PEEM images, and (ii) to assess the local morphological variations (for example, variations in local heights of features) and look for potential relationship to the appearance of nanoscale defects.

By analyzing PEEM and AFM images, we found that morphological grains and grain boundaries imaged with PEEM (6.2 eV probe), correlated well with grains and grain boundaries imaged with AFM (see Figure 3.7). Further, by superimposing PEEM images of defects with AFM images of surface morphology using PEEM images of grains as a guide, we confirmed

that the defects that appeared at specific grain boundaries in PEEM, indeed were located at grain boundaries as imaged with AFM (Figure 3.10) [47]. In general, AFM provides higher level of spatial resolution, on the order of one nanometer, compared to tens of nm in PEEM. It was interesting that in AFM images, we did not observe any clearly visible morphological features associated with grain boundary defects at their specific locations. This shows that grain boundary defects did not form as a result of external precipitation of materials on the surface. We speculate, that these defects, located at the interface of two grains, were very likely related to compositional or structural changes that occurred at the boundary of the adjacent grains. For example, a stressed point could appear and result in local buildup of defects.

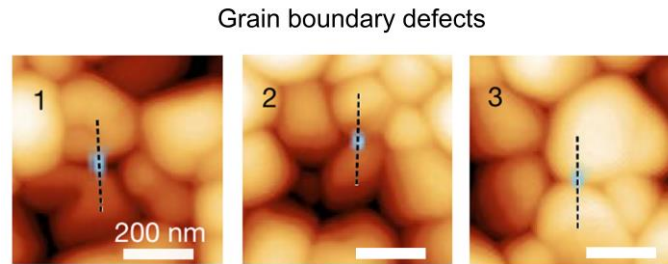


Figure 3.10. Correlation of grain boundary defects with atomic force microscopy. AFM images of grains overlaid with PEEM images of grain boundary defects for the same areas as discussed in Figure 3.8.

We also confirmed that larger defects that we categorized as intra-grain defects in Section 3.4.1, were indeed associated with morphological grains, as we highlight with white dashed circles in Figure 3.11(a and b) [284]. In Section 3.5, we will combine all these observations together with scanning electron microscopy to provide a much clearer and broader picture of various defect types and their origin.

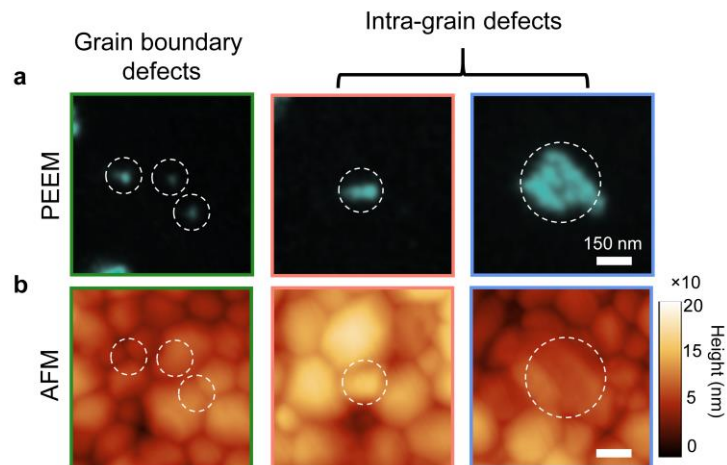


Figure 3.11. Relation of local morphological variations and presence of nanoscale defects. (a) PEEM images of grain boundary (green box) and intra-grain (red and blue boxes) defects. (b) AFM images of the same regions as (a). White dashed circles mark locations of defects.

3.4.3. Scanning electron microscopy measurements

Apart from PEEM and AFM, we also utilized SEM to study our perovskite thin films. SEM provides information about surface topography and composition of the sample. SEM typically uses high electron beam doses and is considered to be a damaging technique for perovskites. Therefore, for our perovskite samples, we conducted SEM characterization as the last measurement to avoid irreversible effects induced by electron beam.

In Figure 3.12a, we show SEM image of perovskite thin film. For comparison, PEEM image of the same region is shown in Figure 3.12b. It is apparent that the topography of grains and grain boundaries imaged with PEEM closely resemble the SEM image. This allowed to easily correlate nanoscale defects and surface morphology in both SEM and PEEM images. Notice that, although we can trace the morphological features in both SEM and PEEM images without any difficulty, the intensity contrast in PEEM differs from the SEM, and should not be directly compared.

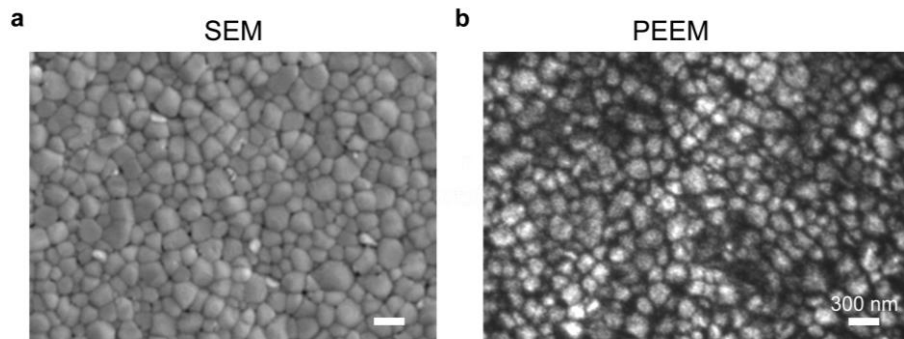


Figure 3.12. Characterization of surface morphology with SEM and PEEM. (a) Images of surface morphology acquired with (a) SEM and (b) PEEM. PEEM topography of grains and grain boundaries follows the SEM image reasonably well. The parts of the film exhibiting low PEEM contrast or poor resolution, can be imaged in SEM with better quality.

To characterize the defects even further, we correlated PEEM images of defects and SEM images of surface morphology. Figure 3.13 shows this correlation for regions associated with grain boundary and intra-grain defects (same regions as shown in Figure 3.11) [284]. For the grain boundary defects, we did not observe any morphological features at the sites of the defects (Figure 3.13a-c, green box). This double confirmed our finding with AFM correlation. For the intra-grain defects, we found that while some of them corresponded to regular morphological grains (Figure 3.13a-c, blue box), other defects were associated with grains that showed brighter SEM contrast (Figure 3.13a-b, red box). Typically, features containing elements with higher Z-numbers, appear brighter in SEM images. This implied compositional heterogeneity associated with these bright grains. From literature reports, it was well-established in perovskite field that such bright crystallites in the SEM images of perovskite films typically originate from inclusions of PbI_2 that are known to form due to excess of PbI_2 in precursor solution [347-349]. The amount of such bright grains has been reported to correlate well with intensity of characteristic PbI_2 XRD peaks [347]. These inclusions are richer in lead as compared to pristine perovskite and therefore, appear brighter in SEM as compared to pristine perovskite grains. Given the iodine-rich composition of our perovskite samples, we attributed grains that showed brighter SEM

contrast to precipitated PbI_2 . Through correlation of PEEM and SEM, we found that one type of intra-grain defects were associated with these PbI_2 grains. We also observed that these PbI_2 inclusions were elevated in height above the perovskite grains, as shown with AFM line scans (Figure 3.13c, red box). In Section 4.4, where we summarize our findings regarding the nature of defects, we will put this finding in context of other measurements and will provide more discussion about defects associated with PbI_2 .

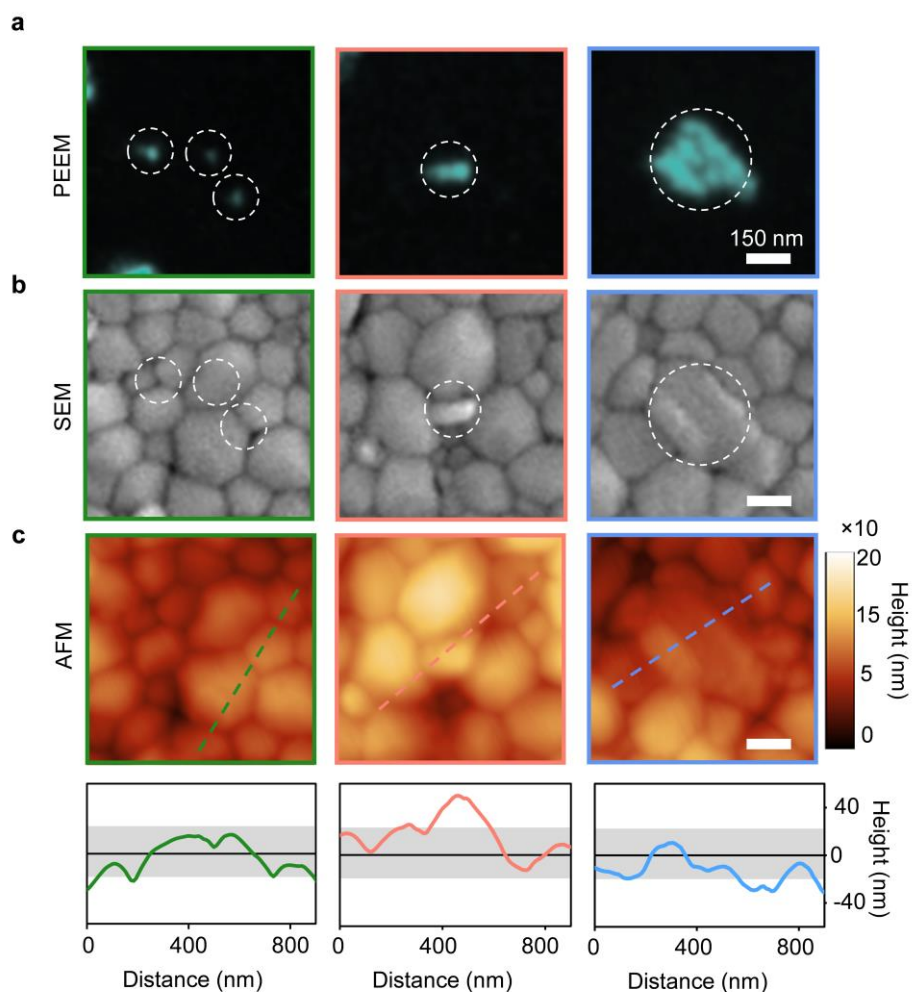


Figure 3.13. Relation of local morphology imaged with SEM to spatial location of nanoscale defects. (a) PEEM images of grain boundary (green box) and intra-grain (red and blue boxes) defects. (b) SEM images of the same regions as (a) with locations of defects marked with white dashed circles for better visibility. (c) AFM images of the same regions as (a and b) with line profiles through the defect clusters indicating the raised height only for some of the intra-grain defects. Solid black line indicates mean height for the sample, with grey shaded area denoting the root mean-square bounds.

3.5. Conclusion

In this Chapter, by employing PEEM, we imaged nanoscale defects in hybrid perovskite thin films. We found that these defects ranged in sizes from few tens to few hundreds of nanometers. We further employed PEEM to image surface microstructure of our perovskite films. By superimposing PEEM images of defects and surface morphology, we found that the smallest defects of just few tens of nanometers in sizes, were predominantly located at grain boundaries. We did not observe these defects to extend along the entire grain boundary, but rather as localized features at the junction between two grains. The larger defects of up to few hundreds of nanometers in sizes, were found to be associated with morphological grains and were categorized as intra-grain defects. Through correlation of PEEM images of intra-grain defects and SEM images of surface morphology, we found their different origins. While some of these defects were associated with regular morphological grains as seen from correlation of PEEM with SEM and AFM, other intra-grain defects corresponded to grains with brighter SEM contrast. Given that such bright grains in SEM images of perovskite films originate from inclusions of unreacted PbI_2 , we attributed one type of intra-grain defects to PbI_2 . In Section 4.4, we will elaborate on this in more detail.

Chapter 4

Photoelectron Spectroscopy of Hybrid Perovskite Thin Films

4.1. Abstract

In Chapter 3, based on PEEM imaging of nanoscale defects and surface morphology of the film, we identified grain boundary- and intra-grain defects in triple-cation mixed halide perovskite thin films. Moreover, we started obtaining insights about the nature of some of these defects and established that intra-grain defects had different origin. To further distinguish between these defects and to understand their energetic alignment, in this Chapter we employ photoelectron spectroscopy (PES) and obtain a nanoscale map of the photoemission spectrum and the local work function at defects sites.

4.2. Photoelectron spectroscopy

With photoemission electron microscope, through spectro-microscopy measurements, we can learn about electronic structures and chemical states of materials. Unlike conventional ultraviolet photoelectron spectroscopy (UPS) that predominantly outputs spatially-averaged spectroscopic data, PEEM allows to map photoemission signal as an image with good level of spatial resolution. This allows to access spectroscopic information of individual small features, such as nanoscale defects.

In order to collect photoelectron spectra in PEEM, one can either perform imaging and collect energy-filtered images, or collect spatially averaged spectrum from selected area at the dispersive plane of the energy filter (appears as a line with modulated intensity). The imaging mode has been briefly discussed in Chapter 3 for imaging defect states and grains in perovskites, and has been widely utilized throughout the work on this thesis.

4.2.1. Energy-resolved imaging of perovskite thin films

Energy-resolved images of perovskite thin films have been collected using photon pulses of 6.2 eV in energy. This photon energy was enough to reach the onset of the valence band and photo-emit electrons from there to the vacuum states. This imaging mode required the use of a hemispherical energy analyzer and an energy slit. The schematic of PEEM with hemispherical energy analyzer is shown in Figure 4.1. The photo-emitted electrons that have different kinetic energies travel between the two hemispheres of an electrostatic energy-filter that are kept at different potentials. Depending on their kinetic energies, electrons are dispersed differently in the analyzer to travel around optimal trajectories. An energy filter or slit, is placed at the end of the analyzer, and only electrons with specific kinetic energies that pass through the slit can arrive at the detector. To vary kinetic energy of the photo-emitted electrons and to control which part of the photoemission spectrum reaches detector, we adjust the sample bias (or start voltage) in the microscope. By varying the sample bias, we can collect images as a function of kinetic energy of photo-emitted electrons. By plotting the intensity modulation of different features from the energy-filtered images, we can analyze for example, the contributions from the valence states, mid gap states, etc. If the probe energy is sufficiently large (synchrotron radiation), it becomes possible to image contributions from specific chemical states and to obtain chemical information about the sample.

Sequence of energy-resolved images of perovskite thin films have been collected with a step of 100 meV in range from -1 to 3 eV (start voltage) around the valence band edge. The energy scale in our plots is corrected by the Fermi level, determined from the high energy cutoff of the photoelectron spectrum taken from fiducial gold marker.

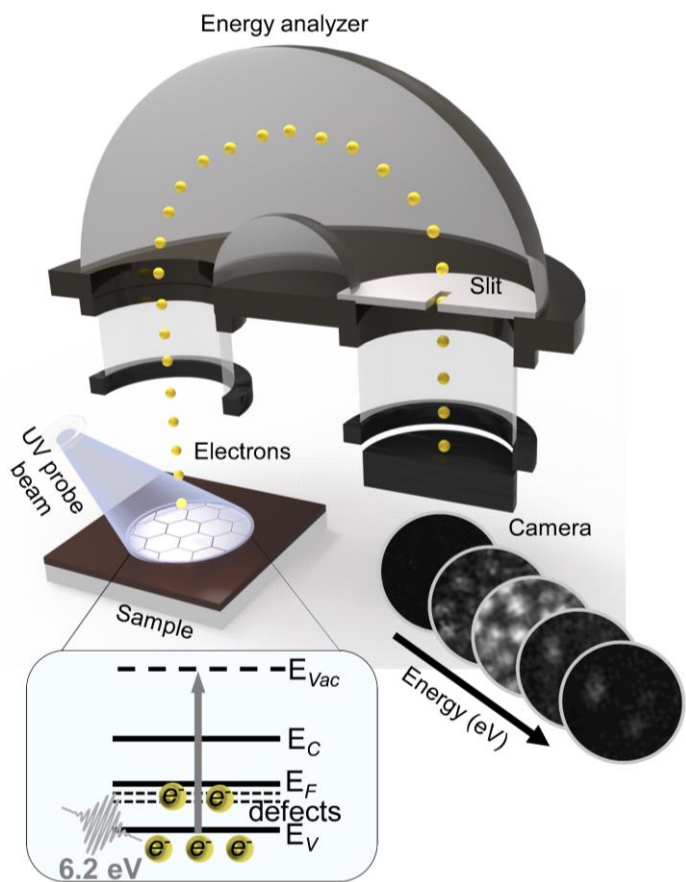


Figure 4.1. Schematic of a spectroscopic PEEM. UV probe pulses cause photoemission of electrons from sample surface; electrons are then accelerated through hemispherical energy analyzer, dispersed in energy, and imaged on CCD camera for each energy. In this way a sequence of energy-filtered PEEM images can be collected. Inset shows energy level diagram of hybrid perovskite: grey arrow indicates transitions from valence band states (E_V) through the defect states (*defects*) below the Fermi level (E_F) to vacuum states (E_{Vac}) upon probing of sample with photons of 6.2 eV in energy.

A sequence of energy-resolved images of perovskite thin film sample, is shown in Figure 4.2. The energy here is presented on $E - E_F$ (eV) scale. At the energies that correspond to the onset of the valence band (from - 2.1 eV to - 1.4 eV), we clearly start observing surface microstructure appearing as grains (highlighted with grey box in Figure 4.2). At the energies closer to the mid gap region (- 1.3 eV to 0 eV), the mid gap states are being probed. These appear in the PEEM image as nanoscale defect-rich clusters, as has been discussed in Chapter 3. For better visibility, the images of defects are highlighted with green box.

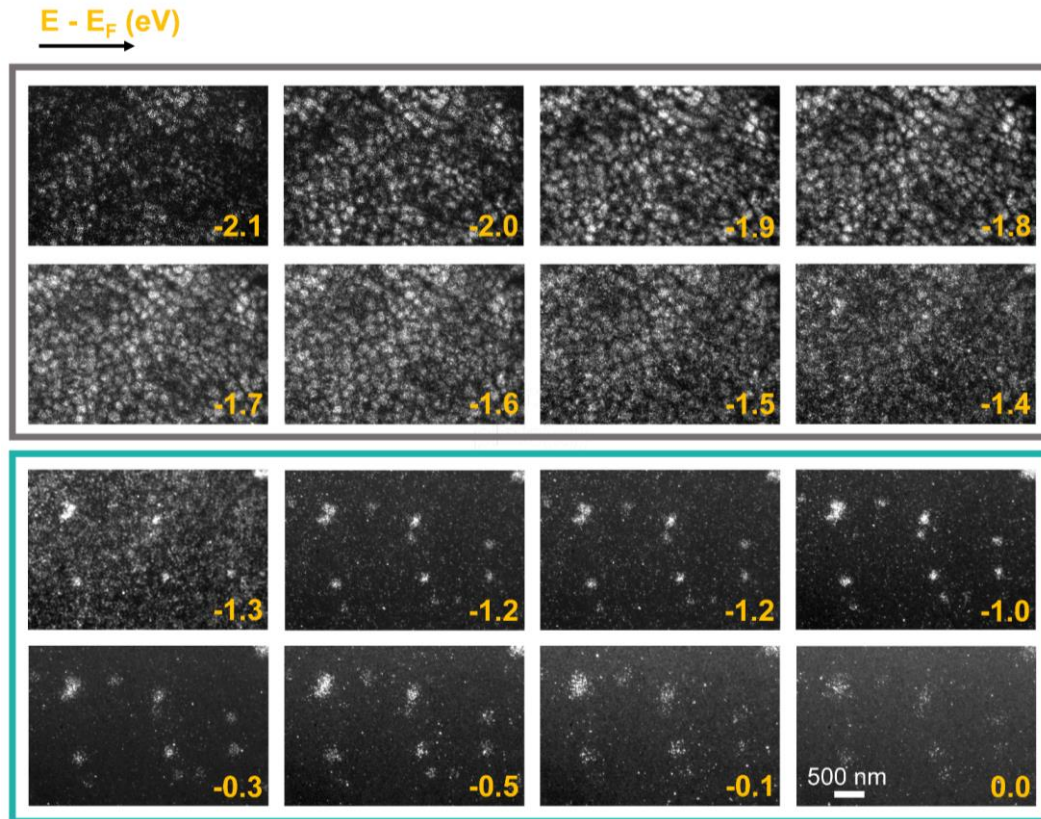


Figure 4.2. Energy-filtered PEEM images of perovskite thin film collected when probing samples with 6.2 eV photons. At the energies from -2.1 eV to -1.4 eV, the contrast shown is due to surface morphology (highlighted with grey box). Localized nanoscale defects appear in images from -1.3 eV to -0.1 eV below the Fermi level (0 eV), and are highlighted with green box. The intensity of each image is scaled independently for better visibility.

To collect energy-resolved images, we utilized the objective ramp script in the imaging software of the PEEM instrument. This script allows to program objective current to automatically adjust at each energy step during the scan to maintain image focus and resolution; otherwise, images at different kinetic energies can de-focus rapidly, which results in loss of spatial resolution.

During photoemission spectro-microscopy measurements, it is important to keep the dose of probe photons low to avoid space charge, which can be seen as spectral broadening in photoemission spectrum and loss of resolution in the image. To avoid this, during the experiments in this thesis, we kept fluence of the 6.2 eV probe photons below 10 nJ cm^{-2} , which we estimated in Chapter 3 to be below the space charge limit. The typical imaging conditions

for collecting energy-filtered images were about 20 seconds exposure per frame, and 4 averages per image.

4.2.2. *Insights into the origin of defects from PES*

From the energy-resolved images of hybrid perovskite sample, we can extract photoelectron spectra that contain energy on one axis and photoemission intensity on another. These spectra provide information about energy distribution of the photo-emitted electrons. Given that energy-filtered images are collected with a good level of spatial resolution, we can extract the photoelectron spectra even from nanoscale areas on the sample. For example, we can plot the photoelectron spectrum for a single grain of the polycrystalline film. This becomes especially useful for differentiating signal from different domains or grains that resulted from spatial heterogeneities in the sample.

Figure 4.3(a, b) shows a typical photoelectron spectrum of pristine region of the triple cation mixed halide perovskite thin film sample. The spectrum represents photoemission from the valence band states starting at $E - E_F$ value of about -1.2 eV. Due to the limitations in probe energy in our setup, we are only able to collect signal from the onset of the valence band. Having even higher energy of probe photons would be useful to obtain chemical information about our samples. The photoelectron spectrum extracted from a single grain (Figure 4.3c), as indicated with red dashed circle in Figure 4.3a, follows well the averaged PES for a larger area. This means that the spectral features of grains are very similar and represent spectral features of pristine perovskite material.

When extracting photoelectron spectrum for region that contains nanoscale defects, as shown from the overlay of PEEM images of defects and surface morphology in Figure 4.3d, we observed appearance of signal from the mid gap states, as indicated in Figure 4.3e. These regions, in addition to the main peak from the valence states, showed a broad spectral feature in the band gap, extending from the valence states edge up to the Fermi level. The magnified part of the PES of the defect-rich region is plotted in Figure 4.3f together with PES of the pristine region. The occupied states extending into the band gap for the defect-rich region, are clearly seen as a characteristic “shoulder” in PES.

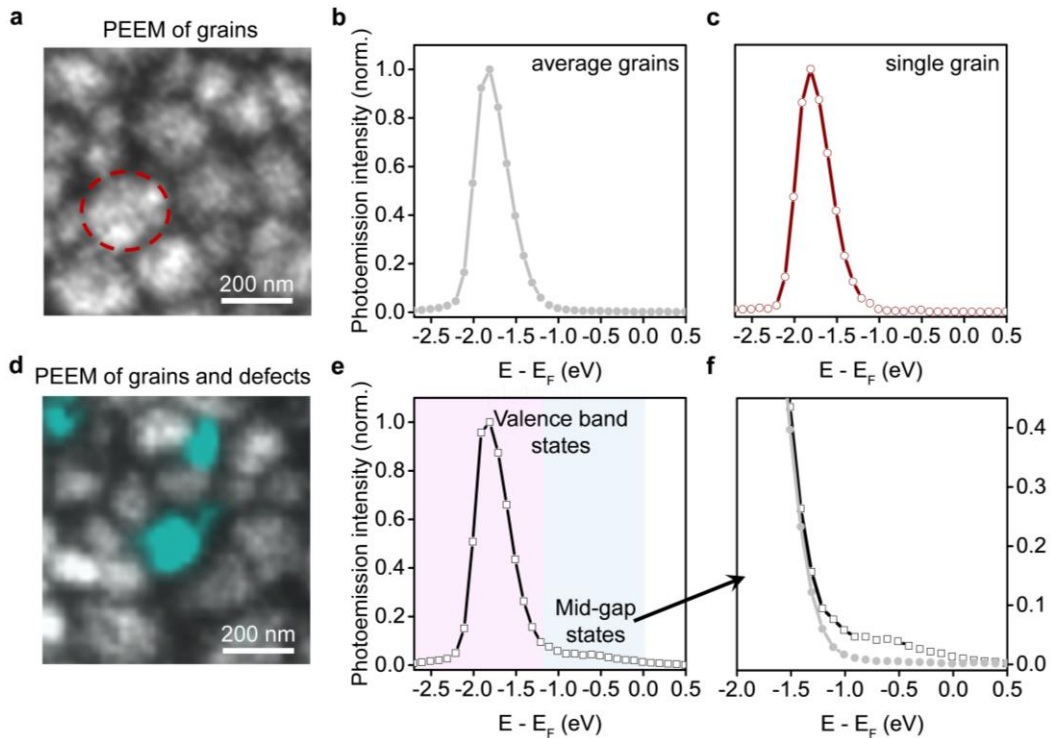


Figure 4.3. Photoelectron spectroscopy of perovskite thin film samples. (a) PEEM image of pristine grains. (b) Averaged PES extracted from the entire area shown in (a). (c) PES of a single pristine grain indicated with red in (a). (d) Overlaid PEEM images of defects (green) and surface morphology (grey contrast). (e) Photoelectron spectrum extracted for the region containing nanoscale defects shown in (d). PES contains contributions from both valence band and mid gap defect states. (f) Magnified part of PES in (e) shown with black line and square, and PES of pristine region in (b) shown with grey line and circle.

By selectively plotting photoelectron spectra of intra-grain defects, we were able to further differentiate between them. In Figure 4.4(a, b and f, g), we show typical PEEM images of intra-grain defects and corresponding SEM images of the same regions. From the photoelectron spectroscopy, we found that the sites of these defects were associated with very different densities of occupied mid gap states, as seen from their photoemission intensities in mid gap spectral region (Figure 4.4c and h). When we correlated these observations with our conclusions from Chapter 3, we found that the defects that we attributed to precipitated PbI_2 , (Figure 4.4 f, g), consistently showed lower photoemission intensity in the mid gap region, as compared to other intra-grain defects. This can be seen from a series of photoelectron spectra plotted for multiple defects of each type in Figure 4.4(d and i), as well as from averaged photoelectron spectra in Figure 4.6. We also found that photoelectron spectrum was characteristic to the type of defect and the sizes of these defects did not dictate their photoemission intensities in mid gap spectral region (Figure 4.4e and j).

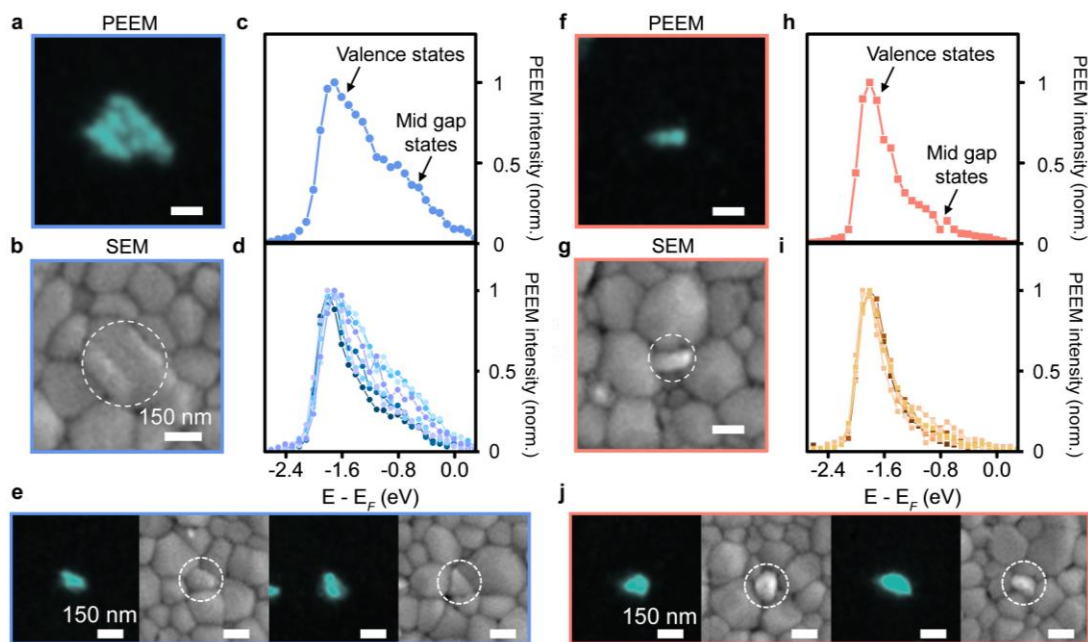


Figure 4.4. Photoelectron spectroscopy of intra-grain defects. Typical (a) PEEM and (b) SEM images and (c) PES (blue line) of intra-grain defect associated with morphological grain. (d) PES of multiple defects as described in (a), showing consistent large density of mid gap states. (e) PEEM and SEM images of additional intra-grain defects similar to (a). Typical (f) PEEM and (g) SEM images and (h) PES (red line) of intra-grain defect associated with grain with brighter SEM contrast. (i) PES of multiple defects as described in (f), showing consistent lower density of mid gap states, compared to (d). (j) PEEM and SEM images of additional intra-grain defects similar to (f).

The photoelectron spectra of grain boundary defects, were distinctly different from the signal plotted for intra-grain defects, and had very low density of occupied states in mid gap region (Figure 4.5). Considering the very small sizes of the grain boundary defects, which were at the limit of our spatial resolution, it was rather challenging to collect photoelectron spectra from these small areas due to limited signal to noise ratio. Nevertheless, when comparing with the signal from the pristine regions (Figure 4.6), the mid gap features at their sites were clearly observed.

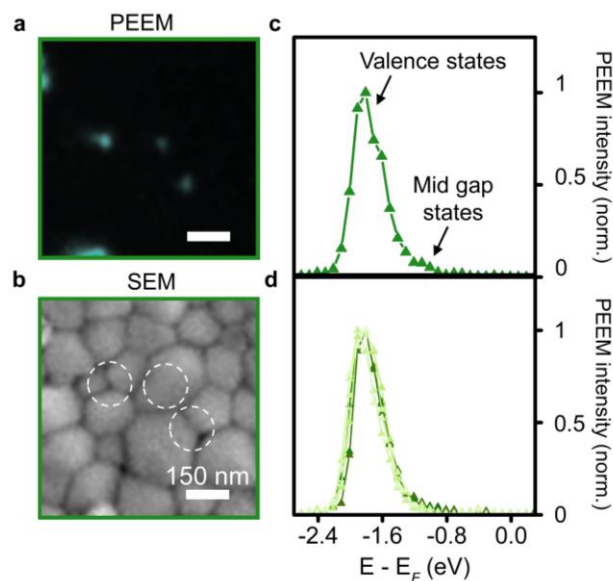


Figure 4.5. Photoelectron spectroscopy of grain boundary defects. Typical (a) PEEM and (b) SEM images of defects that appeared at grain boundaries. (c) PES of the grain boundary defect (green line). (d) PES of multiple grain boundary defects showing low density of mid gap states.

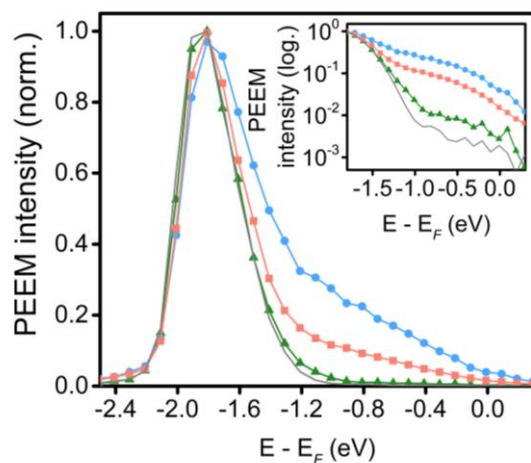


Figure 4.6. Photoelectron spectra for intra-grain (blue and red) and grain boundary (green) defects averaged for multiple features of the same type, as compared to pristine areas (grey). Inset shows contributions from mid gap states on logarithmic scale.

By fitting the photoelectron spectra with Gaussian functions, we can estimate the energy-level positions of nanoscale defects. Typically, analysis of photoelectron spectroscopy data is performed in comparison with theoretical calculations of the partial density of states, as has been done in a number of works [42, 350]. Those reports utilized higher energies of probe photons and performed spatially-averaged conventional ultraviolet photoelectron spectroscopy. These works did not report on appearance of occupied mid gap states in perovskite thin films, likely because such signals would be very weak when compared to contributions from valence states in spatially-averaged spectroscopy. In conventional spatially-averaged UPS, most of the signal would originate from pristine perovskite, and a very low mid gap signal could be interpreted as background or noise. As a result, theoretical models do not usually account for contributions from the defect states when interpreting the photoemission spectroscopy data of hybrid perovskites. It would be useful to compare our data with theoretical models to understand more about the origin of nanoscale defects. However, compared to perovskite compositions with relatively simple unit cell, such as MAPbI_3 or MAPbBr_3 , that are typically used in theoretical works, mixed compositions that we used in this thesis, are much more complex and lack theoretical calculations. Therefore, in this thesis, we used a rather straightforward approach to evaluate the energy distribution of defect states by fitting PES with multiple Gaussian functions. As an extension to current work, it remains an open and interesting direction for us to collaborate with groups who perform theoretical calculations of photoelectron spectra for triple cation mixed halide perovskite thin films. This would provide further qualitative information about the nanoscale defects we found through our PEEM measurements. For example, one could expect the mid gap signal to contain contributions from multiple discrete states. However, given the energy resolution of PEEM in our experiments (125 meV) and spectral signature of these mid gap states, we are likely observing them as a broad spectral features in our photoelectron spectra.

When fitting photoelectron spectra extracted from nanoscale defects, we found that the best fit for all the features was achieved when applying three Gaussian functions. One Gaussian function was used to fit broad contributions from the mid gap states, and provided an estimation of energy level for different defect types, while the rest two Gaussians were used to cover the onset of the valence band. We found that grain boundary and two different types of intra-grain defects appeared at different energies, up to 1 eV above the valence band, as shown in Figure 4.7. This further confirmed different origin of these defects. As briefly discussed in Chapter 1, deep level states in perovskites could be induced by iodine interstitials, lead vacancies and various anti-site substitutions [20, 21]. To fully understand the nature of the defects from our PES measurements, as a follow up to this work, we will require to correlate our results with theoretical calculations. Similarly, PbI_2 has been reported to contain high density of Pb vacancies [351], that could be accumulating on the surface in a form of clusters that we eventually image in PEEM.

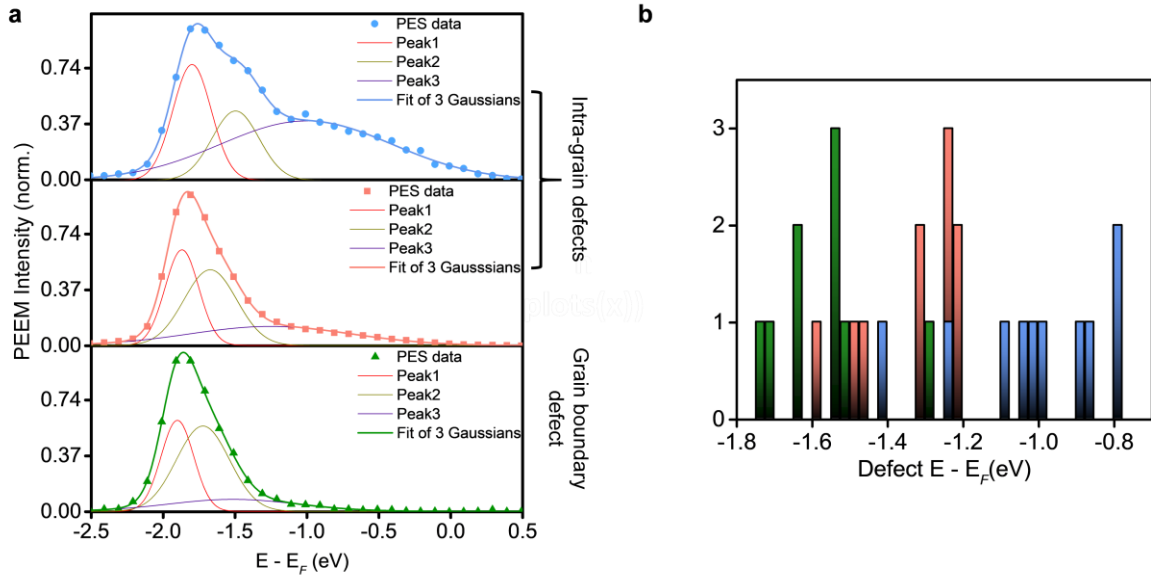


Figure 4.7. Estimation of energy distribution of defects. (a) Gaussian fits (red, yellow, purple) to the photoelectron spectra for selected defects used to estimate peak energy of the mid gap states. (b) Estimated $E - E_F$ of the mid gap states for different types of defects based on fitting: grain boundary-, PbI_2 and another type of intra-grain defects are represented with green, red and blue bars, respectively.

4.3. Energetic variations at defect sites

To further characterize the nanoscale defects, we looked into spectral differences between defect sites and surrounding grains. Interestingly, we found different energetic landscape associated with intra-grain defects as compared to the surrounding pristine regions. This can be seen from comparison of photoelectron spectra extracted from a defect site and from a grain located right next to it (Figure 4.8). By looking at the cutoff energies, that represent work function, we found shifts in local work function for the defect sites as compared to pristine grains. The work function shifts in surface science are typically related to differences in chemical composition, alternative phases, crystallographic orientation, or adsorption of molecules and gases.

From photoelectron spectra, the work function (Φ) is calculated by subtracting the cutoff energy (E_{cutoff}) from the energy of the incident photons $h\nu$ (Equation 4.1).

$$\Phi = h\nu - E_{cutoff} \quad (4.1)$$

We analyzed work function differences between the pristine grains and defect sites, and observed shifted values for local areas that correlated with intra-grain defects (Figure 4.8, blue and red boxes). This implied that very likely those defective grains were associated with local heterogeneities in composition, structure or orientation, and likely could not be considered pristine perovskite. The amount of this work function shift varied for different intra-grain defects. For example, the intra-grain defects that we prior attributed to precipitated PbI_2 , showed rather smaller changes in work function when compared to other intra-grain defects. For the much smaller grain boundary defects, given their small sizes which were at the limit of our spatial resolution, we did not observe obvious changes in work function, as compared with surrounding grains (Figure 4.8, green box).

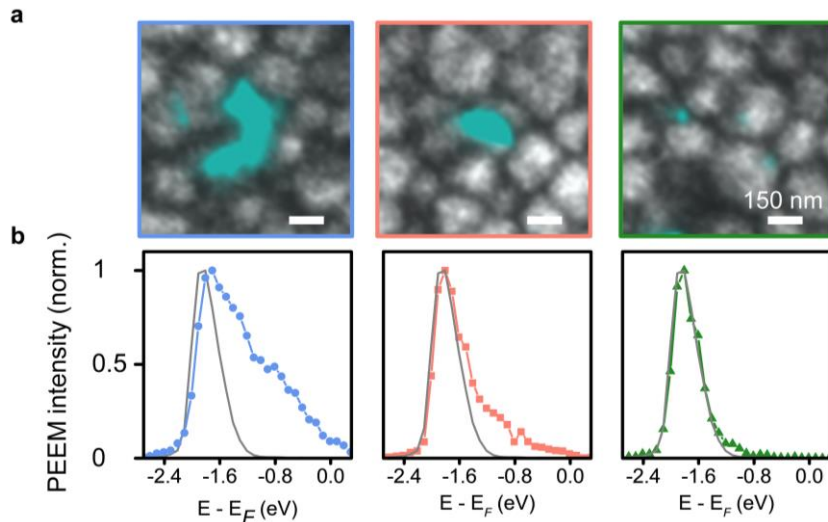


Figure 4.8. Photoelectron spectroscopy of grains and nanoscale defects. (a) Overlaid PEEM images of grains and defects. (b) Photoelectron spectra of defect sites and pristine grains. For some of the intra-grain defects shifted cutoff energy was observed.

In order to access the work function information on the spatial scale, we developed a way to map the changes in work function from the energy-filtered PEEM images. For this, we considered only a part of the photoelectron spectrum, to avoid contributions from the mid gap states, and developed a procedure to record value of cutoff energy, which we then subtracted from the incident photon energy to plot work function.

To obtain maps of work function, we have extracted PES from each pixel from the stack of energy-filtered images, and performed fitting with a Gaussian function. We determined position of the secondary edge cutoff (Figure 4.9a, b) and calculated work function according to the Equation 4.1. The plotted two-dimensional image is shown in Figure 4.9c. As a control, we also plotted an amplitude map generated during Gaussian fitting (Figure 4.9d). This amplitude map is composed of the maximum intensity for each pixel and should match the PEEM image collected from the valence band edge. Our amplitude map followed the image of surface morphology reasonably well, which showed successful fitting for every pixel. The 2D maps of work function directly showed energetic heterogeneities in perovskite film and served as a helpful tool to analyze larger amounts of data, as we did not need to plot large amount of photoelectron spectra for each region of interest.

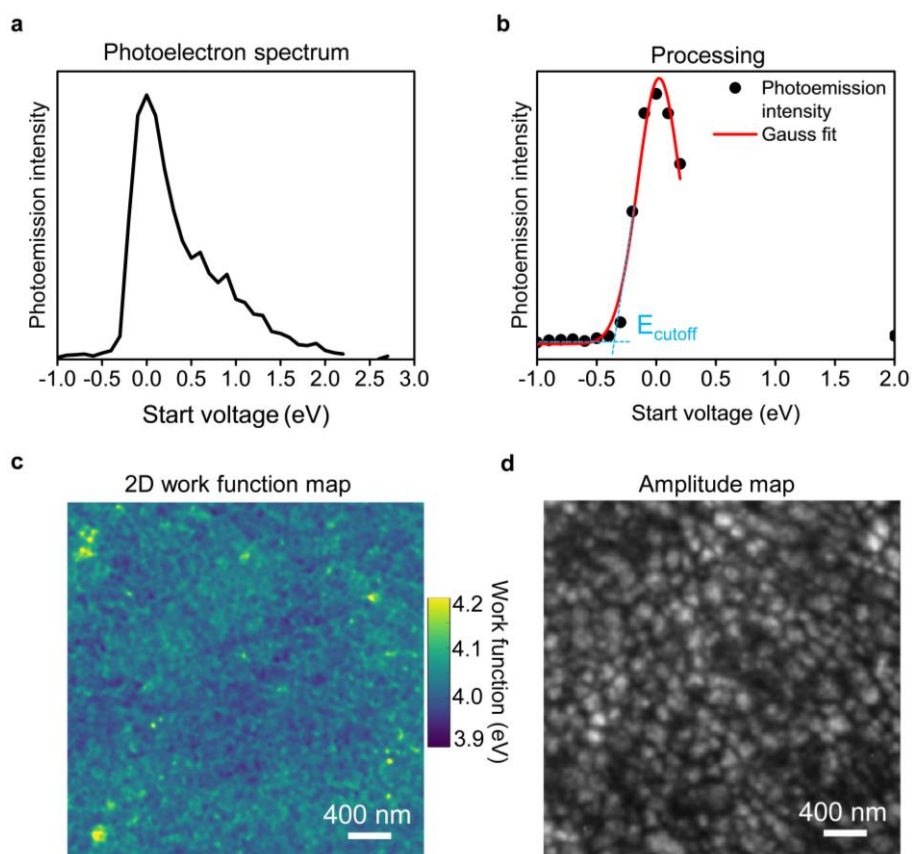


Figure 4.9. Plotting two-dimensional work function maps. (a) Photoelectron spectrum extracted from energy-filtered images of perovskite thin film. (b) Processing steps to determine cutoff energy and calculate work function. (c) Work function map plotted for an area of perovskite thin film of about 3 μm by 3 μm . (d) Amplitude map that follows grain morphology, generated during the processing.

By comparing PEEM image of defects and map of work function, we found that the work function was relatively homogeneous for pristine regions (Figure 4.10a). In contrast, at the sites associated with intra-grain defects, we found clear variations in work function compared to the pristine regions, as has been prior identified from PES plots in Figure 4.8. In Figure 4.10b, we show overlaid PEEM images of defects and grains next to work function maps plotted for the same areas. The sites of the intra-grain defects were clearly associated with elevated values of work function, as marked with white dashed circles. We also confirmed that intra-grain defects that were associated with PbI_2 (Figure 4.10b, red box), showed smaller increase in work function as compared with other intra-grain defects (Figure 4.10b, blue box). Given the small sizes of the grain boundary defects, and small local variations of the work function, we were not able to observe clear signatures of heterogeneities in work function associated with the grain boundary defects (Figure 4.10c).

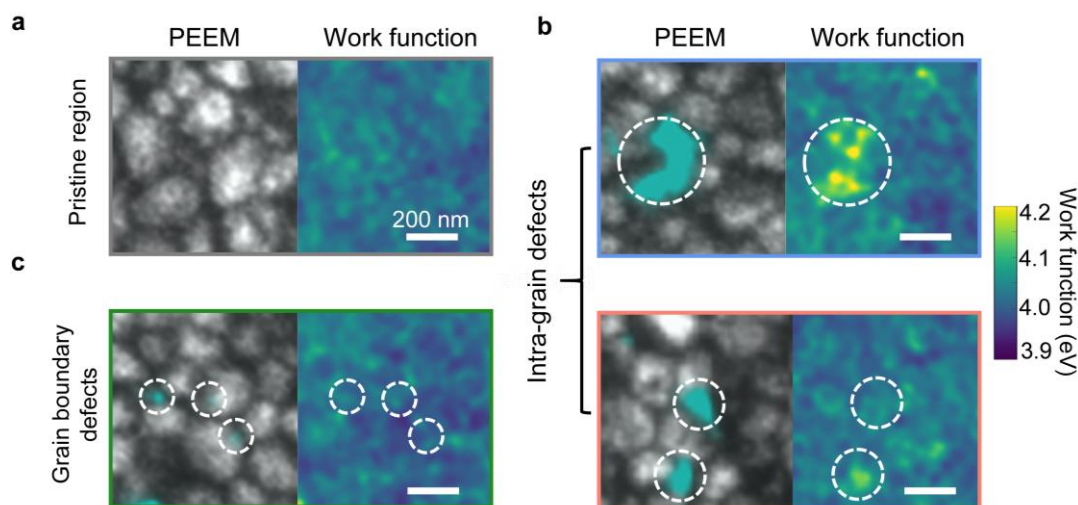


Figure 4.10. Correlation of defects and local work function. (a) PEEM image and work function map of a pristine region of perovskite thin film. (b) Overlaid PEEM images and work function maps of regions associated with intra-grain defects. (c) Overlaid PEEM images and work function maps of regions associated with grain boundary defects. White dashed circles are outlining locations of nanoscale defects.

4.4. Conclusion

To conclude, in this Chapter, we employed energy-resolved imaging with PEEM to obtain photoelectron spectra of nanoscale defects. We found that intra-grain defects had very different spectral signatures, as seen from the photoemission intensity in mid gap region. In particular, we observed that defects that we previously attributed to PbI_2 , had consistently lower density of mid gap states, compared to other intra-grain defects, which further corroborated the different origins of intra-grain defects. We also plotted local work function variation and found that compared to pristine film, intra-grain defects were associated with local increase in work function which allowed us to gain confidence that all the intra-grain defects were associated with some compositional or structural heterogeneity.

Before we move to the next chapter where we employ time-resolved measurements and discuss the roles of defects in charge carrier trapping, we will briefly summarize our findings about nanoscale defects in hybrid perovskite thin films we obtained thus far. By utilizing PEEM, we imaged nanoscale defects in hybrid perovskite thin films. Based on morphological location with respect to surface microstructure, we categorized the imaged defects into grain boundary and intra-grain defects. By combining PEEM and SEM, we attributed some of the intra-grain defects to precipitated PbI_2 . Via photoelectron spectroscopy measurements, we found that other type of intra-grain defects that were associated with morphological grains, showed elevated work functions and high density of mid gap states. The grain boundary defects appeared at the junction of two grains and based on SEM and AFM characterization, did not show morphological features associated with their locations, except of the grain boundary itself.

Outside of the scope of this thesis, but nevertheless important, is the work done in parallel by our collaborators from Stranks group at the University of Cambridge, who worked on applying synchrotron-based microscopy tools, such as nano X-ray diffraction (nXRD) to study hybrid perovskite thin films. By combining PEEM and nXRD results, we correlated local structural information with nanoscale defects. We confirmed that some of the intra-grain defects corresponded to PbI_2 and found that other intra-grain defects, were associated with 6H hexagonal polytype perovskite phases [284], consistent with energetic heterogeneity associated with these defects observed through our photoelectron spectroscopy measurements. The grain boundary defects, due to their small sizes, could not be studied and indexed conclusively due to limitations in spatial resolution of both PEEM and nXRD. Accessing structural information at these sites would likely require utilization of techniques approaching atomic scale resolution. In the following Chapters of this thesis, with the purpose of differentiating between intra-grain defects, we will be referring to them as PbI_2 and polytype defects, when applicable.

It still remains interesting to further research these defects, especially by employing techniques with atomic scale resolution. In particular, correlation of PEEM with transmission electron microscopy would be an enlightening follow up to our work. Such measurements would allow to study atomic arrangements associated with grain boundary defects and to further understand structural information of intra-grain defects. Given that literature reports typically emphasize on large densities of point defects in hybrid perovskites that are involved in charge trapping, ion migration, likely even phase segregation in multi-cation and mixed halide perovskites [11, 298, 352], it would be interesting to understand whether through our PEEM measurements, we are imaging clusters of point defects, or higher-dimensional defects such as dislocations and stacking faults, or some combination of both.

Chapter 5

Time-resolved Photoemission Electron Microscopy of Hybrid Perovskites

5.1. Abstract

After having uncovered the presence of multiple types of defects in triple cation mixed halide perovskite thin films, the next important question was addressing the roles of these defects in performance of perovskite films. In particular, we were interested in exploring the roles of these defects in charge carrier trapping that leads to non-radiative losses. Given that charge trapping is a very fast process, we would require utilization of techniques that allow us to obtain information in the temporal domain. At the same time, given the nanoscale nature of these defects, it is important to utilize tools with high spatial resolution. In this Chapter, we employ time-resolved photoemission electron microscopy that combines spatial resolution of photoemission electron microscope and temporal resolution of optical pulses to record spatio-temporal charge trapping dynamics in hybrid perovskite thin films. We specifically look into response of different types of defects to establish their particular roles in non-radiative recombination.

5.2. TR-PEEM imaging considerations

The presence of defects has been previously linked to non-radiative recombination due to charge trapping, and a number of studies have been conducted to understand this channel of performance losses [5, 6, 9, 13, 301]. The methodologies utilized, often report on spatially-averaged dynamics or on spatially-resolved information in the steady state [5, 208]. For example, ultrafast spectroscopy measurements have no spatial resolution and typically attribute either changes in carrier dynamics or observation of spectral features to presence of performance-limiting defects [14, 15, 301]. Given the presence of various types of nanoscale defects in perovskite absorbers, it is important to utilize tools that allow to study recombination processes with good spatial resolution. Moreover, given the ultrafast nature of charge trapping that is expected to occur at nanosecond timescales or faster, it becomes equally as important to have access to probes that are very short in time in order to capture the charge trapping dynamics at defective sites. TR-PEEM that combines spatial resolution of PEEM and temporal resolution of optical pulses, will serve as an excellent tool to study charge trapping dynamics in hybrid perovskite thin films in both space and time.

In TR-PEEM, as has been discussed in Chapter 2, prior to sending an ultrafast probe pulse, sample is photo-excited with a pump pulse that promotes electrons from the valence band states to the conduction band states. Following that, we can monitor the response from selected parts of the energy spectrum with time-delayed probe pulse. For example, we can record the response of either excited state or ground state of the material, or as in the case of our perovskite samples, we can trace the changes from the defect states. To do so, one would collect PEEM images of defects before and after the photoexcitation at different time delays between pump and probe. By further analyzing changes in PEEM intensities through this sequence of PEEM images, one can monitor the evolution of time dependent photoemission signal at regions of interest.

A schematic of TR-PEEM experiment together with the energy-level diagram of perovskite sample at the instance of photo-excitation is shown in Figure 5.1. A near-infrared pump photons have been selected to photo-excite perovskite at the absorption edge.

During TR-PEEM experiment, we recorded PEEM images of defects at each time delay between pump and probe. TR-PEEM images for each time delay have been generated by subtracting images acquired at negative time delays from images acquired at positive time delays. This allowed to visualize movies of charge carrier trapping at nanoscale defects in perovskite thin films. To ensure that the observed dynamics were not originating from instabilities of laser intensity during the measurement, we normalized the intensity of each of the recorded images by the signal from gold fiducial marker, which was found to show no dependence on delay between pump and probe.

The typical imaging conditions for TR-PEEM images were 1 second exposure and 64 averages per frame (1 delay step). We found that given the sensitive nature of these measurements, and the very small signal we were expecting to observe, one required sufficient amount of averaging for each time delay and subsequently many repeated scans to ensure that we collected good quality signal. Scans have been repeated at least 4 times, and final images are result of 4 averages.

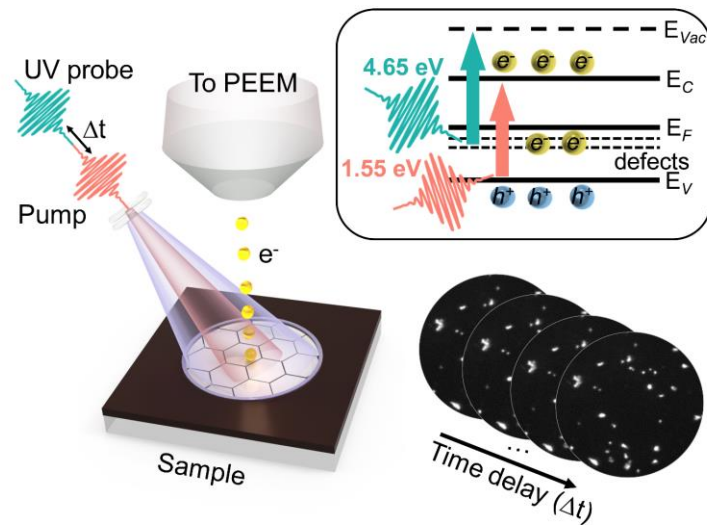


Figure 5.1. Schematic of time-resolved PEEM experiment of perovskite sample. Inset shows energy-level diagram of perovskite sample at the instance of photo-excitation. Incident pump photons (*pump*) promote electrons in perovskite from valence band states (E_V) to the conduction band states (E_C). The time-delayed UV probe photons (*UV probe*) photo-emit electrons from defect states (*defects*) below the Fermi level (E_F) to the vacuum level (E_{Vac}). For each time delay between pump and probe, a PEEM image is recorded.

The fluence of 1.55 eV pump photons for TR-PEEM measurements was chosen to be of about $100 \mu\text{J cm}^{-2}$. Given the rather low absorption at this wavelength for mixed-halide samples, this approximately translates to carrier density of $\sim 10^{16} \text{ cm}^{-3}$. The probe photon fluence was kept below 100 nJ cm^{-2} for 4.65 eV photons. It is very important to have a good control over pump and probe fluences to not overexpose sample with either UV probe light or near-infrared pump, which could damage the sample. For example, high doses of pump could cause heating of the sample and induce new defects or increase photoemission intensity from the mid gap states. Similarly, high dosages of UV light have been also reported to be harmful for perovskites as well [353]. Therefore, very careful attention should be paid to doses of both pump and probe photons while performing TR-PEEM.

5.2.1. TR-PEEM imaging of perovskite thin films

During TR-PEEM of hybrid perovskite thin films, by monitoring modulation of photoemission intensity from mid gap states after photo-excitation, we can track changes in their carrier population and thus follow the trapping dynamics. In particular, we expect one of the following three scenarios to take place: (i) no changes in PEEM intensity, (ii) increase in PEEM intensity and (iii) decrease in PEEM intensity. Each of these can be interpreted through the changes in population of mid gap states occurring due to charge trapping.

The case of (i), when no changes in PEEM intensity have been recorded, implies absence of charge carrier trapping. When the population of states is invariant to the photo-excitation, we expect trapping to either not take place at all, or to take place at timescales far beyond the

timescales measured in our experimental set-up. In the case (ii), an increased photoemission signal from the defect states, indicates a rise in population of electrons in those states, and can be interpreted as trapping of electrons. And finally, in case (iii), the decrease in photoemission signal can indicate reduced population of electrons in the mid gap states, and could be interpreted as trapping of photo-excited holes.

To compare charge carrier trapping for various regions of interest, *e.g.*, from pristine perovskite or from different types of defects, we constructed movies recording changes in photoemission intensity for specific time delay steps after photo-excitation (Figure 5.2). For better visualization, we colored negative change in PEEM intensity with blue, and positive with red. The first striking observation was lack of changes in photoemission intensity at pristine regions that did not contain mid gap states (Figure 5.2, “Pristine region”). In contrast, we detected very localized changes in photoemission intensity from nanoscale defects. In particular, the sites of intra-grain defects associated with polytype grains, showed pronounced hole trapping behavior as seen from the decreased photoemission intensity (Figure 5.2, “Polytype defect”). Similarly, we found that the grain boundary defects also demonstrated hole trapping behavior (Figure 5.2, “Grain boundary defect”). Moreover, despite their small sizes of just few tens of nanometers, grain boundary defects showed more pronounced trapping as seen from larger percent change in photoemission intensity. Interestingly, the intra-grain PbI_2 defects, did not demonstrate obvious changes in photoemission intensity (Figure 5.2, “ PbI_2 defect”) making them relatively benign from perspective of trapping charges generated in pristine perovskite. The trapping by the PbI_2 defects could be inhibited due to energetic or morphological/height barrier between PbI_2 and perovskite.

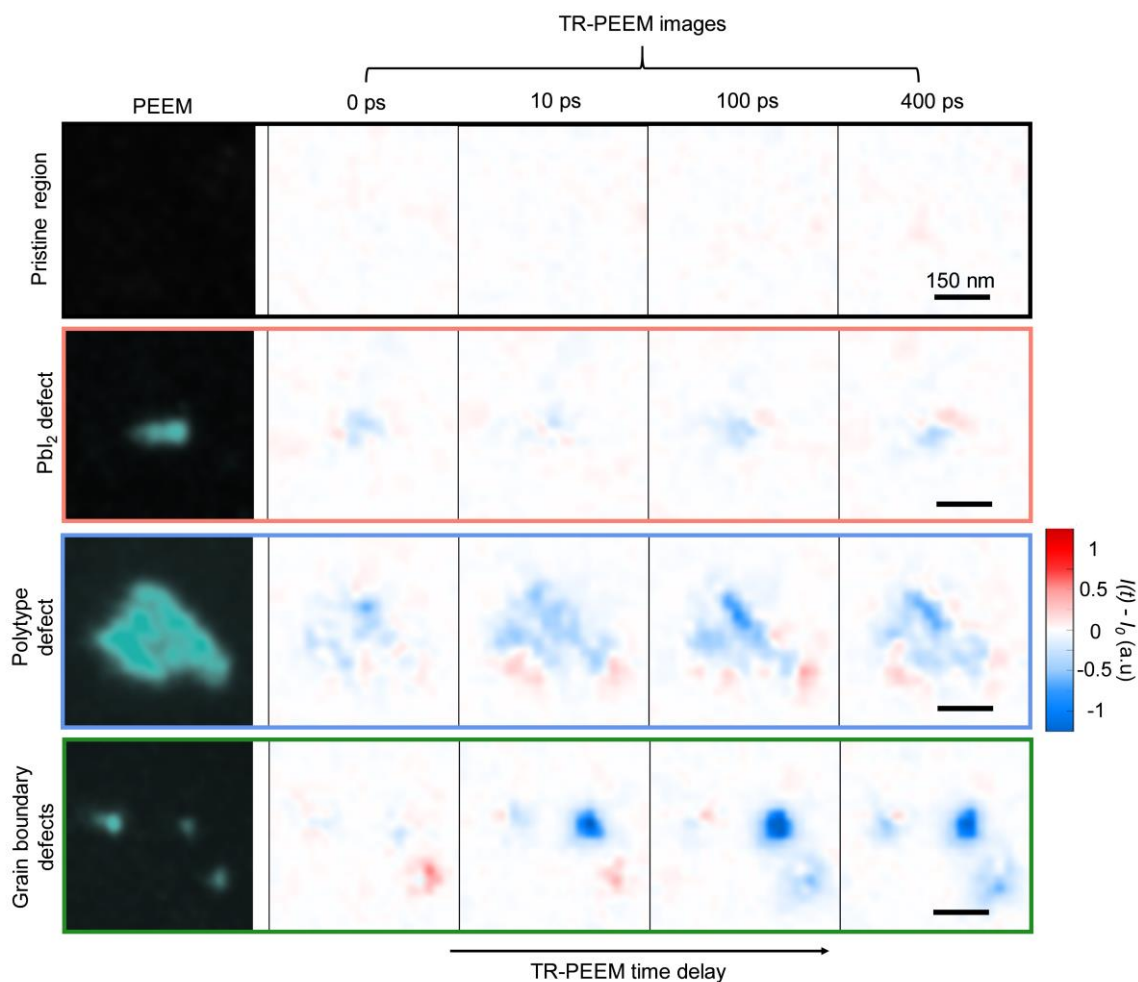


Figure 5.2. Time-resolved PEEM images of perovskite thin film. For pristine regions that were not associated with nanoscale defects, no changes in photoemission intensity were observed after photo-excitation, implying absence of charge trapping. The defects associated with precipitated PbI₂, did not demonstrate any obvious signs of charge trapping upon photo-exciting perovskite, while the intra-grain polytype- and grain boundary defects, showed clear hole-trapping signal as seen from reduction of photoemission intensity at their sites. Color scale indicates change in PEEM intensity ($I(t) - I_0$): blue color denotes reduction in photo-emission intensity, while red color – increase in photoemission intensity.

5.2.2. TR-PEEM trapping dynamics

To evaluate trapping dynamics, we extracted photoemission intensities for different types of defects as a function of time delay between pump and probe. We normalized the extracted intensities to intensity of gold fiducial marker to remove laser fluctuations. Subsequently, the extracted signals were averaged between multiple defects of the same kind (grain boundary and intra-grain PbI_2 and polytype defects, respectively) and plotted as percent change $((I(t) - I_0)/I_0 \times 100)$ in photoemission intensity versus pump-probe time delay.

The pristine regions of the film that were not associated with defects, did not respond to photoexcitation, as seen from Figure 5.3a. Similarly, we also did not observe response from the PbI_2 defects upon photo-exciting perovskite (Figure 5.3b), as discussed in Section 5.2.1. The rest intra-grain and grain boundary defects, participated in carrier trapping as seen from reduction in photoemission intensity after photoexcitation. Moreover, there were important differences between the two. The grain boundary defects showed larger change in PEEM intensity after photoexcitation (Figure 5.3c), indicating their significant cross section for photo-hole capture. For this defect type, we used double exponential decays (Equation 5.1) to estimate their trapping dynamics. We obtained two time constants of ~ 6 ps and ~ 290 ps, suggesting a local, fast trapping processes followed by a slower diffusion-assisted trapping, in agreement with our previous findings [47]. By attributing the fast time constant from TR-PEEM fitting to rapid trapping of charges nearby the defect site, and slower component to diffusion of charges to the defect site, we can estimate trapping diffusion length according to the equation $L_T = \sqrt{D\tau_T}$. Given diffusion coefficient D of about $0.2 \text{ cm}^2 \text{ s}^{-1}$ [54] and τ_2 of 290 ps, we can estimate the L_T to be on the order of ~ 80 nm, which approaches the grain size. In contrast, polytype defects showed much smaller TR-PEEM response with only a fast exponential decay (Equation 5.2) observed within our experimental window (Figure 5.3d). This indicates, that diffusion-assisted processes here, if present, were weaker and slower.

$$y(t) = A_1 \times [\exp(-t/\tau_1) - 1] + A_2 \times [\exp(-t/\tau_2) - 1] \quad (5.1)$$

$$y(t) = A_1 \times [\exp(-t/\tau_1) - 1] \quad (5.2)$$

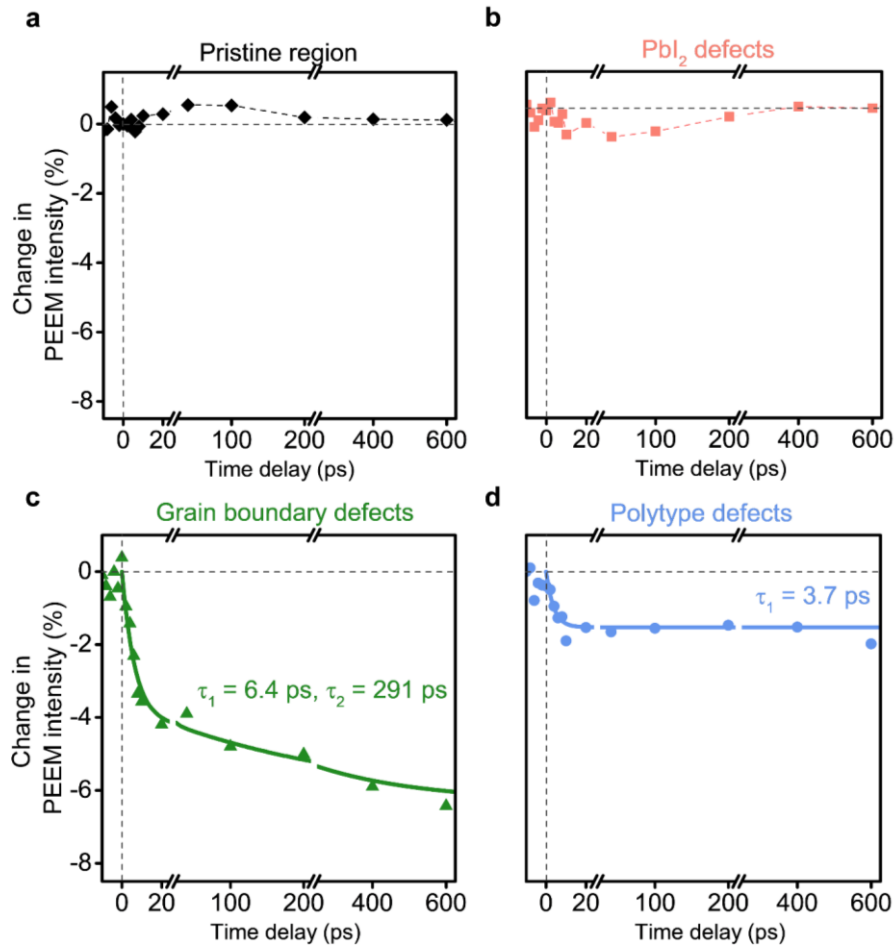


Figure 5.3. Time-resolved PEEM dynamics. TR-PEEM decay curves plotted as percentage change in PEEM intensity after photoexcitation ($[I(t) - I_0]/I_0 \times 100$) versus pump–probe time-delay for (a) pristine region, (b) PbI_2 defects, (c) grain boundary defects and (d) intra-grain polytype defects. Solid lines represent exponential decay fits.

5.3. Correlation with steady-state photoluminescence losses

We employed confocal photoluminescence microscopy to understand how the defects imaged in PEEM would relate to local variations in photoluminescence. For this, we first imaged the defects in PEEM with 4.65 eV photons and subsequently performed photoluminescence mapping of the same area of the sample using 532 nm laser excitation source. We specifically looked into local variations of photoluminescence intensity associated with different types of defects.

In Figure 5.4a, we show PEEM image of defects that was superimposed with map of photoluminescence intensity in Figure 5.4b. We immediately saw that photoluminescence intensity was inhomogeneous and regions with poor photoluminescence correlated reasonably well with locations of defects. In Figure 5.4c, we show magnified images for different regions of interest including one pristine region and several areas containing nanoscale defects. The pristine region of the film showed high photoluminescence count, consistent with absence of TR-PEEM signal, indicating lack of charge trapping processes. At the sites of PbI_2 defects, we observed very small localized photoluminescence losses (Figure 5.4c, red box). Given that from TR-PEEM measurements, we established that PbI_2 defects did not participate in trapping of photo-excited holes from perovskite, we attributed these photoluminescence losses to occur largely due to presence of non-perovskite material. We note, however, that there remains a possibility for electrons from perovskite to be trapped by PbI_2 defects at time scales beyond our TR-PEEM measurements. Therefore, we cannot exclude this potential pathway of non-radiative recombination to also impact photoluminescence intensity at regions associated with PbI_2 defects.

At the regions associated with the grain boundary defects (Figure 5.4c, green box), we observed the impact of diffusion assisted trapping that we established earlier through TR-PEEM measurements. The photoluminescence intensity here was depleted over a large area beyond the defect site, consistent with presence of slow trapping component in TR-PEEM measurements that we have attributed to diffusion of charges to defects. It is important to note that the probing depth of photoluminescence measurements is much larger than PEEM, therefore, we can expect carriers generated in bulk of material to also contribute to charge trapping and non-radiative recombination. This implies that to model the diffusion-assisted trapping, we would have to consider both lateral and vertical diffusion. Furthermore, it is also an interesting observation from different perspective: PEEM is a surface-sensitive technique and therefore, we cannot probe and make assumptions about the bulk of material. However, we cannot exclude possibility of charges from the bulk to diffuse to the defect sites that are close to surface. The photoluminescence depletion associated with defect sites, could be a reasonable experimental observation of such an effect. Therefore, being conventionally a surface-sensitive technique, TR-PEEM can still provide clues about bulk-related processes.

Finally, the correlation of PEEM images of defects and photoluminescence microscopy maps showed that the intra-grain polytype defects were also associated with depleted photoluminescence intensity (Figure 5.4c, blue box). This was in agreement with TR-PEEM measurements that identified polytype defects to have charge trapping nature.

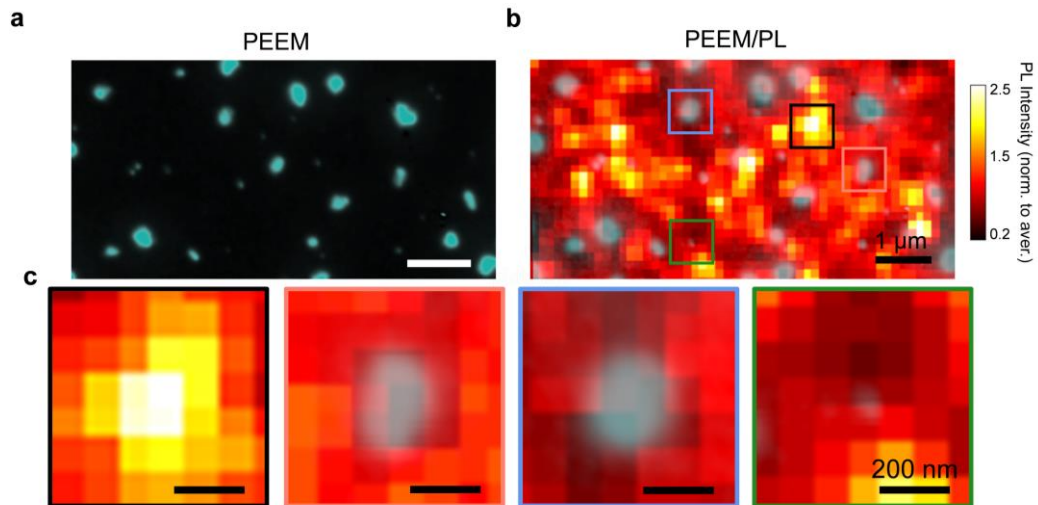


Figure 5.4. Correlation of PEEM and photoluminescence maps. (a) PEEM image of nanoscale defects. (b) Photoluminescence intensity map overlaid with PEEM map of defects for the same region as (a). (c) Magnified regions of interest as indicated with color-coded boxes in (b), showing overlaid PEEM/PL maps of pristine region (black box), region associated with PbI_2 defect (red box), intra-grain polytype defect (blue box) and grain boundary defect (green box).

Note that the resolution of the PL microscopy here is at the diffraction limit, which can cause complications when correlating with PEEM images that have much better spatial resolution. However, in past, we also performed PL microscopy on perovskite samples with Leica STED super-resolution fluorescence microscope that can overcome the diffraction limit and achieve up to 50 nm spatial resolution [47]. Using Leica STED microscope, we still observed extended PL losses correlating with defect sites [47].

5.4. Conclusion

In this Chapter, we employed time-resolved photoemission electron microscopy to investigate the roles of the nanoscale defects in performance of perovskite thin films. By recording the spatio-temporal charge trapping dynamics for different defects, we found that depending on their nature, they played varied roles in photo-excited hole trapping. Grain boundary defects, despite their small sizes of about few tens of nanometers, exhibited large reduction in photoemission intensity after photo-excitation, indicating their significant cross section for capturing holes. Their TR-PEEM dynamics exhibited two time constants, suggesting a fast trapping process, followed by a slower diffusion assisted trapping process. Photoluminescence maps around the grain boundary defects showed the impact of diffusion assisted trapping – the photoluminescence intensity was depleted over the large area around the defect site. For the intra-grain polytype defects, the TR-PEEM response was weaker with only a fast-exponential decay observed within our measurement window. This indicates that diffusion-assisted processes here, if present, were weaker and slower. Consistent with this, photoluminescence maps at regions associated with intra-grain polytype defects, also showed photoluminescence losses. In contrast, the intra-grain defects associated with precipitated PbI_2 , did not show obvious changes in photoemission intensity after photo-excitation of perovskite, indicating that these defects were relatively benign from perspective of trapping photo-generated charges in pristine perovskite. Such processes could be inhibited at PbI_2 defects due to the energetic and/or morphological height barrier with the surrounding perovskite grains.

Chapter 6

Effects of Passivation on Defect Distribution in Perovskite Thin Films

6.1. Abstract

The presence of defects substantially hinders the optoelectronic performance of perovskite solar cells. To reduce defect densities and improve performance of hybrid perovskites, various strategies have been designed and implemented [124, 126, 127, 354, 355]. In this Chapter, we will discuss how some these passivation strategies that are known to reduce defect densities, impact nanoscale defects in perovskite thin films. We will utilize photoemission electron spectro-microscopy and time-resolved photoemission electron microscopy to monitor the distribution of nanoscale defects and their charge trapping dynamics after treatments that are known to reduce defect densities.

6.2. Passivation by post-treatment

One of the common passivation strategies to reduce defect densities in hybrid perovskites, is passivation by post-treatment [356-358]. This approach typically involves introduction of functional molecules, Lewis acids or halogen ions on the surface of an already fabricated perovskite film [359-361]. Additionally, introduction of simple molecules, such as oxygen, has also been reported to enhance optoelectronic quality of perovskites [208, 362-365]. In particular, remarkable enhancements in photoluminescence intensity have been observed and related to reduction in trap densities upon illuminating perovskite films and microcrystals with visible light in the presence of oxygen [208, 366-369]. Given that oxygen has been reported to intercalate to perovskite via defects [370], in this work, by employing TR-PEEM to probe nanoscale defects in hybrid perovskite thin films, we were seeking to visualize the response of each defect type to illumination in oxygen environment.

6.2.1. Light and environment effects

To understand the very beginning response of defects under photo-exposure in the presence of oxygen, we have first performed PEEM measurements on perovskite sample, including mapping of defects, photoelectron spectroscopy and TR-PEEM (Figure 6.1). Following PEEM measurements, sample was exposed to light and controlled amounts of dry air inside of a small external chamber with fused silica window. The transfer suitcase containing perovskite sample mounted on a PEEM cartridge was attached to the chamber. The chamber was pumped and purged several times and filled with dry air to reach 1 mbar dry air pressure, which has been reported to be sufficient to begin observing improvements in photoluminescence [365]. The sample was introduced to the external chamber and exposed to He-Ne laser light (less than 1 sun intensity) through the window for the duration of 1 hour. The laser beam was prior expanded to illuminate the whole area of perovskite film under the cartridge cap. After the treatment, PEEM measurements were repeated on the same areas. Having fiducial gold markers deposited on the sample, was very helpful for this experiment and allowed to easily locate the regions of interest.

The exposure measurements could not have been conducted in situ in the imaging chamber of PEEM, because the oxygen pressures required for passivation, were higher than the PEEM system can tolerate. PEEM can only operate under ultrahigh vacuum conditions (at least 10^{-7} Torr) that are required to reduce probability of electrical discharge on sample and to prevent scattering of photo-emitted electrons with gas molecules. Moreover, the microchannel plate that amplifies the detected electrons can be damaged if vacuum in the column of the microscope is poor.

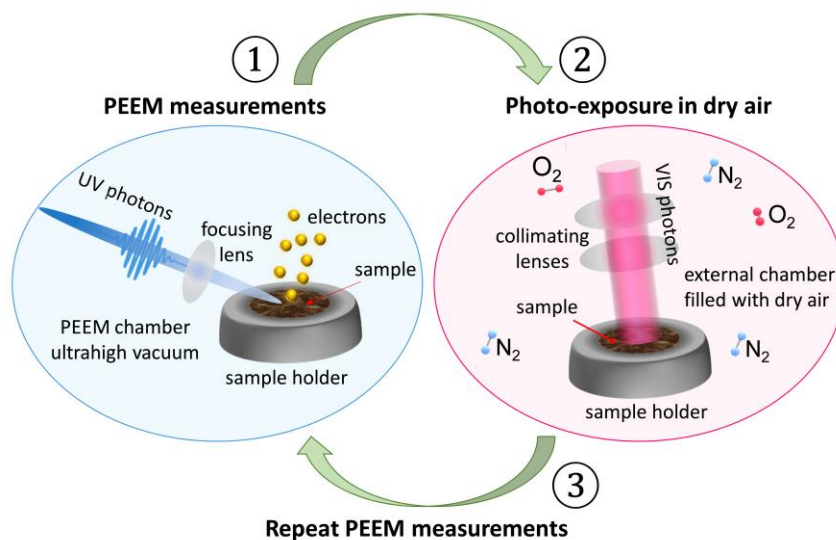


Figure 6.1. Schematic of photo-exposure measurements. Step (1) covers PEEM measurements including PEEM imaging of defects, PES and TR-PEEM; at step (2), photo-exposure is conducted in an external chamber filled with dry air; at step (3), PEEM measurements are repeated again after the treatment.

We specifically tracked responses of different types of defects after the treatment, and found that grain boundary defects that prior to the treatment, demonstrated pronounced hole trapping signal, no longer acted as traps. TR-PEEM images in Figure 6.2a and TR-PEEM decay dynamics in Figure 6.2b, clearly show this deactivation of charge trapping at grain boundary defects, as seen from lack of changes in PEEM intensity after the photo-excitation. Given that in Chapter 5, we have identified grain boundary defects as one of the most detrimental channels of non-radiative recombination, this deactivation of trapping after treatment could nicely contribute to explanations of the reported enhancements of photoluminescence intensity after illumination of perovskite films in the presence of oxygen.

This observation was also interesting in context of theoretical reports that discussed effects of defect-mediated oxygen absorption in perovskites. The density functional theory modelling by Meggiolaro *et al.* [21], proposed a mechanism of inactivation of deep hole traps associated with iodide interstitials upon interactions with oxygen. The report suggested that oxidation of interstitial iodine was favored over the lattice iodine and effectively deactivated deep hole traps introduced by iodine interstitials by forming moderately stable oxidized products. From our TR-PEEM measurements, we observed that hole-trapping grain boundary defects cured readily after exposure to dry air, while pristine film did not demonstrate obvious changes. Our measurements do not provide access to structural information, and therefore, we cannot promptly attribute grain boundary defects to interstitial iodide. Nevertheless, our direct experimental visualization of the removal of an important channel of non-radiative recombination upon treatment with oxygen, remains in good agreement with proposed theoretical model.

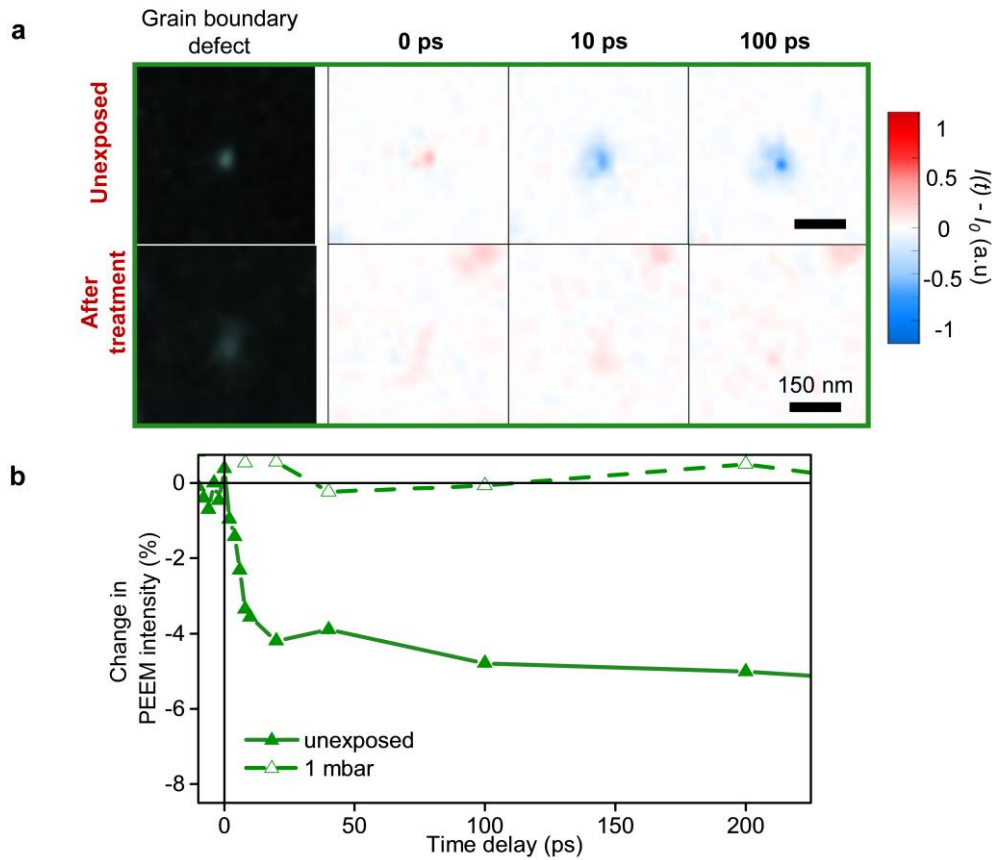


Figure 6.2. TR-PEEM response of grain boundary defects to photo-exposure in dry air. (a) PEEM and TR-PEEM images of selected grain boundary defect before exposure (“Unexposed”) and after treatment with 1 mbar dry air (“After treatment”) upon illumination. (b) TR-PEEM dynamics before and after treatment for grain boundary defects plotted as percent change in PEEM intensity $[I(t) - I_0]/I_0 \times 100$.

After we established response of the grain boundary defects, we turned into investigating response of the intra-grain defects. Surprisingly, these defects were largely unchanged after the treatment with 1 mbar dry air, as seen from comparison of PEEM images (Figure 6.3a, c) and photoelectron spectra (Figure 6.3b, d). The TR-PEEM signals of those, also remained largely unchanged after the treatment (Figure 6.4). The lack of response of the intra-grain defects could be related to slower rates of interaction of oxygen with defects occurring within hexagonal perovskite and PbI_2 phases. It would thus be interesting to monitor the behavior of these defects upon more intense treatments.

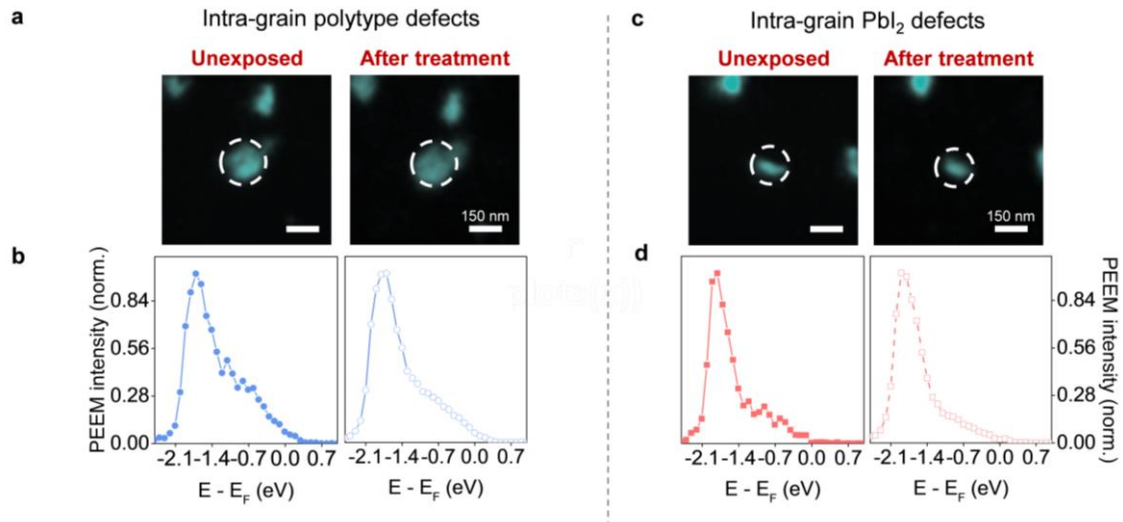


Figure 6.3. Response of intra-grain defects to photo-exposure under 1 mbar dry air. (a) PEEM images of a selected intra-grain polytype defect before (“Unexposed”) and after the treatment (“After treatment”). Images are plotted on the same intensity scale. (b) Photoemission spectra of the defects in (a) showing that density of occupied mid gap states was not obviously affected by the treatment. (c) PEEM images of a selected intra-grain PbI_2 defect before and after the treatment. Images plotted on the same intensity scale. (d) Photoemission spectra of the defects shown in (c). Similar to (b), the density of occupied mid gap states for PbI_2 defects was not affected by the treatment.

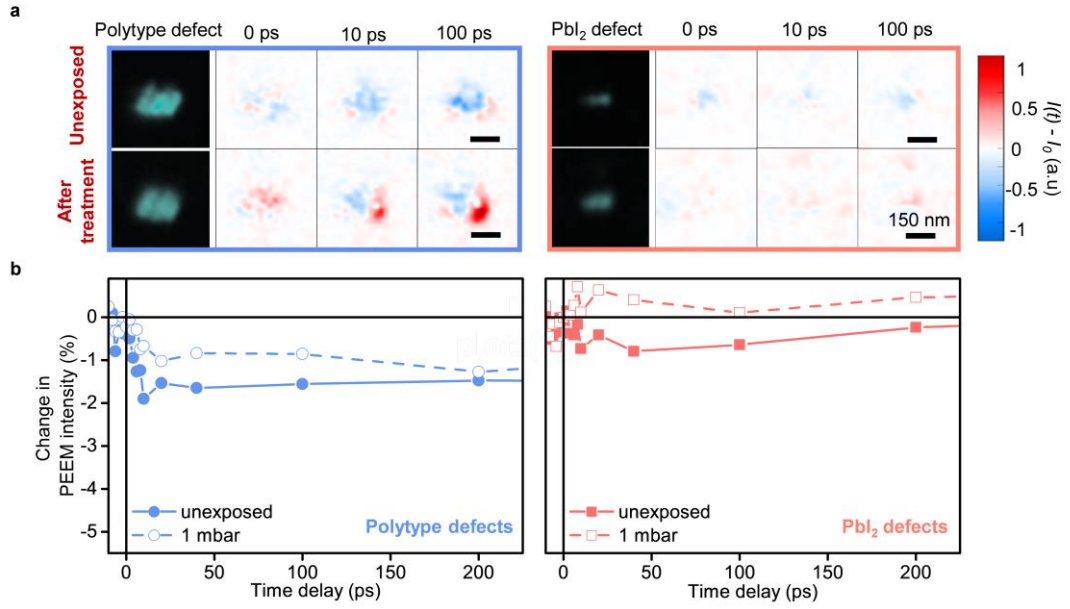


Figure 6.4. TR-PEEM response of intra-grain defects to photo-exposure in dry air. (a) PEEM and TR-PEEM images of selected intra-grain polytype (blue box) and PbI₂ (red box) defects before exposure and after treatment with 1 mbar dry air upon illumination. (b) TR-PEEM dynamics before and after the treatment for intra-grain polytype (blue line) and PbI₂ (red line) defects, plotted as percent change in PEEM intensity $[I(t) - I_0]/I_0 \times 100$.

To understand the response of defects to more intense dry air treatment, we filled the chamber to 10 mbar dry air pressure and repeated photo-exposure with subsequent PEEM measurements. Interestingly, after further exposure, we began detecting reduction in defect densities for the intra-grain defects, while the grain boundary defects remained suppressed. Figure 6.5 shows the response of intra-grain defects during photo-exposure upon increasing dry air pressure. The defect densities of intra-grain defects, reduced after the treatment with 10 mbar dry air, as seen from PEEM images in Figure 6.5a and photoelectron spectra in Figure 6.5b. From photoelectron spectroscopy, we can more clearly observe reduced photoemission intensity in mid gap region after the treatment, which indicated suppression of defect densities. For better visualization, we highlighted the “defect shoulder” in photoelectron spectra in Figure 6.5b with blue boxes.

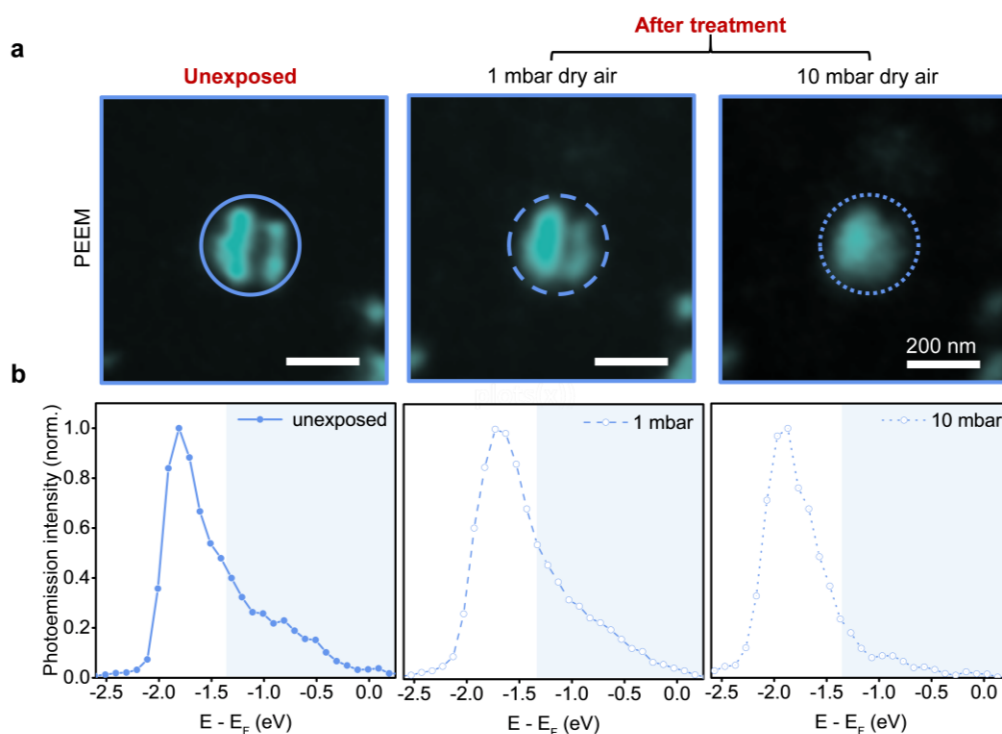


Figure 6.5. Response of intra-grain polytype defects to photo-exposure with different dry air conditions. (a) PEEM images of a selected defect before exposure and after treatments, shown on the same intensity scale. (b) Photoelectron spectra plotted for the defects shown in (a), with contribution from mid gap states highlighted with blue shaded boxes.

The response of PbI_2 defects, showed similar trends to the intra-grain polytype defects. After mild dry air treatment, we did not observe obvious changes in their photoemission intensities. However, with more intense exposure to dry air, we also began detecting reduction in photoemission intensity of this defect type as seen from PEEM images and photoelectron spectra in Figure 6.6. This observation was very interesting, and allowed to suppose that reaction of intra-grain polytype and PbI_2 defects with oxygen could be occurring via similar mechanisms.

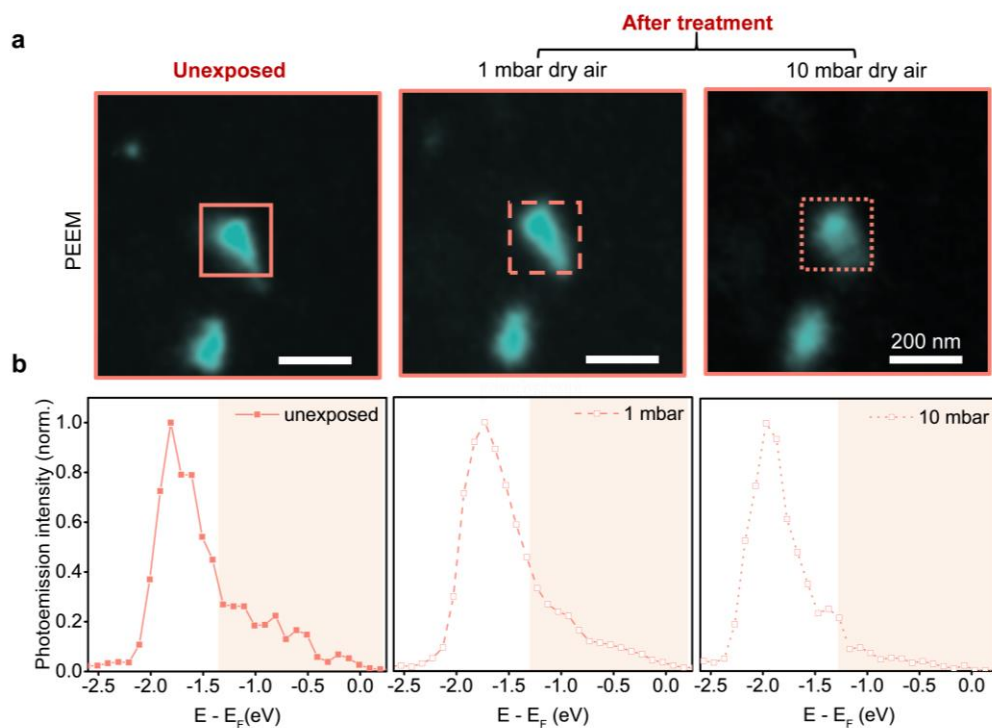


Figure 6.6. Response of PbI_2 defects to photo-exposure with different dry air conditions. (a) PEEM images of a selected defect before exposure and after treatments, shown on the same intensity scale. (b) Photoelectron spectra plotted for the defects shown in (a), with contribution from mid gap states highlighted with red shaded boxes.

We also began observing electrostatic changes associated with defect sites after the treatment. By comparing the plots of photoelectron spectra of intra-grain defects *versus* pristine grains before and after the treatment, we found an extra shift in work function for these defects after the treatment (Figure 6.7). Such electrostatic shifts sustained even after further treatment with more intense dry air conditions. This could imply chemical changes at defect sites after interaction with oxygen. For example, formation of oxidized phases has been reported in literature to take place when superoxide that is formed between molecular O_2 and an excess electron, reacts with perovskite surface forming by Pb-O covalent bond with surface Pb ion [125]. This further disintegrates the Pb-I octahedral structure. Such processes could be occurring even faster at defect sites, considering lack of order at the surface due to high defect density. Therefore, any changes in work function that we have observed even with mild treatments, could be an early indication of competitive processes of reduction of defect density, and formation of new oxidized phases.

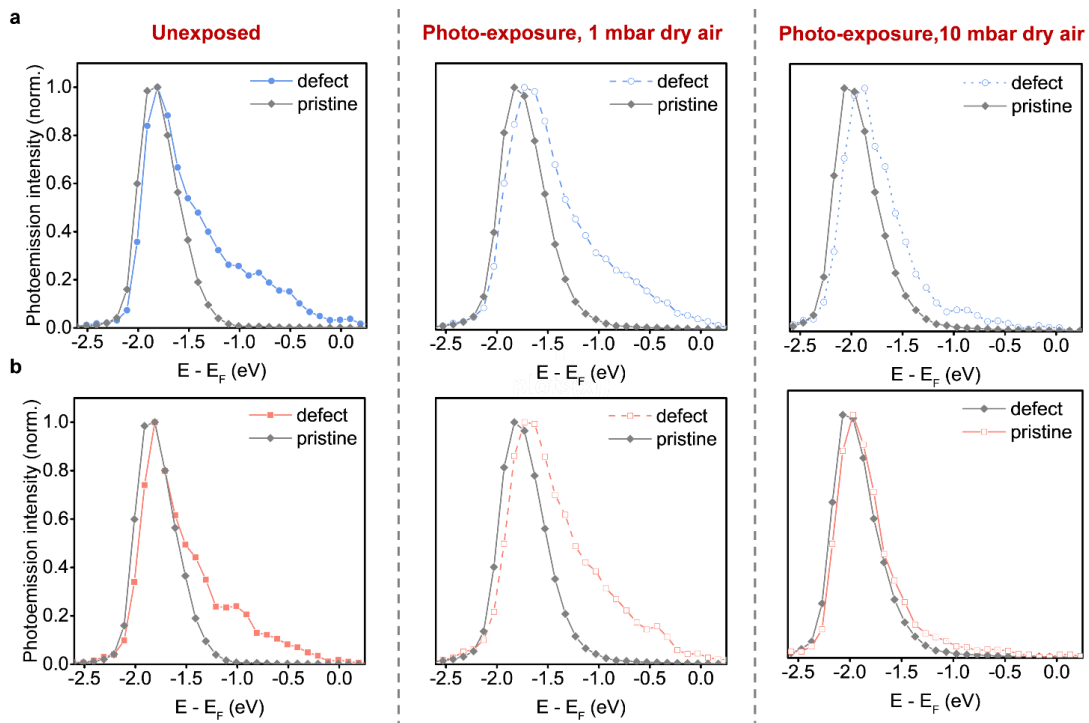


Figure 6.7. Evolution of photoelectron spectra of intra-grain defects and pristine areas before and after the treatment. (a) Photoelectron spectra of selected intra-grain polytype defect (blue line) and pristine grains (grey) before the treatment (“Unexposed”) and after photo-exposure with 1 mbar and 10 mbar dry air upon illumination, as labelled. By tracking cutoff energy, larger energy shift is observed between defect site and pristine grains after the treatment. (b) Evolution of photoelectron spectra of PbI_2 defects, showing similar increased energy shift between defect site and pristine grains after the treatment.

Another interesting aspect is that reduction of trap densities upon exposure to light and oxygen, can be reversible. It has been reported that over time upon keeping perovskite samples in vacuum, the improved photoluminescence intensity observed after treatment, can revoke back [367]. To understand if we would observe such effects through our measurements, we kept the sample in vacuum chamber of PEEM for one day after the treatment, and repeated the PEEM measurements. We found that some of the intra-grain defects showed signs of recovery. Figure 6.8 shows variation of PEEM intensity at defect sites as a function of treatment. Some of the intra-grain defects that were prior suppressed by photo-exposure in dry air, showed preferential brightening after resting in vacuum chamber of PEEM. We conclude that the defect density can revoke back over time due to the desorption of oxygen.

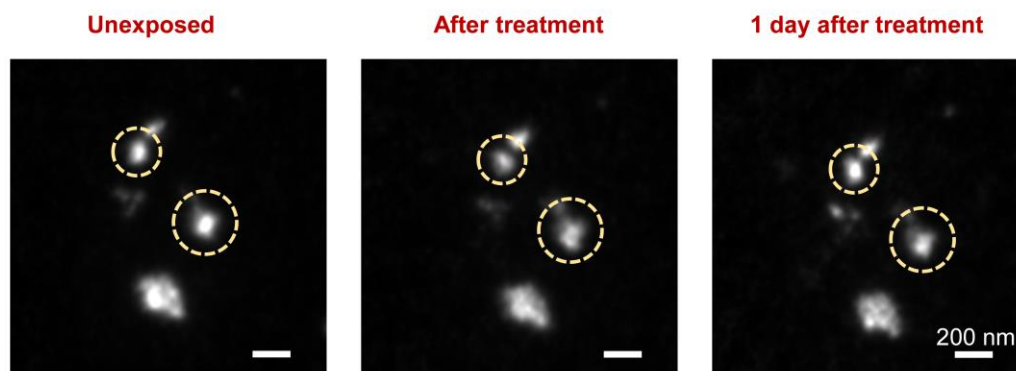


Figure 6.8. Evolution of defects after treatment. PEEM images of intra-grain defects before treatment (“Unexposed”), after photo-exposure in dry air (“After treatment”) and one day after the treatment (“1 day after treatment”). PEEM images were taken with same exposure conditions and are shown of the same intensity scale.

It is worth discussing here that exposure to oxygen has been reported to not only enhance performance of perovskites, but could also contribute to beginning of degradation processes. In fact, prolonged exposure has been reported to result into film degradation caused by reaction of superoxide species with perovskite that overcomes the healing effect of defect annihilation and eventually destroys perovskite [343, 368, 371]. In order to observe such degradation effects, treatments lasting for multiple hours are required. During our measurements, we have not conducted such intense exposure experiments. Therefore, it remains an interesting and open question to understand how defects would react to such prolonged and intense exposure to oxygen.

In this work, we focused our efforts extensively on studying mixed halide perovskite samples. Given that mixed halide perovskites are prone to phase segregation upon illumination, it is worth discussing these effects here. According to literature reports, phase segregation upon illumination of mixed halide perovskites, was suggested to proceed via formation of I-rich phase which dominates photoluminescence [372, 373]. In this thesis, we used triple cation mixed halide perovskite composition containing MA, FA and Cs cations with relatively low Br content. Such films have been reported to be more photo-stable compared to single cation, or Br-rich films [181, 374]. Therefore, we did not expect to observe the effects of phase segregation in our measurements. However, it would be relatively straightforward to observe phase segregation effects from photoelectron spectroscopy measurements and even formation of I-rich domains

that were reported for Br-rich perovskite compositions by Bischak *et al.* [181]. Given that I-rich phase has a lower band gap compared to the mixed phase by about 250 - 300 meV, we would be capable of tracking such changes with photoelectron spectroscopy.

6.3. Passivation during perovskite formation

Passivation of perovskite thin film samples via mixing various additives to the precursor solution became a viable strategy to enhance performance of perovskite solar cells. Such additives typically include metal cations such as Na^+ , K^+ , Rb^+ [46, 375, 376], halogen anions such as Cl^- , I^- [377-379] or small molecules such as BQ, *etc.* [380], that are added to the precursor solution before the deposition of perovskite films. The passivated perovskites were reported to have suppressed non-radiative recombination and improved device efficiencies. In this work, given our capabilities to directly visualize defects in perovskite thin films, we aimed to understand how one of such treatments, in particular addition of potassium iodide, would impact the defect distribution.

6.3.1. Passivation with KI additives

Addition of potassium iodide (KI) to perovskite precursor has been reported to improve photoluminescence quantum efficiency of perovskite thin films and to enhance efficiency of perovskite solar cells [46]. Such improvements have been explained *via* passivation of defects with excess iodide and formation of potassium-rich species at grain boundaries and at the film surface. In order to test how addition of potassium impacts distribution of defects, we performed PEEM measurements on passivated triple cation mixed halide samples with 10 % potassium incorporation [46]. The passivated samples have been prepared by our colleagues from Stranks Lab at the University of Cambridge by depositing perovskite precursor solution with incorporated potassium iodide on ITO/glass substrates. The samples were shipped to Okinawa Institute of Science and Technology in well-sealed packaging to avoid exposure to ambient air.

Through PEEM imaging (Figure 6.9a), we found differences in defect size and distribution in K-passivated samples as compared to un-passivated perovskite [381]. By comparing the size distribution of defects in K-passivated samples (Figure 6.9b) with un-passivated (discussed in Figure 3.5 in Chapter 3), we observed that the very small defects that we found in un-passivated films, were largely not present in passivated samples. The average size of defects in passivated samples was estimated to be on the order of 200 nm and most of the defects were larger than 100 nm. For better visualization, we are showing PEEM images of defects in both K-passivated and un-passivated films in Figure 6.9c and d. From this comparison, it is evident that very small defects that are present in un-passivated films, were not observed in K-passivated perovskite.

We further correlated distribution of defects in K-passivated samples with surface morphology of the film imaged with scanning electron microscopy (Figure 6.10a and b). Through this correlation, we identified that defects in K-passivated samples were associated with morphological grains, as marked with red dashed circles in Figure 6.10a and b. In these measurements, we did not observe any of the defects to be situated at grain boundaries. In Figure 6.10c, for better visualization, we show magnified PEEM and SEM images of a selected defect (marked with blue boxes in Figure 6.10a and b). Our preliminary measurements thus showed that in contrast to un-passivated samples that contained both grain boundary and intra-grain defects, the defects in K-passivated samples had predominantly intra-grain nature.

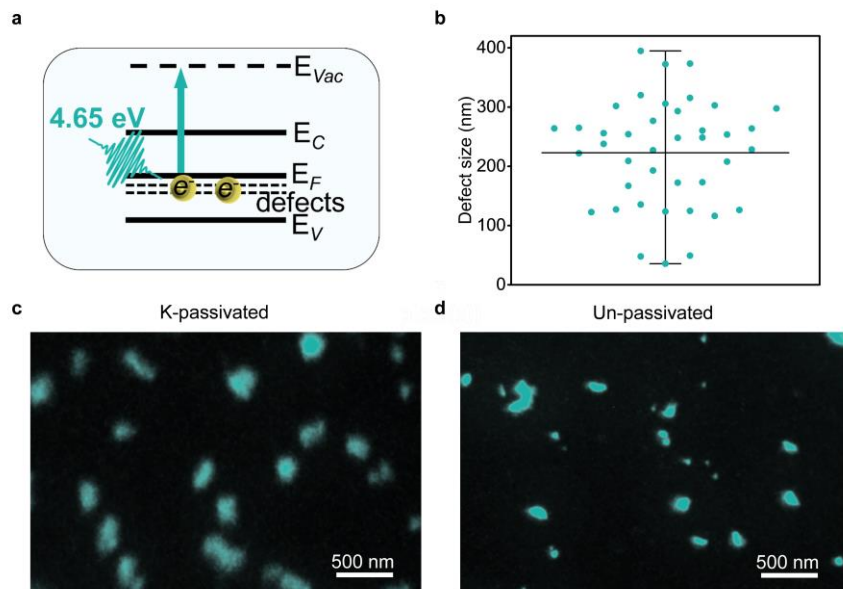


Figure 6.9. Distribution of defects in K-passivated perovskite thin films. (a) Energy-level diagram of perovskite sample when using 4.65 eV probe photons. (b) Estimated defect sizes (analyzed within 5 μm field of view). (c) PEEM image of surface defects in K-passivated perovskite thin film. (d) PEEM image of defects in un-passivated sample.

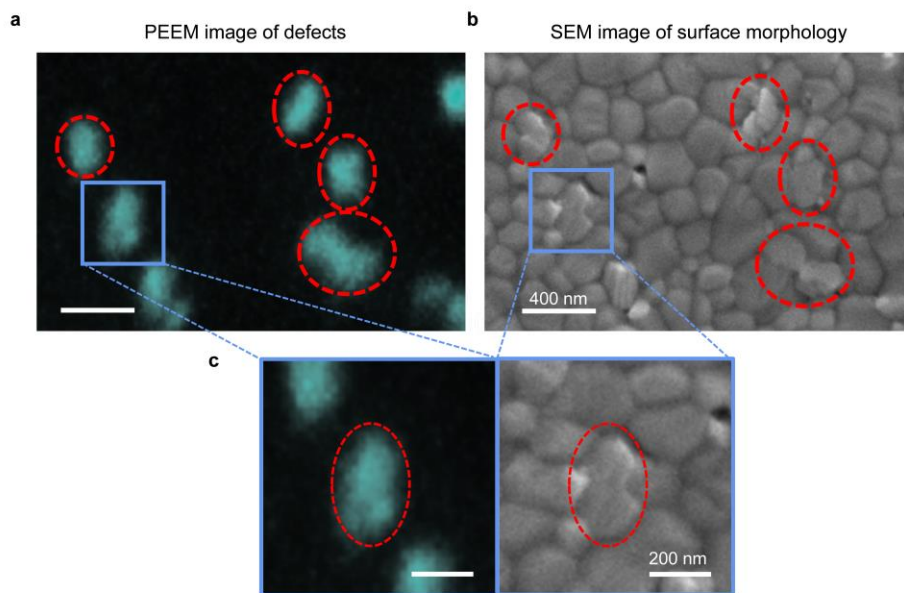


Figure 6.10. Correlation of defects in K-passivated samples with surface morphology. (a) PEEM image of defect in K-passivated samples acquired with 4.65 eV photons. (b) SEM images of the same area as (a). Red dashed circles are indicating defects in (a) that are associated with morphological grains in (b). (c) Magnified PEEM and SEM images from the areas marked with blue boxes in (a) and (b), showing intra-grain nature of defects in K-passivated perovskite films.

Through photoelectron spectroscopy measurements, as shown in Figure 6.11(a, b), we found that defect sites in K-passivated samples were associated with high density of occupied mid gap states, similarly to intra-grain polytype defects in un-passivated samples. By comparing photoelectron spectra for defect sites and pristine areas, we observed similar work function shifts up to 100 meV associated with defect locations (Figure 6.11a, c), as were observed for intra-grain defects in un-passivated samples (Chapter 4).

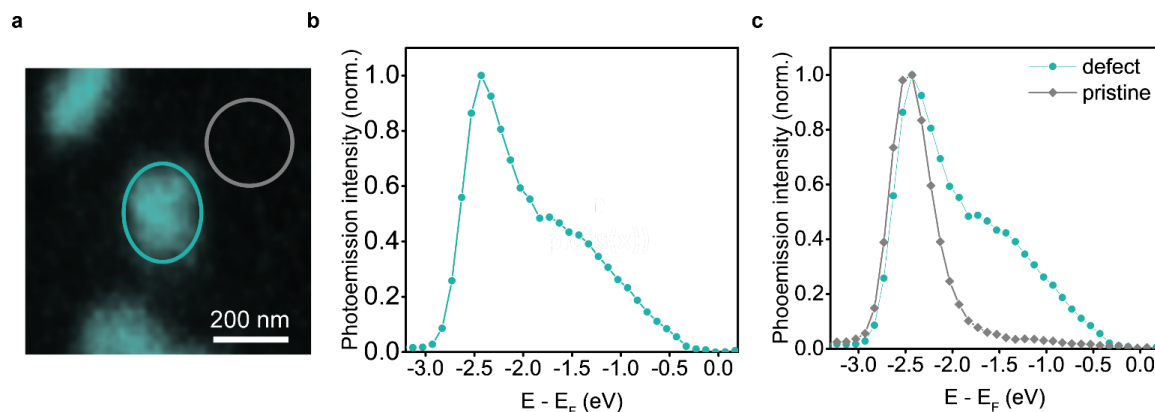


Figure 6.11. Photoelectron spectroscopy of K-passivated perovskite thin film. (a) PEEM image of selected intra-grain defect. (b) Photoelectron spectrum of intra-grain defect highlighted with green circle in (a). (c) Photoelectron spectra of intra-grain defect highlighted with green circle in (a) and pristine area highlighted with grey circle in (a), showing energy shift towards higher work function values for the defect site.

When employing TR-PEEM, upon photo-exciting passivated sample with near infrared pump photons, we found that defects in K-passivated samples participated in sub-nanosecond hole trapping, as seen from TR-PEEM dynamics in Figure 6.12. Moreover, their trapping dynamics followed those of intra-grain polytype defects in un-passivated samples (Section 5.2.2).

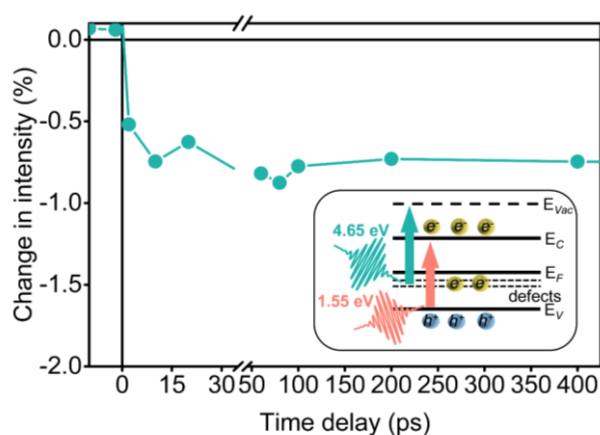


Figure 6.12. TR-PEEM signal of intra-grain defects in K-passivated perovskite thin film. 1.55 eV photons with fluence of about $100 \mu\text{J cm}^{-2}$ were used for photoexcitation. TR-PEEM response was recorded for intra-grain defects and averaged for multiple defects.

Our preliminary observations imply that passivation of perovskites with potassium seems to successfully passivate grain boundary defects. This is in agreement with report by Abdi-Jalebi *et al.* [46], who found formation of K-rich species at grain boundaries after addition of KI and reported them to effectively suppress non-radiative recombination arising from interstitial halides. However, according to our observations, K-passivation might not be sufficient to eliminate formation of intra-grain surface defects in mixed halide perovskites. Formation of such defects might require careful control of fabrication conditions during film deposition [77] and does not seem to be impacted by addition of metal cations.

6.4. Conclusion

In this Chapter, we aimed to understand the behavior of nanoscale defects in hybrid perovskite thin films upon applying treatments known to suppress defect densities and to improve photoluminescence intensity of perovskites. We chose a common post-treatment strategy when perovskite thin film was exposed to dry air upon light illumination. We found that mild amounts of dry air appeared to be sufficient to suppress trapping by the grain boundary defects, while intra-grain defects remained largely unchanged and required more intense treatments to begin showing reduced densities. We also employed passivation during the film formation via addition of potassium iodide to the precursor solution before the film deposition. We found that small grain boundary defects were suppressed in passivated samples, while intra-grain defects remained present. We conclude that defect engineering in hybrid perovskites is a complex problem, and might require application of multiple targeted strategies, instead of designing one universal approach. We would also like to emphasize on the suitability of PEEM and TR-PEEM to act as very powerful tools to characterize performance losses in perovskite thin film samples.

Chapter 7

Conclusion and Outlook

7.1. Conclusion

In this thesis, we aimed to shed more light on the defect structure of perovskite thin films. In Chapters 1 and 2, we provided detailed introduction to our research and explained methodologies used in this thesis. In Chapter 3, we employed photoemission electron microscopy to image occupied mid gap defect states in perovskite thin films. These defects appeared as nanoscale clusters of few tens to few hundreds of nanometers in sizes. By correlating the locations of the nanoscale defects with surface microstructure of perovskite thin films, we found that the smallest defects of just few tens of nanometers in sizes, formed predominantly at grain boundaries, while larger ones, of few hundreds of nanometers in sizes, were associated with entire grains. By further correlating our PEEM results with auxiliary microscopy techniques, we found that some of the intra-grain defects were associated with precipitated PbI_2 , while the rest of them formed within regular morphological grains.

In Chapter 4, we employed photoelectron spectroscopy to access spectroscopic information about the defects as compared to pristine perovskite film. We found that some of the intra-grain defects were associated with local elevations in work function, suggesting that they might be originating from different material phase. The photoelectron spectra of these defects were also found to show higher defect density in mid gap region, as compared to PbI_2 defects.

In Chapter 5, by employing time-resolved photoemission electron microscopy, we turned into investigating particular role of each defect type in performance of perovskite thin films. TR-PEEM combines spatial resolution of PEEM and temporal resolution of optical pump-probe experiment and allows to monitor spatio-temporal charge carrier trapping dynamics at defect sites in hybrid perovskites. Via TR-PEEM measurements, we found that depending on their types, the nanoscale defects showed varied roles in charge trapping – from highly detrimental to relatively benign. In particular, grain boundary defects and one type of intra-grain defects that were found to be associated with hexagonal polytype phases, exhibited clear hole-trapping behavior, while defects associated with PbI_2 remained largely benign when photo-exciting perovskite.

Finally, Chapter 6 is devoted to studying response of defects to strategies known to suppress defect densities. We focused on a common post-treatment approach when perovskite film was exposed to controlled amounts of dry air under illumination. We found that even very small amounts of dry air under illumination, were sufficient to suppress trapping by the grain boundary defects and remove an important channel of non-radiative recombination. We also employed another strategy known to suppress defects, such as passivation during film growth via addition of potassium iodide to the precursor solution. We found that addition of potassium can suppress

formation of the small grain boundary defects, while still leaving the intra-grain defects present. We showed that PEEM and TR-PEEM can serve as excellent tools to directly monitor the evolution of surface defects while applying different treatments.

Our work on uncovering the presence of multiple types of nanoscale defects in perovskite thin films, their varied roles in film performance and varied response to passivation strategies brings important understanding about microscopic behavior of hybrid perovskites and we hope will help develop successful strategies to engineer the defects. This thesis work is one of the pioneering works applying PEEM and TR-PEEM to study hybrid perovskites [47, 132, 279, 284, 307, 382] and we truly hope to inspire future researches applying such complex yet very rewarding techniques to keep exploring variety of perovskite- and other photovoltaic materials.

7.2. Outlook

In this thesis, we showed that the nanoscale defects of just few tens of nanometers in sizes, formed at specific grain boundaries. However, given the very small sizes of these defects, it was challenging to extract any un-ubiquitous information about their nature. We therefore, concluded that employing techniques with atomic scale resolution, would be a useful follow up to our study and will allow to further understand structural or chemical information about these defects. In particular, structural information could be obtained via application of transmission electron microscopies (high resolution TEM, high-angle annular dark field scanning TEM, etc.) that have recently demonstrated outstanding results when employed to study hybrid perovskites. For example, *via* TEM measurements, the presence of amorphous phases at grain boundaries in FA-perovskites has been revealed [269]. Other works highlighted formation of intra-grain defects assigned to stacking faults that were also harboring point defects [287]. This makes it interesting to also correlate intra-grain defects observed by us in PEEM with TEM measurements to find out which exact types of perovskite defects (planar or clusters of point defects we have found through our PEEM measurements). When addressing chemical information, correlation of PEEM with energy-dispersive x-ray spectroscopy, cathodoluminescence microscopy [181], IR nano-spectroscopy [251], scanning tunneling microscopy and spectroscopy [98], would be of great interest, as their high level of spatial resolution and ability to obtain chemical information, would complement nicely our PEEM identification of defects.

When employing time-resolved PEEM, we have demonstrated that some of the nanoscale defects in hybrid perovskite thin films participated in trapping of photo-excited holes. However, we did not observe the photoemission signal at defect sites to recover within the sub-nanosecond measurement window of our TR-PEEM experiment, which is in agreement with reported long lifetimes of trapped holes [22]. This implies that longer time window might be required to understand the trapping dynamics fully. Such TR-PEEM experiment will require more technical steps, such as adopting the experimental set-up to operate at the longer time delays (of about a few hundreds of nanoseconds [14]) via, for example, the use of electro-optic modulators to generate longer time delays between pump and probe. Here, however, the signal-to-noise and measurement time will require careful attention, as each image frame will require long exposure and many averages to collect good quality signal. On a side note, throughout our measurements, we only observed holes being trapped at the defect sites in perovskites and we did not detect any signs of electron trapping. Electron traps are another detrimental pathway of non-radiative recombination in perovskites and would appear in TR-PEEM measurements as an increase in photo-emission intensity in mid gap spectral region after the photo-excitation. However, we did not detect any of such signals so far. We were also not able to image the photo-excited state, which given the crystal symmetry of perovskite, could require higher energies of probe photons to photo-emit from the lowest conduction band and highest valence band edges. This implies that further work is required to develop and employ pulsed sources of higher photon energies to keep exploring photo-excited phenomena in hybrid perovskites.

In this work, we extensively studied the state-of-the-art triple cation mixed halide hybrid perovskite composition. Besides this, perovskite family has many other compositional variations to offer, that are as well applied to manufacture highly efficient solar cells and light emitting diodes. Given that PEEM provides a direct visual of the defect-mediated processes occurring in thin film perovskites, it would be very useful to keep investigating many other

compositional variations of perovskites and establish composition-property relationship in terms of distribution of surface defects from PEEM measurements.

Recently wide-band-gap perovskites for tandem application have been attracting more and more attention [123, 383]. These Br-rich compositions are known to be prone to phase segregation, the origin of which is still not well understood. At the same time various strategies are being offered to suppress phase segregation via *e.g.*, incorporation of additives such as Cl, two dimensional materials, bulky metal cations (NMA) or interface passivation via post-treatments [44, 384, 385]. Given the great applicability of PEEM to directly probe how passivation strategies impact distribution of surface defects, it becomes a straightforward future direction to explore.

Furthermore, the upscaling of devices is one of the most important requirements for commercialization of perovskite solar cells. Therefore, careful investigation and control of films prepared by methods allowing large-scale production of perovskite modules is of high importance. Keeping in mind that thus far spin-coating from solution allows to fabricate devices with highest efficiencies, further understanding of limitations of films prepared by scalable methods, remains critical. Being solution-, vapor-based or hybrid-, film deposition approaches can result in formation of various defects that can be readily identified with TR-PEEM.

Apart from thin film perovskites, in recent years, two-dimensional perovskites [386] have become popular for opto-electronic applications. These materials due to dimensionality effects, possess a plethora of interesting properties. One of those, is excitonic character of photo-excited state, unlike for three-dimensional perovskites where free carriers are formed after photo-excitation due to the low exciton binding energies. It would be interesting to visualize the photo-excited state in 2D perovskites and TR-PEEM here would serve as a convenient tool to achieve this.

Finally, the study of perovskite heterojunctions with other materials such as electron- or hole transport layers deserve attention. Time-resolved spectro-microscopy here would allow to visualize the movement of charges through the layers after the photo-excitation. In this way, in addition to losses in perovskite absorber, the losses at heterojunction can be studied. An important limitation here would be the surface-sensitive nature of PEEM measurements. Therefore, only ultrathin layers of material should be deposited on perovskite in order for the experiment to succeed. Alternatively, investigation of 2D perovskites deposited on a thin transport layer can be considered.

Lastly, although this thesis was focused on hybrid perovskites, same arguments and methodologies can be applied to other photovoltaic materials. The ability of PEEM to resolve nanoscale- and microscale information, coupled with visualization of charge transfer in space, time and energy achieved via TR-PEEM, creates a valuable characterization route to understand and further improve the properties of materials.

References

- [1] A. Kojima, K. Teshima, Y. Shirai, and T. Miyasaka, "Organometal Halide Perovskites as Visible-Light Sensitizers for Photovoltaic Cells" *Journal of the American Chemical Society*, vol. 131, no. 17, pp. 6050-6051, 2009/05/06 2009, doi: 10.1021/ja809598r.
- [2] NREL. "Best Research-Cell Efficiency Chart." <https://www.nrel.gov/pv/cell-efficiency.html> (accessed 2022).
- [3] J. M. Howard, R. Lahoti, and M. S. Leite, "Imaging Metal Halide Perovskites Material and Properties at the Nanoscale" *Advanced Energy Materials*, vol. 10, no. 26, 2019, doi: 10.1002/aenm.201903161.
- [4] E. M. Tennyson, T. A. S. Doherty, and S. D. Stranks, "Heterogeneity at multiple length scales in halide perovskite semiconductors" *Nature Reviews Materials*, vol. 4, no. 9, pp. 573-587, 2019, doi: 10.1038/s41578-019-0125-0.
- [5] W. de Quilettes Dane *et al.*, "Impact of microstructure on local carrier lifetime in perovskite solar cells" *Science*, vol. 348, no. 6235, pp. 683-686, 2015/05/08 2015, doi: 10.1126/science.aaa5333.
- [6] D. W. deQuilettes *et al.*, "Photo-induced halide redistribution in organic-inorganic perovskite films" *Nature Communications*, vol. 7, no. 1, p. 11683, 2016/05/24 2016, doi: 10.1038/ncomms11683.
- [7] D. W. deQuilettes *et al.*, "Tracking Photoexcited Carriers in Hybrid Perovskite Semiconductors: Trap-Dominated Spatial Heterogeneity and Diffusion" *ACS Nano*, vol. 11, no. 11, pp. 11488-11496, 2017/11/28 2017, doi: 10.1021/acsnano.7b06242.
- [8] S. Draguta *et al.*, "Spatially Non-uniform Trap State Densities in Solution-Processed Hybrid Perovskite Thin Films" *J Phys Chem Lett*, vol. 7, no. 4, pp. 715-21, Feb 18 2016, doi: 10.1021/acs.jpcllett.5b02888.
- [9] S. D. Stranks, "Nonradiative Losses in Metal Halide Perovskites" *ACS Energy Letters*, vol. 2, no. 7, pp. 1515-1525, 2017, doi: 10.1021/acseenergylett.7b00239.
- [10] N.-G. Park and H. Segawa, "Research Direction toward Theoretical Efficiency in Perovskite Solar Cells" *ACS Photonics*, vol. 5, no. 8, pp. 2970-2977, 2018, doi: 10.1021/acsp Photonics.8b00124.
- [11] A. Buin *et al.*, "Materials processing routes to trap-free halide perovskites" *Nano Lett*, vol. 14, no. 11, pp. 6281-6, Nov 12 2014, doi: 10.1021/nl502612m.
- [12] O. M. Bakr and O. F. Mohammed, "Perovskite solar cells: Shedding light on film crystallization" *Nat Mater*, vol. 16, no. 6, pp. 601-602, May 25 2017, doi: 10.1038/nmat4908.
- [13] J. M. Ball and A. Petrozza, "Defects in perovskite-halides and their effects in solar cells" *Nature Energy*, vol. 1, no. 11, 2016, doi: 10.1038/nenergy.2016.149.

- [14] M. J. Trimpl *et al.*, "Charge-Carrier Trapping and Radiative Recombination in Metal Halide Perovskite Semiconductors" *Advanced Functional Materials*, vol. 30, no. 42, 2020, doi: 10.1002/adfm.202004312.
- [15] S. G. Motti *et al.*, "Defect Activity in Lead Halide Perovskites" *Advanced Materials*, vol. 31, no. 47, 2019, doi: 10.1002/adma.201901183.
- [16] W.-J. Yin, T. Shi, and Y. Yan, "Unusual defect physics in CH₃NH₃PbI₃ perovskite solar cell absorber" *Applied Physics Letters*, vol. 104, no. 6, 2014, doi: 10.1063/1.4864778.
- [17] A. Baumann, S. Vath, P. Rieder, M. C. Heiber, K. Tvingstedt, and V. Dyakonov, "Identification of Trap States in Perovskite Solar Cells" *J Phys Chem Lett*, vol. 6, no. 12, pp. 2350-4, Jun 18 2015, doi: 10.1021/acs.jpcclett.5b00953.
- [18] H. Jin *et al.*, "It's a trap! On the nature of localised states and charge trapping in lead halide perovskites" *Materials Horizons*, vol. 7, no. 2, pp. 397-410, 2020, doi: 10.1039/c9mh00500e.
- [19] N. Liu and C. Yam, "First-principles study of intrinsic defects in formamidinium lead triiodide perovskite solar cell absorbers" *Phys Chem Chem Phys*, vol. 20, no. 10, pp. 6800-6804, Mar 7 2018, doi: 10.1039/c8cp00280k.
- [20] D. Meggiolaro and F. De Angelis, "First-Principles Modeling of Defects in Lead Halide Perovskites: Best Practices and Open Issues" *ACS Energy Letters*, vol. 3, no. 9, pp. 2206-2222, 2018, doi: 10.1021/acsenerylett.8b01212.
- [21] D. Meggiolaro *et al.*, "Iodine chemistry determines the defect tolerance of lead-halide perovskites" *Energy & Environmental Science*, vol. 11, no. 3, pp. 702-713, 2018, doi: 10.1039/c8ee00124c.
- [22] W. Li, J. Liu, F.-Q. Bai, H.-X. Zhang, and O. V. Prezhdo, "Hole Trapping by Iodine Interstitial Defects Decreases Free Carrier Losses in Perovskite Solar Cells: A Time-Domain Ab Initio Study" *ACS Energy Letters*, vol. 2, no. 6, pp. 1270-1278, 2017, doi: 10.1021/acsenerylett.7b00183.
- [23] C. Hsu *et al.*, "Efficient mini/micro-perovskite light-emitting diodes" *Cell Reports Physical Science*, vol. 2, no. 9, p. 100582, 2021/09/22/ 2021, doi: <https://doi.org/10.1016/j.xcrp.2021.100582>.
- [24] G. Pacchioni, "Highly efficient perovskite LEDs" *Nature Reviews Materials*, vol. 6, no. 2, pp. 108-108, 2021/02/01 2021, doi: 10.1038/s41578-021-00280-5.
- [25] K. Zhang, N. Zhu, M. Zhang, L. Wang, and J. Xing, "Opportunities and challenges in perovskite LED commercialization" *Journal of Materials Chemistry C*, 10.1039/D1TC00232E vol. 9, no. 11, pp. 3795-3799, 2021, doi: 10.1039/D1TC00232E.
- [26] H. Jing *et al.*, "Flexible Ultrathin Single-Crystalline Perovskite Photodetector" *Nano Letters*, vol. 20, no. 10, pp. 7144-7151, 2020/10/14 2020, doi: 10.1021/acs.nanolett.0c02468.
- [27] C. Li *et al.*, "Ultrafast and broadband photodetectors based on a perovskite/organic bulk heterojunction for large-dynamic-range imaging" *Light: Science & Applications*, vol. 9, no. 1, p. 31, 2020/03/03 2020, doi: 10.1038/s41377-020-0264-5.

- [28] L. Li, S. Ye, J. Qu, F. Zhou, J. Song, and G. Shen, "Recent Advances in Perovskite Photodetectors for Image Sensing" *Small*, <https://doi.org/10.1002/sml.202005606> vol. 17, no. 18, p. 2005606, 2021/05/01 2021, doi: <https://doi.org/10.1002/sml.202005606>.
- [29] W. Li *et al.*, "Evaporated Perovskite Thick Junctions for X-Ray Detection" *ACS Applied Materials & Interfaces*, vol. 13, no. 2, pp. 2971-2978, 2021/01/20 2021, doi: 10.1021/acscami.0c20973.
- [30] Z. Li, F. Zhou, H. Yao, Z. Ci, Z. Yang, and Z. Jin, "Halide perovskites for high-performance X-ray detector" *Materials Today*, vol. 48, pp. 155-175, 2021/09/01/ 2021, doi: <https://doi.org/10.1016/j.mattod.2021.01.028>.
- [31] L. Pan, S. Shrestha, N. Taylor, W. Nie, and L. R. Cao, "Determination of X-ray detection limit and applications in perovskite X-ray detectors" *Nature Communications*, vol. 12, no. 1, p. 5258, 2021/09/06 2021, doi: 10.1038/s41467-021-25648-7.
- [32] H. Wu, Y. Ge, G. Niu, and J. Tang, "Metal Halide Perovskites for X-Ray Detection and Imaging" *Matter*, vol. 4, no. 1, pp. 144-163, 2021/01/06/ 2021, doi: <https://doi.org/10.1016/j.matt.2020.11.015>.
- [33] V. M. Goldschmidt, "Die Gesetze der Krystallochemie" *Naturwissenschaften*, vol. 14, no. 21, pp. 477-485, 1926/05/01 1926, doi: 10.1007/BF01507527.
- [34] W. Travis, E. N. K. Glover, H. Bronstein, D. O. Scanlon, and R. G. Palgrave, "On the application of the tolerance factor to inorganic and hybrid halide perovskites: a revised system" *Chemical Science*, 10.1039/C5SC04845A vol. 7, no. 7, pp. 4548-4556, 2016, doi: 10.1039/C5SC04845A.
- [35] C. Li, K. C. K. Soh, and P. Wu, "Formability of ABO₃ perovskites" *Journal of Alloys and Compounds*, vol. 372, no. 1, pp. 40-48, 2004/06/09/ 2004, doi: <https://doi.org/10.1016/j.jallcom.2003.10.017>.
- [36] C. Li, X. Lu, W. Ding, L. Feng, Y. Gao, and Z. Guo, "Formability of ABX₃ (X = F, Cl, Br, I) halide perovskites" *Acta Crystallogr B*, vol. 64, no. Pt 6, pp. 702-7, Dec 2008, doi: 10.1107/s0108768108032734.
- [37] W. Li, Z. Wang, F. Deschler, S. Gao, R. H. Friend, and A. K. Cheetham, "Chemically diverse and multifunctional hybrid organic-inorganic perovskites" *Nature Reviews Materials*, vol. 2, no. 3, 2017, doi: 10.1038/natrevmats.2016.99.
- [38] F. Brivio, K. T. Butler, A. Walsh, and M. van Schilfgaarde, "Relativistic quasiparticle self-consistent electronic structure of hybrid halide perovskite photovoltaic absorbers" *Physical Review B*, vol. 89, no. 15, 2014, doi: 10.1103/PhysRevB.89.155204.
- [39] X. Zhu, H. Su, R. A. Marcus, and M. E. Michel-Beyerle, "Computed and Experimental Absorption Spectra of the Perovskite CH₃NH₃PbI₃" *J Phys Chem Lett*, vol. 5, no. 17, pp. 3061-5, Sep 4 2014, doi: 10.1021/jz501174e.
- [40] F. Zheng, H. Takenaka, F. Wang, N. Z. Koocher, and A. M. Rappe, "First-Principles Calculation of the Bulk Photovoltaic Effect in CH₃NH₃PbI₃ and CH₃NH₃PbI(3-x)Cl(x)" *J Phys Chem Lett*, vol. 6, no. 1, pp. 31-7, Jan 2 2015, doi: 10.1021/jz502109e.
- [41] W. Gao, X. Gao, T. A. Abtey, Y.-Y. Sun, S. Zhang, and P. Zhang, "Quasiparticle band gap of organic-inorganic hybrid perovskites: Crystal structure, spin-orbit coupling, and

- self-energy effects" *Physical Review B*, vol. 93, no. 8, 2016, doi: 10.1103/PhysRevB.93.085202.
- [42] S. Tao *et al.*, "Absolute energy level positions in tin- and lead-based halide perovskites" *Nat Commun*, vol. 10, no. 1, p. 2560, Jun 12 2019, doi: 10.1038/s41467-019-10468-7.
- [43] S. A. Kulkarni, T. Baikie, P. P. Boix, N. Yantara, N. Mathews, and S. Mhaisalkar, "Band-gap tuning of lead halide perovskites using a sequential deposition process" *J. Mater. Chem. A*, vol. 2, no. 24, pp. 9221-9225, 2014, doi: 10.1039/c4ta00435c.
- [44] J. Tong, Q. Jiang, F. Zhang, S. B. Kang, D. H. Kim, and K. Zhu, "Wide-Bandgap Metal Halide Perovskites for Tandem Solar Cells" *ACS Energy Letters*, vol. 6, no. 1, pp. 232-248, 2020, doi: 10.1021/acsenenergylett.0c02105.
- [45] P. McMeekin David *et al.*, "A mixed-cation lead mixed-halide perovskite absorber for tandem solar cells" *Science*, vol. 351, no. 6269, pp. 151-155, 2016/01/08 2016, doi: 10.1126/science.aad5845.
- [46] M. Abdi-Jalebi *et al.*, "Maximizing and stabilizing luminescence from halide perovskites with potassium passivation" *Nature*, vol. 555, no. 7697, pp. 497-501, 2018/03/01 2018, doi: 10.1038/nature25989.
- [47] T. A. S. Doherty *et al.*, "Performance-limiting nanoscale trap clusters at grain junctions in halide perovskites" *Nature*, vol. 580, no. 7803, pp. 360-366, 2020/04/01 2020, doi: 10.1038/s41586-020-2184-1.
- [48] Y. Ogomi *et al.*, "CH₃NH₃S_nxPb(1-x)I₃ Perovskite Solar Cells Covering up to 1060 nm" *The Journal of Physical Chemistry Letters*, vol. 5, no. 6, pp. 1004-1011, 2014/03/20 2014, doi: 10.1021/jz5002117.
- [49] S. De Wolf *et al.*, "Organometallic Halide Perovskites: Sharp Optical Absorption Edge and Its Relation to Photovoltaic Performance" *J Phys Chem Lett*, vol. 5, no. 6, pp. 1035-9, Mar 20 2014, doi: 10.1021/jz500279b.
- [50] H. C. Casey, D. D. Sell, and K. W. Wecht, "Concentration dependence of the absorption coefficient for n- and p-type GaAs between 1.3 and 1.6 eV" *Journal of Applied Physics*, vol. 46, no. 1, pp. 250-257, 1975, doi: 10.1063/1.321330.
- [51] M. D. Sturge, "Optical Absorption of Gallium Arsenide between 0.6 and 2.75 eV" *Physical Review*, vol. 127, no. 3, pp. 768-773, 1962, doi: 10.1103/PhysRev.127.768.
- [52] M. Cardona, "Electron Effective Masses of InAs and GaAs as a Function of Temperature and Doping" *Physical Review*, vol. 121, no. 3, pp. 752-758, 1961, doi: 10.1103/PhysRev.121.752.
- [53] H. D. Barber, "Effective mass and intrinsic concentration in silicon" *Solid-State Electronics*, vol. 10, no. 11, pp. 1039-1051, 1967/11/01/ 1967, doi: [https://doi.org/10.1016/0038-1101\(67\)90122-0](https://doi.org/10.1016/0038-1101(67)90122-0).
- [54] T. M. Brenner, D. A. Egger, L. Kronik, G. Hodes, and D. Cahen, "Hybrid organic—inorganic perovskites: low-cost semiconductors with intriguing charge-transport properties" *Nature Reviews Materials*, vol. 1, no. 1, 2016, doi: 10.1038/natrevmats.2015.7.

- [55] H. Oga, A. Saeki, Y. Ogomi, S. Hayase, and S. Seki, "Improved Understanding of the Electronic and Energetic Landscapes of Perovskite Solar Cells: High Local Charge Carrier Mobility, Reduced Recombination, and Extremely Shallow Traps" *Journal of the American Chemical Society*, vol. 136, no. 39, pp. 13818-13825, 2014/10/01 2014, doi: 10.1021/ja506936f.
- [56] T. J. Savenije *et al.*, "Thermally Activated Exciton Dissociation and Recombination Control the Carrier Dynamics in Organometal Halide Perovskite" *The Journal of Physical Chemistry Letters*, vol. 5, no. 13, pp. 2189-2194, 2014/07/03 2014, doi: 10.1021/jz500858a.
- [57] T. M. Brenner, D. A. Egger, A. M. Rappe, L. Kronik, G. Hodes, and D. Cahen, "Are Mobilities in Hybrid Organic–Inorganic Halide Perovskites Actually “High”?" *The Journal of Physical Chemistry Letters*, vol. 6, no. 23, pp. 4754-4757, 2015/12/03 2015, doi: 10.1021/acs.jpcllett.5b02390.
- [58] D. Stranks Samuel *et al.*, "Electron-Hole Diffusion Lengths Exceeding 1 Micrometer in an Organometal Trihalide Perovskite Absorber" *Science*, vol. 342, no. 6156, pp. 341-344, 2013/10/18 2013, doi: 10.1126/science.1243982.
- [59] G. Xing *et al.*, "Long-Range Balanced Electron- and Hole-Transport Lengths in Organic-Inorganic CH₃NH₃PbI₃" *Science*, vol. 342, no. 6156, pp. 344-347, 2013/10/18 2013, doi: 10.1126/science.1243167.
- [60] Q. Dong *et al.*, "Electron-hole diffusion lengths > 175 μm in solution-grown CH₃NH₃PbI₃ single crystals" *Science*, vol. 347, no. 6225, pp. 967-970, 2015/02/27 2015, doi: 10.1126/science.aaa5760.
- [61] D. Shi *et al.*, "Low trap-state density and long carrier diffusion in organolead trihalide perovskite single crystals" *Science*, vol. 347, no. 6221, pp. 519-522, 2015/01/30 2015, doi: 10.1126/science.aaa2725.
- [62] M. I. Saidaminov *et al.*, "High-quality bulk hybrid perovskite single crystals within minutes by inverse temperature crystallization" *Nature Communications*, vol. 6, no. 1, p. 7586, 2015/07/06 2015, doi: 10.1038/ncomms8586.
- [63] Z. Guo, J. S. Manser, Y. Wan, P. V. Kamat, and L. Huang, "Spatial and temporal imaging of long-range charge transport in perovskite thin films by ultrafast microscopy" *Nature Communications*, vol. 6, no. 1, p. 7471, 2015/06/23 2015, doi: 10.1038/ncomms8471.
- [64] M. Zhang, H. Yu, M. Lyu, Q. Wang, J.-H. Yun, and L. Wang, "Composition-dependent photoluminescence intensity and prolonged recombination lifetime of perovskite CH₃NH₃PbBr₃–xCl_x films" *Chemical Communications*, 10.1039/C4CC04973J vol. 50, no. 79, pp. 11727-11730, 2014, doi: 10.1039/C4CC04973J.
- [65] E. Edri, S. Kirmayer, S. Mukhopadhyay, K. Gartsman, G. Hodes, and D. Cahen, "Elucidating the charge carrier separation and working mechanism of CH₃NH₃PbI₃–xCl_x perovskite solar cells" *Nature Communications*, vol. 5, no. 1, p. 3461, 2014/03/11 2014, doi: 10.1038/ncomms4461.

- [66] N. Kedem *et al.*, "Light-Induced Increase of Electron Diffusion Length in a p–n Junction Type CH₃NH₃PbBr₃ Perovskite Solar Cell" *The Journal of Physical Chemistry Letters*, vol. 6, no. 13, pp. 2469-2476, 2015/07/02 2015, doi: 10.1021/acs.jpcllett.5b00889.
- [67] F. Huang, M. Li, P. Siffalovic, G. Cao, and J. Tian, "From scalable solution fabrication of perovskite films towards commercialization of solar cells" *Energy & Environmental Science*, vol. 12, no. 2, pp. 518-549, 2019, doi: 10.1039/c8ee03025a.
- [68] Y. Ma and Q. Zhao, "A strategic review on processing routes towards scalable fabrication of perovskite solar cells" *Journal of Energy Chemistry*, vol. 64, pp. 538-560, 2022, doi: 10.1016/j.jechem.2021.05.019.
- [69] Z. Saki, M. M. Byranvand, N. Taghavinia, M. Kedia, and M. Saliba, "Solution-processed perovskite thin-films: the journey from lab- to large-scale solar cells" *Energy & Environmental Science*, vol. 14, no. 11, pp. 5690-5722, 2021, doi: 10.1039/d1ee02018h.
- [70] J. Ávila, C. Momblona, P. P. Boix, M. Sessolo, and H. J. Bolink, "Vapor-Deposited Perovskites: The Route to High-Performance Solar Cell Production?" *Joule*, vol. 1, no. 3, pp. 431-442, 2017, doi: 10.1016/j.joule.2017.07.014.
- [71] Y. Jiang, S. He, L. Qiu, Y. Zhao, and Y. Qi, "Perovskite solar cells by vapor deposition based and assisted methods" *Applied Physics Reviews*, vol. 9, no. 2, 2022, doi: 10.1063/5.0085221.
- [72] M. R. Leyden, L. K. Ono, S. R. Raga, Y. Kato, S. Wang, and Y. Qi, "High performance perovskite solar cells by hybrid chemical vapor deposition" *J. Mater. Chem. A*, vol. 2, no. 44, pp. 18742-18745, 2014, doi: 10.1039/c4ta04385e.
- [73] L. Qiu *et al.*, "Hybrid chemical vapor deposition enables scalable and stable Cs-FA mixed cation perovskite solar modules with a designated area of 91.8 cm² approaching 10% efficiency" *Journal of Materials Chemistry A*, vol. 7, no. 12, pp. 6920-6929, 2019, doi: 10.1039/c9ta00239a.
- [74] M. M. Tavakoli *et al.*, "Fabrication of efficient planar perovskite solar cells using a one-step chemical vapor deposition method" *Scientific Reports*, vol. 5, no. 1, p. 14083, 2015/09/22 2015, doi: 10.1038/srep14083.
- [75] I. Turkevych *et al.*, "Strategic advantages of reactive polyiodide melts for scalable perovskite photovoltaics" *Nat Nanotechnol*, vol. 14, no. 1, pp. 57-63, Jan 2019, doi: 10.1038/s41565-018-0304-y.
- [76] N.-G. Park and K. Zhu, "Scalable fabrication and coating methods for perovskite solar cells and solar modules" *Nature Reviews Materials*, vol. 5, no. 5, pp. 333-350, 2020, doi: 10.1038/s41578-019-0176-2.
- [77] A. D. Taylor *et al.*, "A general approach to high-efficiency perovskite solar cells by any antisolvent" *Nat Commun*, vol. 12, no. 1, p. 1878, Mar 25 2021, doi: 10.1038/s41467-021-22049-8.
- [78] A. Dualeh, N. Tétreault, T. Moehl, P. Gao, M. K. Nazeeruddin, and M. Grätzel, "Effect of Annealing Temperature on Film Morphology of Organic-Inorganic Hybrid Perovskite Solid-State Solar Cells" *Advanced Functional Materials*, vol. 24, no. 21, pp. 3250-3258, 2014, doi: 10.1002/adfm.201304022.

- [79] J. S. Yun *et al.*, "Benefit of Grain Boundaries in Organic–Inorganic Halide Planar Perovskite Solar Cells" *The Journal of Physical Chemistry Letters*, vol. 6, no. 5, pp. 875–880, 2015/03/05 2015, doi: 10.1021/acs.jpcclett.5b00182.
- [80] Z. Chu *et al.*, "Impact of grain boundaries on efficiency and stability of organic-inorganic trihalide perovskites" *Nature Communications*, vol. 8, no. 1, p. 2230, 2017/12/20 2017, doi: 10.1038/s41467-017-02331-4.
- [81] W. J. Yin, T. Shi, and Y. Yan, "Unique properties of halide perovskites as possible origins of the superior solar cell performance" *Adv Mater*, vol. 26, no. 27, pp. 4653–8, Jul 16 2014, doi: 10.1002/adma.201306281.
- [82] D.-Y. Son *et al.*, "Self-formed grain boundary healing layer for highly efficient CH₃NH₃PbI₃ perovskite solar cells" *Nature Energy*, vol. 1, no. 7, p. 16081, 2016/06/20 2016, doi: 10.1038/nenergy.2016.81.
- [83] T.-X. Qin *et al.*, "Quantification of electron accumulation at grain boundaries in perovskite polycrystalline films by correlative infrared-spectroscopic nanoimaging and Kelvin probe force microscopy" *Light: Science & Applications*, vol. 10, no. 1, p. 84, 2021/04/15 2021, doi: 10.1038/s41377-021-00524-7.
- [84] R. Long, J. Liu, and O. V. Prezhdo, "Unravelling the Effects of Grain Boundary and Chemical Doping on Electron-Hole Recombination in CH₃NH₃PbI₃ Perovskite by Time-Domain Atomistic Simulation" *J Am Chem Soc*, vol. 138, no. 11, pp. 3884–90, Mar 23 2016, doi: 10.1021/jacs.6b00645.
- [85] B. Bahrami *et al.*, "Nanoscale spatial mapping of charge carrier dynamics in perovskite solar cells" *Nano Today*, vol. 33, p. 100874, 2020/08/01/ 2020, doi: <https://doi.org/10.1016/j.nantod.2020.100874>.
- [86] S. I. Rahman *et al.*, "Grain Boundary Defect Passivation of Triple Cation Mixed Halide Perovskite with Hydrazine-Based Aromatic Iodide for Efficiency Improvement" *ACS Appl Mater Interfaces*, vol. 12, no. 37, pp. 41312–41322, Sep 16 2020, doi: 10.1021/acsami.0c10448.
- [87] J.-S. Park, J. Calbo, Y.-K. Jung, L. D. Whalley, and A. Walsh, "Accumulation of Deep Traps at Grain Boundaries in Halide Perovskites" *ACS Energy Letters*, vol. 4, no. 6, pp. 1321–1327, 2019, doi: 10.1021/acsenenergylett.9b00840.
- [88] S. M. Iftiqar and J. Yi, "Impact of grain boundary defect on performance of perovskite solar cell" *Materials Science in Semiconductor Processing*, vol. 79, pp. 46–52, 2018/06/01/ 2018, doi: <https://doi.org/10.1016/j.mssp.2018.01.022>.
- [89] W. Nie *et al.*, "High-efficiency solution-processed perovskite solar cells with millimeter-scale grains" *Science*, vol. 347, no. 6221, pp. 522–525, 2015/01/30 2015, doi: 10.1126/science.aaa0472.
- [90] H. Zhou *et al.*, "Interface engineering of highly efficient perovskite solar cells" *Science*, vol. 345, no. 6196, pp. 542–546, 2014/08/01 2014, doi: 10.1126/science.1254050.
- [91] B. Liu, S. Wang, Z. Ma, J. Ma, R. Ma, and C. Wang, "High-performance perovskite solar cells with large grain-size obtained by the synergy of urea and dimethyl sulfoxide"

- Applied Surface Science*, vol. 467-468, pp. 708-714, 2019/02/15/ 2019, doi: <https://doi.org/10.1016/j.apsusc.2018.10.141>.
- [92] A. Peter Amalathas, L. Landová, Z. Hájková, L. Horák, M. Ledinsky, and J. Holovský, "Controlled Growth of Large Grains in CH₃NH₃PbI₃ Perovskite Films Mediated by an Intermediate Liquid Phase without an Antisolvent for Efficient Solar Cells" *ACS Applied Energy Materials*, vol. 3, no. 12, pp. 12484-12493, 2020/12/28 2020, doi: 10.1021/acsaem.0c02441.
- [93] E. Gutierrez-Partida *et al.*, "Large-Grain Double Cation Perovskites with 18 μ s Lifetime and High Luminescence Yield for Efficient Inverted Perovskite Solar Cells" *ACS Energy Letters*, vol. 6, no. 3, pp. 1045-1054, 2021/03/12 2021, doi: 10.1021/acsenerylett.0c02642.
- [94] B. Bahrami *et al.*, "Nanoscale control of grain boundary potential barrier, dopant density and filled trap state density for higher efficiency perovskite solar cells" *INFOMAT*, vol. 2, no. 2, pp. 409-423, MAR 2020, doi: 10.1002/inf2.12055.
- [95] S. Y. Luchkin, A. F. Akbulatov, L. A. Frolova, S. A. Tsarev, P. A. Troshin, and K. J. Stevenson, "Spatially-resolved nanoscale measurements of grain boundary enhanced photocurrent in inorganic CsPbBr₃ perovskite films" *Solar Energy Materials and Solar Cells*, vol. 171, pp. 205-212, 2017/11/01/ 2017, doi: <https://doi.org/10.1016/j.solmat.2017.06.059>.
- [96] J. M. Snaider *et al.*, "Ultrafast Imaging of Carrier Transport across Grain Boundaries in Hybrid Perovskite Thin Films" *ACS Energy Letters*, vol. 3, no. 6, pp. 1402-1408, 2018/06/08 2018, doi: 10.1021/acsenerylett.8b00560.
- [97] W. Li *et al.*, "Phase Segregation Enhanced Ion Movement in Efficient Inorganic CsPbIBr₂ Solar Cells" *Advanced Energy Materials*, <https://doi.org/10.1002/aenm.201700946> vol. 7, no. 20, p. 1700946, 2017/10/01 2017, doi: <https://doi.org/10.1002/aenm.201700946>.
- [98] M.-C. Shih *et al.*, "Spatially Resolved Imaging on Photocarrier Generations and Band Alignments at Perovskite/PbI₂ Heterointerfaces of Perovskite Solar Cells by Light-Modulated Scanning Tunneling Microscopy" *Nano Letters*, vol. 17, no. 2, pp. 1154-1160, 2017/02/08 2017, doi: 10.1021/acs.nanolett.6b04803.
- [99] A. K. Jena, A. Kulkarni, and T. Miyasaka, "Halide Perovskite Photovoltaics: Background, Status, and Future Prospects" *Chem Rev*, vol. 119, no. 5, pp. 3036-3103, Mar 13 2019, doi: 10.1021/acs.chemrev.8b00539.
- [100] A. Miyata *et al.*, "Direct measurement of the exciton binding energy and effective masses for charge carriers in organic-inorganic tri-halide perovskites" *Nature Physics*, vol. 11, no. 7, pp. 582-587, 2015, doi: 10.1038/nphys3357.
- [101] J. Chen and N.-G. Park, "Materials and Methods for Interface Engineering toward Stable and Efficient Perovskite Solar Cells" *ACS Energy Letters*, vol. 5, no. 8, pp. 2742-2786, 2020, doi: 10.1021/acsenerylett.0c01240.
- [102] S. Olthof and K. Meerholz, "Substrate-dependent electronic structure and film formation of MAPbI₃ perovskites" *Scientific Reports*, vol. 7, no. 1, p. 40267, 2017/01/13 2017, doi: 10.1038/srep40267.

- [103] M. V. Khenkin *et al.*, "Consensus statement for stability assessment and reporting for perovskite photovoltaics based on ISOS procedures" *Nature Energy*, vol. 5, no. 1, pp. 35-49, 2020, doi: 10.1038/s41560-019-0529-5.
- [104] J. Nelson, *The Physics of Solar Cells*. PUBLISHED BY IMPERIAL COLLEGE PRESS AND DISTRIBUTED BY WORLD SCIENTIFIC PUBLISHING CO., 2003, p. 384.
- [105] W. Shockley and H. J. Queisser, "Detailed Balance Limit of Efficiency of p-n Junction Solar Cells" *Journal of Applied Physics*, vol. 32, no. 3, pp. 510-519, 1961, doi: 10.1063/1.1736034.
- [106] P. Selvaraj *et al.*, "Enhancing the efficiency of transparent dye-sensitized solar cells using concentrated light" *Solar Energy Materials and Solar Cells*, vol. 175, pp. 29-34, 2018/02/01/ 2018, doi: <https://doi.org/10.1016/j.solmat.2017.10.006>.
- [107] A. W. Y. Ho-Baillie, J. Zheng, M. A. Mahmud, F.-J. Ma, D. R. McKenzie, and M. A. Green, "Recent progress and future prospects of perovskite tandem solar cells" *Applied Physics Reviews*, vol. 8, no. 4, 2021, doi: 10.1063/5.0061483.
- [108] G. E. Eperon, M. T. Hörantner, and H. J. Snaith, "Metal halide perovskite tandem and multiple-junction photovoltaics" *Nature Reviews Chemistry*, vol. 1, no. 12, 2017, doi: 10.1038/s41570-017-0095.
- [109] Y. Shang, S. Hao, C. Yang, and G. Chen, "Enhancing Solar Cell Efficiency Using Photon Upconversion Materials" *Nanomaterials*, vol. 5, no. 4, 2015, doi: 10.3390/nano5041782.
- [110] S. Asahi, H. Teranishi, K. Kusaki, T. Kaizu, and T. Kita, "Two-step photon up-conversion solar cells" *Nature Communications*, vol. 8, no. 1, p. 14962, 2017/04/06 2017, doi: 10.1038/ncomms14962.
- [111] E. Aydin *et al.*, "Ligand-bridged charge extraction and enhanced quantum efficiency enable efficient n-i-p perovskite/silicon tandem solar cells" *Energy & Environmental Science*, vol. 14, no. 8, pp. 4377-4390, 2021, doi: 10.1039/d1ee01206a.
- [112] M. De Bastiani *et al.*, "Efficient bifacial monolithic perovskite/silicon tandem solar cells via bandgap engineering" *Nature Energy*, vol. 6, no. 2, pp. 167-175, 2021, doi: 10.1038/s41560-020-00756-8.
- [113] F. H. Isikgor *et al.*, "Concurrent cationic and anionic perovskite defect passivation enables 27.4% perovskite/silicon tandems with suppression of halide segregation" *Joule*, vol. 5, no. 6, pp. 1566-1586, 2021, doi: 10.1016/j.joule.2021.05.013.
- [114] E. M. Tennyson *et al.*, "Multimodal Microscale Imaging of Textured Perovskite-Silicon Tandem Solar Cells" *ACS Energy Letters*, vol. 6, no. 6, pp. 2293-2304, 2021/06/11 2021, doi: 10.1021/acsenergylett.1c00568.
- [115] R. Lin *et al.*, "All-perovskite tandem solar cells with improved grain surface passivation" *Nature*, vol. 603, no. 7899, pp. 73-78, 2022/03/01 2022, doi: 10.1038/s41586-021-04372-8.
- [116] X. Zheng, A. Y. Alsalloum, Y. Hou, E. H. Sargent, and O. M. Bakr, "All-Perovskite Tandem Solar Cells: A Roadmap to Uniting High Efficiency with High Stability"

- Accounts of Materials Research*, vol. 1, no. 1, pp. 63-76, 2020/10/23 2020, doi: 10.1021/accountsmr.0c00017.
- [117] X. Chen *et al.*, "Efficient and Reproducible Monolithic Perovskite/Organic Tandem Solar Cells with Low-Loss Interconnecting Layers" *Joule*, vol. 4, no. 7, pp. 1594-1606, 2020/07/15/ 2020, doi: <https://doi.org/10.1016/j.joule.2020.06.006>.
- [118] Y.-M. Xie, Q. Xue, Q. Yao, S. Xie, T. Niu, and H.-L. Yip, "Monolithic perovskite/organic tandem solar cells: Developments, prospects, and challenges" *Nano Select*, <https://doi.org/10.1002/nano.202000287> vol. 2, no. 7, pp. 1266-1276, 2021/07/01 2021, doi: <https://doi.org/10.1002/nano.202000287>.
- [119] L. K. Ono, E. J. Juarez-Perez, and Y. Qi, "Progress on Perovskite Materials and Solar Cells with Mixed Cations and Halide Anions" *ACS Appl Mater Interfaces*, vol. 9, no. 36, pp. 30197-30246, Sep 13 2017, doi: 10.1021/acsami.7b06001.
- [120] N. J. Jeon *et al.*, "Compositional engineering of perovskite materials for high-performance solar cells" *Nature*, vol. 517, no. 7535, pp. 476-80, Jan 22 2015, doi: 10.1038/nature14133.
- [121] G. Yang, H. Zhang, G. Li, and G. Fang, "Stabilizer-assisted growth of formamminium-based perovskites for highly efficient and stable planar solar cells with over 22% efficiency" *Nano Energy*, vol. 63, p. 103835, 2019/09/01/ 2019, doi: <https://doi.org/10.1016/j.nanoen.2019.06.031>.
- [122] X. Liu *et al.*, "Highly efficient wide-band-gap perovskite solar cells fabricated by sequential deposition method" *Nano Energy*, vol. 86, p. 106114, 2021/08/01/ 2021, doi: <https://doi.org/10.1016/j.nanoen.2021.106114>.
- [123] T. D. Siegler, T. M. Shimpi, W. S. Sampath, and B. A. Korgel, "Development of wide bandgap perovskites for next-generation low-cost CdTe tandem solar cells" *Chemical Engineering Science*, vol. 199, pp. 388-397, 2019, doi: 10.1016/j.ces.2019.01.003.
- [124] L. Fu, H. Li, L. Wang, R. Yin, B. Li, and L. Yin, "Defect passivation strategies in perovskites for an enhanced photovoltaic performance" *Energy & Environmental Science*, vol. 13, no. 11, pp. 4017-4056, 2020, doi: 10.1039/d0ee01767a.
- [125] B. Chen, P. N. Rudd, S. Yang, Y. Yuan, and J. Huang, "Imperfections and their passivation in halide perovskite solar cells" *Chem Soc Rev*, vol. 48, no. 14, pp. 3842-3867, Jul 15 2019, doi: 10.1039/c8cs00853a.
- [126] C. Li, H. Li, Z. Zhu, N. Cui, Z. a. Tan, and R. Yang, "Perovskite Passivation Strategies for Efficient and Stable Solar Cells" *Solar RRL*, vol. 5, no. 1, 2020, doi: 10.1002/solr.202000579.
- [127] M. Pratheek, T. Abhinav, S. Bhattacharya, G. K. Chandra, and P. Predeep, "Recent progress on defect passivation in perovskites for solar cell application" *Materials Science for Energy Technologies*, vol. 4, pp. 282-289, 2021, doi: 10.1016/j.mset.2021.07.003.
- [128] C. Lan, Z. Zhou, R. Wei, and J. C. Ho, "Two-dimensional perovskite materials: From synthesis to energy-related applications" *Materials Today Energy*, vol. 11, pp. 61-82, 2019/03/01/ 2019, doi: <https://doi.org/10.1016/j.mtener.2018.10.008>.

- [129] A. Dey *et al.*, "State of the Art and Prospects for Halide Perovskite Nanocrystals" *ACS Nano*, vol. 15, no. 7, pp. 10775-10981, 2021/07/27 2021, doi: 10.1021/acsnano.0c08903.
- [130] B. Turedi, V. Yeddu, X. Zheng, D. Y. Kim, O. M. Bakr, and M. I. Saidaminov, "Perovskite Single-Crystal Solar Cells: Going Forward" *ACS Energy Letters*, vol. 6, no. 2, pp. 631-642, 2021/02/12 2021, doi: 10.1021/acseenergylett.0c02573.
- [131] J. A. Christians, S. N. Habisreutinger, J. J. Berry, and J. M. Luther, "Stability in Perovskite Photovoltaics: A Paradigm for Newfangled Technologies" *ACS Energy Letters*, vol. 3, no. 9, pp. 2136-2143, 2018, doi: 10.1021/acseenergylett.8b00914.
- [132] S. Macpherson *et al.*, "Local Nanoscale Phase Impurities are Degradation Sites in Halide Perovskites" *Nature*, 607, pp. 294-300, 2022, doi: <https://doi.org/10.1038/s41586-022-04872-1>.
- [133] T. W. Jones *et al.*, "Lattice strain causes non-radiative losses in halide perovskites" *Energy & Environmental Science*, 10.1039/C8EE02751J vol. 12, no. 2, pp. 596-606, 2019, doi: 10.1039/C8EE02751J.
- [134] S. Jariwala *et al.*, "Local Crystal Misorientation Influences Non-radiative Recombination in Halide Perovskites" *Joule*, vol. 3, no. 12, pp. 3048-3060, 2019/12/18/2019, doi: <https://doi.org/10.1016/j.joule.2019.09.001>.
- [135] S. Chen *et al.*, "Spatial Distribution of Lead Iodide and Local Passivation on Organo-Lead Halide Perovskite" *ACS Appl Mater Interfaces*, vol. 9, no. 7, pp. 6072-6078, Feb 22 2017, doi: 10.1021/acsaami.6b15504.
- [136] P. Gratia *et al.*, "Intrinsic Halide Segregation at Nanometer Scale Determines the High Efficiency of Mixed Cation/Mixed Halide Perovskite Solar Cells" *Journal of the American Chemical Society*, vol. 138, no. 49, pp. 15821-15824, 2016/12/14 2016, doi: 10.1021/jacs.6b10049.
- [137] L. K. Jagadamma, P. R. Edwards, R. W. Martin, A. Ruseckas, and I. D. W. Samuel, "Nanoscale Heterogeneity in CsPbBr₃ and CsPbBr₃:KI Perovskite Films Revealed by Cathodoluminescence Hyperspectral Imaging" *ACS APPLIED ENERGY MATERIALS*, vol. 4, no. 3, pp. 2707-2715, MAR 22 2021, doi: 10.1021/acsaem.0c03154.
- [138] V. W. Bergmann *et al.*, "Real-space observation of unbalanced charge distribution inside a perovskite-sensitized solar cell" *Nature Communications*, vol. 5, no. 1, p. 5001, 2014/09/22 2014, doi: 10.1038/ncomms6001.
- [139] Y. Kutes, L. Ye, Y. Zhou, S. Pang, B. D. Huey, and N. P. Padture, "Direct Observation of Ferroelectric Domains in Solution-Processed CH₃NH₃PbI₃ Perovskite Thin Films" *The Journal of Physical Chemistry Letters*, vol. 5, no. 19, pp. 3335-3339, 2014/10/02 2014, doi: 10.1021/jz501697b.
- [140] D. Nanova *et al.*, "Unraveling the Nanoscale Morphologies of Mesoporous Perovskite Solar Cells and Their Correlation to Device Performance" *Nano Letters*, vol. 14, no. 5, pp. 2735-2740, 2014/05/14 2014, doi: 10.1021/nl5006838.
- [141] M. Xiao *et al.*, "A Fast Deposition-Crystallization Procedure for Highly Efficient Lead Iodide Perovskite Thin-Film Solar Cells" *Angewandte Chemie International Edition*,

<https://doi.org/10.1002/anie.201405334> vol. 53, no. 37, pp. 9898-9903, 2014/09/08 2014, doi: <https://doi.org/10.1002/anie.201405334>.

- [142] N. Adhikari *et al.*, "Interfacial Study To Suppress Charge Carrier Recombination for High Efficiency Perovskite Solar Cells" *ACS APPLIED MATERIALS & INTERFACES*, vol. 7, no. 48, pp. 26445-26454, DEC 9 2015, doi: 10.1021/acsami.5b09797.
- [143] C. G. Bischak, E. M. Sanehira, J. T. Precht, J. M. Luther, and N. S. Ginsberg, "Heterogeneous Charge Carrier Dynamics in Organic-Inorganic Hybrid Materials: Nanoscale Lateral and Depth-Dependent Variation of Recombination Rates in Methylammonium Lead Halide Perovskite Thin Films" *Nano Letters*, vol. 15, no. 7, pp. 4799-4807, 2015/07/08 2015, doi: 10.1021/acs.nanolett.5b01917.
- [144] J. Chae, Q. F. Dong, J. S. Huang, and A. Centrone, "Chloride Incorporation Process in CH₃NH₃PbI₃-xCl_x Perovskites via Nanoscale Bandgap Maps" *NANO LETTERS*, vol. 15, no. 12, pp. 8114-8121, DEC 2015, doi: 10.1021/acs.nanolett.5b03556.
- [145] B. Conings *et al.*, "Intrinsic Thermal Instability of Methylammonium Lead Trihalide Perovskite" *Advanced Energy Materials*, <https://doi.org/10.1002/aenm.201500477> vol. 5, no. 15, p. 1500477, 2015/08/01 2015, doi: <https://doi.org/10.1002/aenm.201500477>.
- [146] J.-J. Li, J.-Y. Ma, Q.-Q. Ge, J.-S. Hu, D. Wang, and L.-J. Wan, "Microscopic Investigation of Grain Boundaries in Organolead Halide Perovskite Solar Cells" *ACS Applied Materials & Interfaces*, vol. 7, no. 51, pp. 28518-28523, 2015/12/30 2015, doi: 10.1021/acsami.5b09801.
- [147] H. C. Liao *et al.*, "Hierarchical i-p and i-n porous heterojunction in planar perovskite solar cells" *JOURNAL OF MATERIALS CHEMISTRY A*, vol. 3, no. 19, pp. 10526-10535, 2015, doi: 10.1039/c5ta02184g.
- [148] J. Ma and L. W. Wang, "Nanoscale Charge Localization Induced by Random Orientations of Organic Molecules in Hybrid Perovskite CH₃NH₃PbI₃" *NANO LETTERS*, vol. 15, no. 1, pp. 248-253, JAN 2015, doi: 10.1021/nl503494y.
- [149] S. Mastroianni *et al.*, "Analysing the effect of crystal size and structure in highly efficient CH₃NH₃PbI₃ perovskite solar cells by spatially resolved photo- and electroluminescence imaging" *NANOSCALE*, vol. 7, no. 46, pp. 19653-19662, 2015, doi: 10.1039/c5nr05308k.
- [150] F. Matsumoto, S. M. Vorpahl, J. Q. Banks, E. Sengupta, and D. S. Ginger, "Photodecomposition and Morphology Evolution of Organometal Halide Perovskite Solar Cells" *The Journal of Physical Chemistry C*, vol. 119, no. 36, pp. 20810-20816, 2015/09/10 2015, doi: 10.1021/acs.jpcc.5b06269.
- [151] R. Ohmann *et al.*, "Real-Space Imaging of the Atomic Structure of Organic-Inorganic Perovskite" *Journal of the American Chemical Society*, vol. 137, no. 51, pp. 16049-16054, 2015/12/30 2015, doi: 10.1021/jacs.5b08227.
- [152] M. J. Simpson, B. Doughty, B. Yang, K. Xiao, and Y.-Z. Ma, "Spatial Localization of Excitons and Charge Carriers in Hybrid Perovskite Thin Films" *The Journal of Physical Chemistry Letters*, vol. 6, no. 15, pp. 3041-3047, 2015/08/06 2015, doi: 10.1021/acs.jpcclett.5b01050.

- [153] B. R. Watson, B. Yang, K. Xiao, Y.-Z. Ma, B. Doughty, and T. R. Calhoun, "Elucidation of Perovskite Film Micro-Orientations Using Two-Photon Total Internal Reflectance Fluorescence Microscopy" *The Journal of Physical Chemistry Letters*, vol. 6, no. 16, pp. 3283-3288, 2015/08/20 2015, doi: 10.1021/acs.jpcclett.5b01474.
- [154] J. Xu *et al.*, "Perovskite–fullerene hybrid materials suppress hysteresis in planar diodes" *Nature Communications*, vol. 6, no. 1, p. 7081, 2015/05/08 2015, doi: 10.1038/ncomms8081.
- [155] M. Yang, Y. Zhou, Y. Zeng, C.-S. Jiang, N. P. Padture, and K. Zhu, "Square-Centimeter Solution-Processed Planar CH₃NH₃PbI₃ Perovskite Solar Cells with Efficiency Exceeding 15%" *Advanced Materials*, <https://doi.org/10.1002/adma.201502586> vol. 27, no. 41, pp. 6363-6370, 2015/11/01 2015, doi: <https://doi.org/10.1002/adma.201502586>.
- [156] Y. Zhou *et al.*, "Crystal Morphologies of Organolead Trihalide in Mesoscopic/Planar Perovskite Solar Cells" *The Journal of Physical Chemistry Letters*, vol. 6, no. 12, pp. 2292-2297, 2015/06/18 2015, doi: 10.1021/acs.jpcclett.5b00981.
- [157] D. W. deQuilettes *et al.*, "Photoluminescence Lifetimes Exceeding 8 μ s and Quantum Yields Exceeding 30% in Hybrid Perovskite Thin Films by Ligand Passivation" *ACS Energy Letters*, vol. 1, no. 2, pp. 438-444, 2016/08/12 2016, doi: 10.1021/acsenerylett.6b00236.
- [158] G. Divitini, S. Cacovich, F. Matteocci, L. Cinà, A. Di Carlo, and C. Ducati, "In situ observation of heat-induced degradation of perovskite solar cells" *Nature Energy*, vol. 1, no. 2, p. 15012, 2016/01/18 2016, doi: 10.1038/nenergy.2015.12.
- [159] G. E. Eperon, D. Moerman, and D. S. Ginger, "Anticorrelation between Local Photoluminescence and Photocurrent Suggests Variability in Contact to Active Layer in Perovskite Solar Cells" *ACS Nano*, vol. 10, no. 11, pp. 10258-10266, 2016/11/22 2016, doi: 10.1021/acsnano.6b05825.
- [160] O. Hentz, Z. B. Zhao, and S. Gradecak, "Impacts of Ion Segregation on Local Optical Properties in Mixed Halide Perovskite Films" *Nano Letters*, vol. 16, no. 2, pp. 1485-1490, FEB 2016, doi: 10.1021/acs.nanolett.5b05181.
- [161] I. M. Hermes *et al.*, "Ferroelastic Fingerprints in Methylammonium Lead Iodide Perovskite" *The Journal of Physical Chemistry C*, vol. 120, no. 10, pp. 5724-5731, 2016/03/17 2016, doi: 10.1021/acs.jpcc.5b11469.
- [162] T. Hwang *et al.*, "Investigation of chlorine-mediated microstructural evolution of CH₃NH₃PbI₃(Cl) grains for high optoelectronic responses" *Nano Energy*, vol. 25, pp. 91-99, 2016/07/01/ 2016, doi: <https://doi.org/10.1016/j.nanoen.2016.04.044>.
- [163] Q. Jeangros *et al.*, "In Situ TEM Analysis of Organic–Inorganic Metal-Halide Perovskite Solar Cells under Electrical Bias" *Nano Letters*, vol. 16, no. 11, pp. 7013-7018, 2016/11/09 2016, doi: 10.1021/acs.nanolett.6b03158.
- [164] Y. Kutes, Y. Zhou, J. L. Bosse, J. Steffes, N. P. Padture, and B. D. Huey, "Mapping the Photoresponse of CH₃NH₃PbI₃ Hybrid Perovskite Thin Films at the Nanoscale" *Nano Letters*, vol. 16, no. 6, pp. 3434-3441, 2016/06/08 2016, doi: 10.1021/acs.nanolett.5b04157.

- [165] S. Y. Leblebici *et al.*, "Facet-dependent photovoltaic efficiency variations in single grains of hybrid halide perovskite" *Nature Energy*, vol. 1, no. 8, p. 16093, 2016/07/04 2016, doi: 10.1038/nenergy.2016.93.
- [166] B. Lee *et al.*, "Evaluating the Optoelectronic Quality of Hybrid Perovskites by Conductive Atomic Force Microscopy with Noise Spectroscopy" *ACS Applied Materials & Interfaces*, vol. 8, no. 45, pp. 30985-30991, 2016/11/16 2016, doi: 10.1021/acsami.6b11011.
- [167] J. J. Li, J. Y. Ma, J. S. Hu, D. Wang, and L. J. Wan, "Influence of N,N-Dimethylformamide Annealing on the Local Electrical Properties of Organometal Halide Perovskite Solar Cells: an Atomic Force Microscopy Investigation" *ACS Applied Materials & Interfaces*, vol. 8, no. 39, pp. 26002-26007, OCT 5 2016, doi: 10.1021/acsami.6b07647.
- [168] Y. Luo *et al.*, "Spatially Heterogeneous Chlorine Incorporation in Organic-Inorganic Perovskite Solar Cells" *Chemistry of Materials*, vol. 28, no. 18, pp. 6536-6543, 2016/09/27 2016, doi: 10.1021/acs.chemmater.6b02065.
- [169] G. A. MacDonald *et al.*, "Methylammonium lead iodide grain boundaries exhibit depth-dependent electrical properties" *Energy & Environmental Science*, vol. 9, no. 12, pp. 3642-3649, 2016, doi: 10.1039/c6ee01889k.
- [170] S. Pandya, A. R. Damodaran, R. Xu, S.-L. Hsu, J. C. Agar, and L. W. Martin, "Strain-induced growth instability and nanoscale surface patterning in perovskite thin films" *Scientific Reports*, vol. 6, no. 1, p. 26075, 2016/05/19 2016, doi: 10.1038/srep26075.
- [171] Y. Shao *et al.*, "Grain boundary dominated ion migration in polycrystalline organic-inorganic halide perovskite films" *Energy & Environmental Science*, 10.1039/C6EE00413J vol. 9, no. 5, pp. 1752-1759, 2016, doi: 10.1039/C6EE00413J.
- [172] L. She, M. Liu, and D. Zhong, "Atomic Structures of CH₃NH₃PbI₃ (001) Surfaces" *ACS Nano*, vol. 10, no. 1, pp. 1126-1131, 2016/01/26 2016, doi: 10.1021/acsnano.5b06420.
- [173] E. M. Talbert *et al.*, "Interplay of structural and compositional effects on carrier recombination in mixed-halide perovskites" *RSC Advances*, vol. 6, no. 90, pp. 86947-86954, 2016, doi: 10.1039/c6ra16505b.
- [174] B. Yang *et al.*, "Observation of Nanoscale Morphological and Structural Degradation in Perovskite Solar Cells by in Situ TEM" *ACS Applied Materials & Interfaces*, vol. 8, no. 47, pp. 32333-32340, 2016/11/30 2016, doi: 10.1021/acsami.6b11341.
- [175] A. J. Yost *et al.*, "Coexistence of Two Electronic Nano-Phases on a CH₃NH₃PbI₃-xCl_x Surface Observed in STM Measurements" *ACS Applied Materials & Interfaces*, vol. 8, no. 42, pp. 29110-29116, OCT 26 2016, doi: 10.1021/acsami.6b07721.
- [176] H. Yuan *et al.*, "Degradation of Methylammonium Lead Iodide Perovskite Structures through Light and Electron Beam Driven Ion Migration" *The Journal of Physical Chemistry Letters*, vol. 7, no. 3, pp. 561-566, 2016/02/04 2016, doi: 10.1021/acs.jpcllett.5b02828.

- [177] J. S. Yun *et al.*, "Critical Role of Grain Boundaries for Ion Migration in Formamidinium and Methylammonium Lead Halide Perovskite Solar Cells" *Advanced Energy Materials*, <https://doi.org/10.1002/aenm.201600330> vol. 6, no. 13, p. 1600330, 2016/07/01 2016, doi: <https://doi.org/10.1002/aenm.201600330>.
- [178] Z. X. Zhao, X. Y. Chen, H. Q. Wu, X. M. Wu, and G. Z. Cao, "Probing the Photovoltage and Photocurrent in Perovskite Solar Cells with Nanoscale Resolution" *Advanced Functional Materials*, vol. 26, no. 18, pp. 3048-3058, May 10 2016, doi: 10.1002/adfm.201504451.
- [179] A. Al Mamun, T. T. Ava, H. J. Jeong, M. S. Jeong, and G. Namkoong, "A deconvoluted PL approach to probe the charge carrier dynamics of the grain interior and grain boundary of a perovskite film for perovskite solar cell applications" *Physical Chemistry Chemical Physics*, vol. 19, no. 13, pp. 9143-9148, APR 7 2017, doi: 10.1039/c7cp01140g.
- [180] S. Berweger *et al.*, "Electronic and Morphological Inhomogeneities in Pristine and Deteriorated Perovskite Photovoltaic Films" *Nano Letters*, vol. 17, no. 3, pp. 1796-1801, 2017/03/08 2017, doi: 10.1021/acs.nanolett.6b05119.
- [181] C. G. Bischak *et al.*, "Origin of Reversible Photoinduced Phase Separation in Hybrid Perovskites" *Nano Letters*, vol. 17, no. 2, pp. 1028-1033, 2017, doi: 10.1021/acs.nanolett.6b04453.
- [182] R. Brenes *et al.*, "Metal Halide Perovskite Polycrystalline Films Exhibiting Properties of Single Crystals" *Joule*, vol. 1, no. 1, pp. 155-167, 2017, doi: <https://doi.org/10.1016/j.joule.2017.08.006>.
- [183] S. Cacovich *et al.*, "Gold and iodine diffusion in large area perovskite solar cells under illumination" *Nanoscale*, vol. 9, no. 14, pp. 4700-4706, APR 14 2017, doi: 10.1039/c7nr00784a.
- [184] J. L. Garrett, E. M. Tennyson, M. Hu, J. Huang, J. N. Munday, and M. S. Leite, "Real-Time Nanoscale Open-Circuit Voltage Dynamics of Perovskite Solar Cells" *Nano Letters*, vol. 17, no. 4, pp. 2554-2560, 2017/04/12 2017, doi: 10.1021/acs.nanolett.7b00289.
- [185] A. Gomez, M. Gich, A. Carretero-Genevri, T. Puig, and X. Obradors, "Piezo-generated charge mapping revealed through direct piezoelectric force microscopy" *Nature Communications*, vol. 8, no. 1, p. 1113, 2017/10/24 2017, doi: 10.1038/s41467-017-01361-2.
- [186] S. Ham, Y. J. Choi, J.-W. Lee, N.-G. Park, and D. Kim, "Impact of Excess CH₃NH₃I on Free Carrier Dynamics in High-Performance Nonstoichiometric Perovskites" *The Journal of Physical Chemistry C*, vol. 121, no. 5, pp. 3143-3148, 2017/02/09 2017, doi: 10.1021/acs.jpcc.6b11984.
- [187] V. Kumar *et al.*, "Nanoscale Mapping of Bromide Segregation on the Cross Sections of Complex Hybrid Perovskite Photovoltaic Films Using Secondary Electron Hyperspectral Imaging in a Scanning Electron Microscope" *ACS Omega*, vol. 2, no. 5, pp. 2126-2133, MAY 2017, doi: 10.1021/acsomega.7b00265.

- [188] J.-W. Lee *et al.*, "A Bifunctional Lewis Base Additive for Microscopic Homogeneity in Perovskite Solar Cells" *Chem*, vol. 3, no. 2, pp. 290-302, 2017/08/10/ 2017, doi: <https://doi.org/10.1016/j.chempr.2017.05.020>.
- [189] J.-W. Lee *et al.*, "The Interplay between Trap Density and Hysteresis in Planar Heterojunction Perovskite Solar Cells" *Nano Letters*, vol. 17, no. 7, pp. 4270-4276, 2017/07/12 2017, doi: 10.1021/acs.nanolett.7b01211.
- [190] J. Y. Li *et al.*, "Touching is believing: interrogating halide perovskite solar cells at the nanoscale via scanning probe microscopy" *NPJ Quantum Materials*, vol. 2, 2017, doi: 10.1038/s41535-017-0061-4.
- [191] W. Li *et al.*, "Phase Segregation Enhanced Ion Movement in Efficient Inorganic CsPbIBr₂ Solar Cells" *Advanced Energy Materials*, vol. 7, no. 20, 2017, doi: 10.1002/aenm.201700946.
- [192] G. A. MacDonald *et al.*, "Determination of the True Lateral Grain Size in Organic–Inorganic Halide Perovskite Thin Films" *ACS Applied Materials & Interfaces*, vol. 9, no. 39, pp. 33565-33570, 2017/10/04 2017, doi: 10.1021/acsami.7b11434.
- [193] D. Moerman, G. E. Eperon, J. T. Precht, and D. S. Ginger, "Correlating Photoluminescence Heterogeneity with Local Electronic Properties in Methylammonium Lead Tribromide Perovskite Thin Films" *Chemistry of Materials*, vol. 29, no. 13, pp. 5484-5492, 2017/07/11 2017, doi: 10.1021/acs.chemmater.7b00235.
- [194] S. Nah, B. Spokoyny, C. Stoumpos, C. M. M. Soe, M. Kanatzidis, and E. Harel, "Spatially segregated free-carrier and exciton populations in individual lead halide perovskite grains" *Nature Photonics*, vol. 11, no. 5, pp. 285-288, 2017/05/01 2017, doi: 10.1038/nphoton.2017.36.
- [195] H. Röhm, T. Leonhard, M. J. Hoffmann, and A. Colmann, "Ferroelectric domains in methylammonium lead iodide perovskite thin-films" *Energy & Environmental Science*, 10.1039/C7EE00420F vol. 10, no. 4, pp. 950-955, 2017, doi: 10.1039/C7EE00420F.
- [196] M. U. Rothmann *et al.*, "Direct observation of intrinsic twin domains in tetragonal CH₃NH₃PbI₃" *Nature Communications*, vol. 8, no. 1, p. 14547, 2017/02/23 2017, doi: 10.1038/ncomms14547.
- [197] M. Salado, R. K. Kokal, L. Calio, S. Kazim, M. Deepa, and S. Ahmad, "Identifying the charge generation dynamics in Cs⁺-based triple cation mixed perovskite solar cells" *Physical Chemistry Chemical Physics*, vol. 19, no. 34, pp. 22905-22914, 2017, doi: 10.1039/c7cp03760k.
- [198] D. Seol *et al.*, "Origin of Hysteresis in CH₃NH₃PbI₃ Perovskite Thin Films" *Advanced Functional Materials*, <https://doi.org/10.1002/adfm.201701924> vol. 27, no. 37, p. 1701924, 2017/10/01 2017, doi: <https://doi.org/10.1002/adfm.201701924>.
- [199] M. J. Simpson, B. Doughty, S. Das, K. Xiao, and Y.-Z. Ma, "Separating Bulk and Surface Contributions to Electronic Excited-State Processes in Hybrid Mixed Perovskite Thin Films via Multimodal All-Optical Imaging" *The Journal of Physical Chemistry Letters*, vol. 8, no. 14, pp. 3299-3305, 2017/07/20 2017, doi: 10.1021/acs.jpcclett.7b01368.

- [200] E. Strelcov *et al.*, "CH₃NH₃PbI₃ perovskites: Ferroelasticity revealed" *Science Advances*, vol. 3, no. 4, 2017, doi: 10.1126/sciadv.1602165.
- [201] M. Stuckelberger *et al.*, "Charge Collection in Hybrid Perovskite Solar Cells: Relation to the Nanoscale Elemental Distribution" *IEEE Journal of Photovoltaics*, vol. 7, no. 2, pp. 590-597, 2017, doi: 10.1109/JPHOTOV.2016.2633801.
- [202] B. Su *et al.*, "Macroscale and Nanoscale Morphology Evolution during in Situ Spray Coating of Titania Films for Perovskite Solar Cells" *ACS Applied Materials & Interfaces*, vol. 9, no. 50, pp. 43724-43732, 2017, doi: 10.1021/acsami.7b14850.
- [203] Q. Wang *et al.*, "Scaling behavior of moisture-induced grain degradation in polycrystalline hybrid perovskite thin films" *Energy & Environmental Science*, 10.1039/C6EE02941H vol. 10, no. 2, pp. 516-522, 2017, doi: 10.1039/C6EE02941H.
- [204] M. Yang *et al.*, "Do grain boundaries dominate non-radiative recombination in CH₃NH₃PbI₃ perovskite thin films?" *Physical Chemistry Chemical Physics*, 10.1039/C6CP08770A vol. 19, no. 7, pp. 5043-5050, 2017, doi: 10.1039/C6CP08770A.
- [205] Y. Yoon *et al.*, "Nanoscale imaging and spectroscopy of band gap and defects in polycrystalline photovoltaic devices" *Nanoscale*, vol. 9, no. 23, pp. 7771-7780, 2017, doi: 10.1039/c7nr01480e.
- [206] Y. X. Zong *et al.*, "Homogenous Alloys of Formamidinium Lead Triiodide and Cesium Tin Triiodide for Efficient Ideal-Bandgap Perovskite Solar Cells" *Angewandte Chemie-International Edition*, vol. 56, no. 41, pp. 12658-12662, 2017, doi: 10.1002/anie.201705965.
- [207] G. W. P. Adhyaksa *et al.*, "Understanding Detrimental and Beneficial Grain Boundary Effects in Halide Perovskites" *Advanced Materials*, vol. 30, no. 52, 2018, doi: 10.1002/adma.201804792.
- [208] R. Brenes, C. Eames, V. Bulovic, M. S. Islam, and S. D. Stranks, "The Impact of Atmosphere on the Local Luminescence Properties of Metal Halide Perovskite Grains" *Adv Mater*, vol. 30, no. 15, p. e1706208, Apr 2018, doi: 10.1002/adma.201706208.
- [209] S. Cacovich *et al.*, "Unveiling the Chemical Composition of Halide Perovskite Films Using Multivariate Statistical Analyses" *ACS Applied Energy Materials*, vol. 1, no. 12, pp. 7174-7181, 2018/12/24 2018, doi: 10.1021/acsaem.8b01622.
- [210] R. Ciesielski *et al.*, "Grain Boundaries Act as Solid Walls for Charge Carrier Diffusion in Large Crystal MAPI Thin Films" *ACS Applied Materials & Interfaces*, vol. 10, no. 9, pp. 7974-7981, 2018/03/07 2018, doi: 10.1021/acsami.7b17938.
- [211] L. Collins *et al.*, "Time resolved surface photovoltage measurements using a big data capture approach to KPFM" *Nanotechnology*, vol. 29, no. 44, p. 445703, 2018/09/06 2018, doi: 10.1088/1361-6528/aad873.
- [212] X. F. Deng *et al.*, "Dynamic study of the light soaking effect on perovskite solar cells by in-situ photoluminescence microscopy" *Nano Energy*, vol. 46, pp. 356-364, APR 2018, doi: 10.1016/j.nanoen.2018.02.024.
- [213] S. Draguta *et al.*, "A quantitative and spatially resolved analysis of the performance-bottleneck in high efficiency, planar hybrid perovskite solar cells" *Energy &*

- Environmental Science*, 10.1039/C7EE03654J vol. 11, no. 4, pp. 960-969, 2018, doi: 10.1039/C7EE03654J.
- [214] T. Du *et al.*, "Probing and Controlling Intragrain Crystallinity for Improved Low Temperature-Processed Perovskite Solar Cells" *Advanced Functional Materials*, vol. 28, no. 51, doi: 10.1002/adfm.201803943.
- [215] N. Faraji, C. J. Qin, T. Matsushimia, C. Adachi, and J. Seidel, "Grain Boundary Engineering of Halide Perovskite CH₃NH₃PbI₃ Solar Cells with Photochemically Active Additives" *Journal of Physical Chemistry C*, vol. 122, no. 9, pp. 4817-4821, doi: 10.1021/acs.jpcc.8b00804.
- [216] B. J. Foley *et al.*, "Impact of Crystallographic Orientation Disorders on Electronic Heterogeneities in Metal Halide Perovskite Thin Films" *Nano Letters*, vol. 18, no. 10, pp. 6271-6278, OCT 2018, doi: 10.1021/acs.nanolett.8b02417.
- [217] A. Gomez, S. Sanchez, M. Campoy-Quiles, and A. Abate, "Topological distribution of reversible and non-reversible degradation in perovskite solar cells" *Nano Energy*, vol. 45, pp. 94-100, MAR 2018, doi: 10.1016/j.nanoen.2017.12.040.
- [218] M. N. F. Hoque, R. He, J. Warzywoda, and Z. Fan, "Effects of Moisture-Based Grain Boundary Passivation on Cell Performance and Ionic Migration in Organic-Inorganic Halide Perovskite Solar Cells" *ACS Applied Materials & Interfaces*, vol. 10, no. 36, pp. 30322-30329, 2018/09/12 2018, doi: 10.1021/acsami.8b08981.
- [219] J. M. Howard *et al.*, "Humidity-Induced Photoluminescence Hysteresis in Variable Cs/Br Ratio Hybrid Perovskites" *The Journal of Physical Chemistry Letters*, vol. 9, no. 12, pp. 3463-3469, 2018/06/21 2018, doi: 10.1021/acs.jpcclett.8b01357.
- [220] C. Jiang and P. Zhang, "Crystalline orientation dependent photoresponse and heterogeneous behaviors of grain boundaries in perovskite solar cells" *Journal of Applied Physics*, vol. 123, no. 8, p. 083105, 2018/02/28 2018, doi: 10.1063/1.5007857.
- [221] H. J. Jung, D. Kim, S. Kim, J. Park, V. P. Dravid, and B. Shin, "Stability of Halide Perovskite Solar Cell Devices: In Situ Observation of Oxygen Diffusion under Biasing" *Advanced Materials*, vol. 30, no. 39, doi: 10.1002/adma.201802769.
- [222] T. W. Kim, M. Kim, L. Cojocar, S. Uchida, and H. Segawa, "Direct Observation of the Tunneling Phenomenon in Organometal Halide Perovskite Solar Cells and Its Influence on Hysteresis" *ACS Energy Letters*, vol. 3, no. 11, pp. 2743-2749, doi: 10.1021/acsenerylett.8b01701.
- [223] T. H. Liu *et al.*, "Stable Formamidinium-Based Perovskite Solar Cells via In Situ Grain Encapsulation" *Advanced Energy Materials*, vol. 8, no. 22, AUG 6 2018, doi: 10.1002/aenm.201800232.
- [224] Y. Liu *et al.*, "Dynamic behavior of CH₃NH₃PbI₃ perovskite twin domains" *Applied Physics Letters*, vol. 113, no. 7, p. 072102, 2018/08/13 2018, doi: 10.1063/1.5041256.
- [225] Y. Liu *et al.*, "Chemical nature of ferroelastic twin domains in CH₃NH₃PbI₃ perovskite" *Nature Materials*, vol. 17, no. 11, pp. 1013-1019, 2018/11/01 2018, doi: 10.1038/s41563-018-0152-z.

- [226] S. Nah, B. M. Spokoyny, C. M. M. Soe, C. C. Stoumpos, M. G. Kanatzidis, and E. Harel, "Ultrafast Imaging of Carrier Cooling in Metal Halide Perovskite Thin Films" *Nano Letters*, vol. 18, no. 2, pp. 1044-1048, 2018/02/14 2018, doi: 10.1021/acs.nanolett.7b04520.
- [227] M. U. Rothmann *et al.*, "Structural and Chemical Changes to CH₃NH₃PbI₃ Induced by Electron and Gallium Ion Beams" *Advanced Materials*, vol. 30, no. 25, JUN 20 2018, doi: 10.1002/adma.201800629.
- [228] K. Song *et al.*, "SKPM study on organic-inorganic perovskite materials" *AIP Advances*, vol. 8, no. 3, p. 035114, 2018/03/01 2018, doi: 10.1063/1.5021755.
- [229] C. Stavrakas *et al.*, "Probing buried recombination pathways in perovskite structures using 3D photoluminescence tomography" *Energy & Environmental Science*, 10.1039/C8EE00928G vol. 11, no. 10, pp. 2846-2852, 2018, doi: 10.1039/C8EE00928G.
- [230] X. F. Tang *et al.*, "Local Observation of Phase Segregation in Mixed-Halide Perovskite" *Nano Letters*, vol. 18, no. 3, pp. 2172-2178, MAR 2018, doi: 10.1021/acs.nanolett.8b00505.
- [231] V. Trifiletti, A. Cannavale, A. Listorti, A. Rizzo, and S. Colella, "Sequential deposition of hybrid halide perovskite starting both from lead iodide and lead chloride on the most widely employed substrates" *Thin Solid Films*, vol. 657, pp. 110-117, 2018/07/01/ 2018, doi: <https://doi.org/10.1016/j.tsf.2018.05.022>.
- [232] Y. Wang *et al.*, "Integration of a functionalized graphene nano-network into a planar perovskite absorber for high-efficiency large-area solar cells" *Materials Horizons*, 10.1039/C8MH00511G vol. 5, no. 5, pp. 868-873, 2018, doi: 10.1039/C8MH00511G.
- [233] S. A. L. Weber *et al.*, "How the formation of interfacial charge causes hysteresis in perovskite solar cells" *Energy & Environmental Science*, 10.1039/C8EE01447G vol. 11, no. 9, pp. 2404-2413, 2018, doi: 10.1039/C8EE01447G.
- [234] Y. Yoon, D. Ha, I. J. Park, P. M. Haney, S. Lee, and N. B. Zhitenev, "Nanoscale photocurrent mapping in perovskite solar cells" *Nano Energy*, vol. 48, pp. 543-550, JUN 2018, doi: 10.1016/j.nanoen.2018.04.010.
- [235] J. S. Yun *et al.*, "Humidity-Induced Degradation via Grain Boundaries of HC(NH₂)₂PbI₃ Planar Perovskite Solar Cells" *Advanced Functional Materials*, <https://doi.org/10.1002/adfm.201705363> vol. 28, no. 11, p. 1705363, 2018/03/01 2018, doi: <https://doi.org/10.1002/adfm.201705363>.
- [236] G. Zheng *et al.*, "Manipulation of facet orientation in hybrid perovskite polycrystalline films by cation cascade" *Nature Communications*, vol. 9, no. 1, p. 2793, 2018/07/18 2018, doi: 10.1038/s41467-018-05076-w.
- [237] A. Alberti, C. Bongiorno, E. Smecca, I. Deretzis, A. La Magna, and C. Spinella, "Pb clustering and PbI₂ nanofragmentation during methylammonium lead iodide perovskite degradation" *Nature Communications*, vol. 10, no. 1, p. 2196, 2019/05/16 2019, doi: 10.1038/s41467-019-09909-0.

- [238] J.-P. Correa-Baena *et al.*, "Homogenized halides and alkali cation segregation in alloyed organic-inorganic perovskites" *Science*, vol. 363, no. 6427, pp. 627-631, 2019/02/08 2019, doi: 10.1126/science.aah5065.
- [239] P. Cui *et al.*, "Planar p–n homojunction perovskite solar cells with efficiency exceeding 21.3%" *Nature Energy*, vol. 4, no. 2, pp. 150-159, 2019/02/01 2019, doi: 10.1038/s41560-018-0324-8.
- [240] R. Giridharagopal *et al.*, "Time-Resolved Electrical Scanning Probe Microscopy of Layered Perovskites Reveals Spatial Variations in Photoinduced Ionic and Electronic Carrier Motion" *ACS Nano*, vol. 13, no. 3, pp. 2812-2821, 2019/03/26 2019, doi: 10.1021/acsnano.8b08390.
- [241] A. Gómez, Q. Wang, A. R. Goñi, M. Campoy-Quiles, and A. Abate, "Ferroelectricity-free lead halide perovskites" *Energy & Environmental Science*, 10.1039/C9EE00884E vol. 12, no. 8, pp. 2537-2547, 2019, doi: 10.1039/C9EE00884E.
- [242] T. Haeger, M. Wilmes, R. Heiderhoff, and T. Riedl, "Simultaneous Mapping of Thermal Conductivity, Thermal Diffusivity, and Volumetric Heat Capacity of Halide Perovskite Thin Films: A Novel Nanoscopic Thermal Measurement Technique" *Journal of Physical Chemistry Letters*, vol. 10, no. 11, pp. 3019-3023, JUN 6 2019, doi: 10.1021/acs.jpcelett.9b01053.
- [243] J. Hieulle *et al.*, "Unraveling the Impact of Halide Mixing on Perovskite Stability" *Journal of the American Chemical Society*, vol. 141, no. 8, pp. 3515-3523, 2019/02/27 2019, doi: 10.1021/jacs.8b11210.
- [244] X. Jiang, J. Hoffman, C. C. Stoumpos, M. G. Kanatzidis, and E. Harel, "Transient Sub-Band-Gap States at Grain Boundaries of CH₃NH₃PbI₃ Perovskite Act as Fast Temperature Relaxation Centers" *ACS Energy Letters*, vol. 4, no. 7, pp. 1741-1747, 2019/07/12 2019, doi: 10.1021/acsenerylett.9b00885.
- [245] D. Kim *et al.*, "Light- and bias-induced structural variations in metal halide perovskites" *Nature Communications*, vol. 10, JAN 25 2019, doi: 10.1038/s41467-019-08364-1.
- [246] F. U. Kosasih, L. Rakocevic, T. Aernouts, J. Poortmans, and C. Ducati, "Electron Microscopy Characterization of P3 Lines and Laser Scribing-Induced Perovskite Decomposition in Perovskite Solar Modules" *ACS Applied Materials & Interfaces*, vol. 11, no. 49, pp. 45646-45655, 2019/12/11 2019, doi: 10.1021/acssami.9b15520.
- [247] C. Lu *et al.*, "Carrier Transfer Behaviors at Perovskite/Contact Layer Heterojunctions in Perovskite Solar Cells" *Advanced Materials Interfaces*, <https://doi.org/10.1002/admi.201801253> vol. 6, no. 2, p. 1801253, 2019/01/01 2019, doi: <https://doi.org/10.1002/admi.201801253>.
- [248] J.-Y. Ma, J. Ding, H.-J. Yan, D. Wang, and J.-S. Hu, "Temperature-Dependent Local Electrical Properties of Organic–Inorganic Halide Perovskites: In Situ KPFM and c-AFM Investigation" *ACS Applied Materials & Interfaces*, vol. 11, no. 24, pp. 21627-21633, 2019/06/19 2019, doi: 10.1021/acssami.9b06418.
- [249] H. T. Pham, T. Duong, W. D. A. Rickard, F. Kremer, K. J. Weber, and J. Wong-Leung, "Understanding the Chemical and Structural Properties of Multiple-Cation Mixed

- Halide Perovskite" *The Journal of Physical Chemistry C*, vol. 123, no. 43, pp. 26718-26726, 2019/10/31 2019, doi: 10.1021/acs.jpcc.9b09035.
- [250] C. Stecker *et al.*, "Surface Defect Dynamics in Organic–Inorganic Hybrid Perovskites: From Mechanism to Interfacial Properties" *ACS Nano*, vol. 13, no. 10, pp. 12127-12136, 2019/10/22 2019, doi: 10.1021/acsnano.9b06585.
- [251] R. Szostak *et al.*, "Nanoscale mapping of chemical composition in organic-inorganic hybrid perovskite films" *Science Advances*, vol. 5, no. 10, p. eaaw6619, doi: 10.1126/sciadv.aaw6619.
- [252] E. M. Tennyson *et al.*, "Cesium-Incorporated Triple Cation Perovskites Deliver Fully Reversible and Stable Nanoscale Voltage Response" *ACS Nano*, vol. 13, no. 2, pp. 1538-1546, FEB 2019, doi: 10.1021/acsnano.8b07295.
- [253] S. Wieghold *et al.*, "Halide Heterogeneity Affects Local Charge Carrier Dynamics in Mixed-Ion Lead Perovskite Thin Films" *Chemistry of Materials*, vol. 31, no. 10, pp. 3712-3721, MAY 28 2019, doi: 10.1021/acs.chemmater.9b00650.
- [254] G. Z. Xia *et al.*, "Nanoscale Insights into Photovoltaic Hysteresis in Triple-Cation Mixed-Halide Perovskite: Resolving the Role of Polarization and Ionic Migration" *Advanced Materials*, vol. 31, no. 36, SEP 2019, doi: 10.1002/adma.201902870.
- [255] C. Yang, P. Du, Z. Dai, H. Li, X. Yang, and Q. Chen, "Effects of Illumination Direction on the Surface Potential of CH₃NH₃PbI₃ Perovskite Films Probed by Kelvin Probe Force Microscopy" *ACS Applied Materials & Interfaces*, vol. 11, no. 15, pp. 14044-14050, 2019/04/17 2019, doi: 10.1021/acsami.8b21774.
- [256] F. Zhang, F. Ullrich, S. Silver, R. A. Kerner, B. P. Rand, and A. Kahn, "Complexities of Contact Potential Difference Measurements on Metal Halide Perovskite Surfaces" *The Journal of Physical Chemistry Letters*, vol. 10, no. 4, pp. 890-896, 2019/02/21 2019, doi: 10.1021/acs.jpcclett.8b03878.
- [257] Y. Zhu *et al.*, "Direct atomic scale characterization of the surface structure and planar defects in the organic-inorganic hybrid CH₃NH₃PbI₃ by Cryo-TEM" *Nano Energy*, vol. 73, p. 104820, 2020/07/01/ 2020, doi: <https://doi.org/10.1016/j.nanoen.2020.104820>.
- [258] Y. Zhao *et al.*, "Strain-activated light-induced halide segregation in mixed-halide perovskite solids" *Nature Communications*, vol. 11, no. 1, p. 6328, 2020/12/10 2020, doi: 10.1038/s41467-020-20066-7.
- [259] H. Yi *et al.*, "Thiocyanate assisted nucleation for high performance mix-cation perovskite solar cells with improved stability" *Journal of Power Sources*, vol. 466, p. 228320, 2020/08/01/ 2020, doi: <https://doi.org/10.1016/j.jpowsour.2020.228320>.
- [260] X. Yang *et al.*, "Superior Carrier Lifetimes Exceeding 6 μ s in Polycrystalline Halide Perovskites" *Advanced Materials*, <https://doi.org/10.1002/adma.202002585> vol. 32, no. 39, p. 2002585, 2020/10/01 2020, doi: <https://doi.org/10.1002/adma.202002585>.
- [261] S. Wieghold, N. Shirato, V. Rose, and L. Nienhaus, "Investigating the effect of electric fields on lead halide perovskites by scanning tunneling microscopy" *Journal of Applied Physics*, vol. 128, no. 12, SEP 28 2020, doi: 10.1063/5.0011735.

- [262] Y. Wang, Z. Hu, C. Gao, C. Yang, J. Zhang, and Y. Zhu, "Comprehensive Elucidation of Grain Boundary Behavior in All-Inorganic Halide Perovskites by Scanning Probe Microscopy" *Advanced Materials Interfaces*, <https://doi.org/10.1002/admi.201901521> vol. 7, no. 7, p. 1901521, 2020/04/01 2020, doi: <https://doi.org/10.1002/admi.201901521>.
- [263] T. H. Y. Vu *et al.*, "Visualizing the Impact of Light Soaking on Morphological Domains in an Operational Cesium Lead Halide Perovskite Solar Cell" *Journal of Physical Chemistry*, vol. 11, no. 1, pp. 136-143, JAN 2 2020, doi: 10.1021/acs.jpcclett.9b03210.
- [264] O. J. Usiobo *et al.*, "Nanoscale Mass-Spectrometry Imaging of Grain Boundaries in Perovskite Semiconductors" *The Journal of Physical Chemistry C*, vol. 124, no. 42, pp. 23230-23236, 2020/10/22 2020, doi: 10.1021/acs.jpcc.0c07464.
- [265] D. Toth *et al.*, "Nanoscale Charge Accumulation and Its Effect on Carrier Dynamics in Tri-cation Perovskite Structures" *ACS Applied Materials & Interfaces*, vol. 12, no. 42, pp. 48057-48066, OCT 21 2020, doi: 10.1021/acsami.0c10641.
- [266] E. M. Tennyson *et al.*, "Correlated Electrical and Chemical Nanoscale Properties in Potassium-Passivated, Triple-Cation Perovskite Solar Cells" *Advanced Materials Interfaces*, vol. 7, no. 17, SEP 2020, doi: 10.1002/admi.202000515.
- [267] J. Song, Y. Zhou, N. P. Padture, and B. D. Huey, "Anomalous 3D nanoscale photoconduction in hybrid perovskite semiconductors revealed by tomographic atomic force microscopy" *Nature Communications*, vol. 11, no. 1, p. 3308, 2020/07/03 2020, doi: 10.1038/s41467-020-17012-y.
- [268] Y.-H. Seo, J. H. Kim, D.-H. Kim, H.-S. Chung, and S.-I. Na, "In situ TEM observation of the heat-induced degradation of single- and triple-cation planar perovskite solar cells" *Nano Energy*, vol. 77, p. 105164, 2020/11/01/ 2020, doi: <https://doi.org/10.1016/j.nanoen.2020.105164>.
- [269] U. Rothmann Mathias *et al.*, "Atomic-scale microstructure of metal halide perovskite" *Science*, vol. 370, no. 6516, p. eabb5940, 2020/10/30 2020, doi: 10.1126/science.abb5940.
- [270] J. Nishida, A. H. Alfaifi, T. P. Gray, S. E. Shaheen, and M. B. Raschke, "Heterogeneous Cation-Lattice Interaction and Dynamics in Triple-Cation Perovskites Revealed by Infrared Vibrational Nanoscopy" *ACS Energy Letters*, vol. 5, no. 5, pp. 1636-1643, MAY 8 2020, doi: 10.1021/acsenergylett.0c00522.
- [271] J. Y. Ma *et al.*, "Microscopic investigations on the surface-state dependent moisture stability of a hybrid perovskite" *Nanoscale*, vol. 12, no. 14, pp. 7759-7765, APR 14 2020, doi: 10.1039/c9nr10137c.
- [272] J. Llacer *et al.*, "Nanoscale Studies at the Early Stage of Water-Induced Degradation of CH₃NH₃PbI₃ Perovskite Films Used for Photovoltaic Applications" *ACS Applied Nano Materials*, vol. 3, no. 8, pp. 8268-8277, 2020/08/28 2020, doi: 10.1021/acsanm.0c01687.
- [273] X. Jiang, S. Jun, J. Hoffman, M. G. Kanatzidis, and E. Harel, "Global Analysis for Time and Spectrally Resolved Multidimensional Microscopy: Application to CH₃NH₃PbI₃ Perovskite Thin Films" *The Journal of Physical Chemistry A*, vol. 124, no. 23, pp. 4837-4847, 2020/06/11 2020, doi: 10.1021/acs.jpca.0c01829.

- [274] D. S. Jakob, H. M. Wang, G. H. Zeng, D. E. Otzen, Y. Yan, and X. J. G. Xu, "Peak Force Infrared-Kelvin Probe Force Microscopy" *Angewandte Chemie-International Edition*, vol. 59, no. 37, pp. 16083-16090, SEP 7 2020, doi: 10.1002/anie.202004211.
- [275] D. Di Girolamo *et al.*, "Ion Migration-Induced Amorphization and Phase Segregation as a Degradation Mechanism in Planar Perovskite Solar Cells" *Advanced Energy Materials*, <https://doi.org/10.1002/aenm.202000310> vol. 10, no. 25, p. 2000310, 2020/07/01 2020, doi: <https://doi.org/10.1002/aenm.202000310>.
- [276] Z. Andaji-Garmaroudi *et al.*, "Elucidating and Mitigating Degradation Processes in Perovskite Light-Emitting Diodes" *Advanced Energy Materials*, vol. 10, no. 48, DEC 2020, doi: 10.1002/aenm.202002676.
- [277] G. Alosaimi, S. J. Shin, R. L. Chin, J. H. Kim, J. S. Yun, and J. Seidel, "Probing Charge Carrier Properties and Ion Migration Dynamics of Indoor Halide Perovskite PV Devices Using Top- and Bottom-Illumination SPM Studies" *Advanced Energy Materials*, vol. 11, no. 37, OCT 2021, doi: 10.1002/aenm.202101739.
- [278] Y.-H. Deng and L. G. Nest, "Analysis of misidentifications in TEM characterisation of organic-inorganic hybrid perovskite material" *Journal of Microscopy*, <https://doi.org/10.1111/jmi.13000> vol. 282, no. 3, pp. 195-204, 2021/06/01 2021, doi: <https://doi.org/10.1111/jmi.13000>.
- [279] K. Frohna *et al.*, "Nanoscale chemical heterogeneity dominates the optoelectronic response of alloyed perovskite solar cells" *Nature Nanotechnology*, no. 17, p. 6, 2022, doi: 10.1038/s41565-021-01019-7.
- [280] T. Gallet, R. G. Poeira, E. M. Lanzoni, T. Abzieher, U. W. Paetzold, and A. Redinger, "Co-evaporation of CH₃NH₃PbI₃: How Growth Conditions Impact Phase Purity, Photostriction, and Intrinsic Stability" *ACS Applied Materials & Interfaces*, vol. 13, no. 2, pp. 2642-2653, 2021/01/20 2021, doi: 10.1021/acsami.0c19038.
- [281] Y. X. Guo *et al.*, "Photoinduced Self-healing of Halide Segregation in Mixed-halide Perovskites" *ACS Energy Letters*, vol. 6, no. 7, pp. 2502-2511, JUL 9 2021, doi: 10.1021/acsenenergylett.1c01040.
- [282] Y. Hui *et al.*, "Stability of Perovskite Thin Films under Working Condition: Bias-Dependent Degradation and Grain Boundary Effects" *Advanced Functional Materials*, <https://doi.org/10.1002/adfm.202103894> vol. 31, no. 36, p. 2103894, 2021/09/01 2021, doi: <https://doi.org/10.1002/adfm.202103894>.
- [283] D. Kim *et al.*, "Exploring Responses of Contact Kelvin Probe Force Microscopy in Triple-Cation Double-Halide Perovskites" *The Journal of Physical Chemistry C*, vol. 125, no. 22, pp. 12355-12365, 2021/06/10 2021, doi: 10.1021/acs.jpcc.1c02474.
- [284] S. Kosar *et al.*, "Unraveling the varied nature and roles of defects in hybrid halide perovskites with time-resolved photoemission electron microscopy" *Energy & Environmental Science*, 10.1039/D1EE02055B vol. 14, no. 12, pp. 6320-6328, 2021, doi: 10.1039/D1EE02055B.
- [285] F. U. Kosasih, S. Cacovich, G. Divitini, and C. Ducati, "Nanometric Chemical Analysis of Beam-Sensitive Materials: A Case Study of STEM-EDX on Perovskite Solar Cells"

- Small Methods*, <https://doi.org/10.1002/smtd.202000835> vol. 5, no. 2, p. 2000835, 2021/02/01 2021, doi: <https://doi.org/10.1002/smtd.202000835>.
- [286] A. Krishna *et al.*, "Nanoscale interfacial engineering enables highly stable and efficient perovskite photovoltaics" *Energy & Environmental Science*, 10.1039/D1EE02454J vol. 14, no. 10, pp. 5552-5562, 2021, doi: 10.1039/D1EE02454J.
- [287] W. Li *et al.*, "The critical role of composition-dependent intragrain planar defects in the performance of MA(1)(-)(x)FA(x)PbI(3) perovskite solar cells" *NATURE ENERGY*, vol. 6, no. 6, pp. 624-632, JUN 2021, doi: 10.1038/s41560-021-00830-9.
- [288] W.-C. Liao, B. H. Liu, and C.-C. Leu, "Photodegradation pathways of CH₃NH₃PbI₃ organic perovskite polycrystalline film observed by in-situ scanning probe microscopy" *Applied Surface Science*, vol. 545, p. 149081, 2021/04/15/ 2021, doi: <https://doi.org/10.1016/j.apsusc.2021.149081>.
- [289] I. Mela *et al.*, "Revealing Nanomechanical Domains and Their Transient Behavior in Mixed-Halide Perovskite Films" *Advanced Functional Materials*, vol. 31, no. 23, JUN 2021, doi: 10.1002/adfm.202100293.
- [290] H. T. Pham, Y. Yin, G. Andersson, K. J. Weber, T. Duong, and J. Wong-Leung, "Unraveling the influence of CsCl/MACl on the formation of nanotwins, stacking faults and cubic supercell structure in FA-based perovskite solar cells" *Nano Energy*, vol. 87, p. 106226, 2021/09/01/ 2021, doi: <https://doi.org/10.1016/j.nanoen.2021.106226>.
- [291] H. A. Qiu and J. M. Mativetsky, "Nanoscale light- and voltage-induced lattice strain in perovskite thin films" *NANOSCALE*, vol. 13, no. 2, pp. 746-752, JAN 14 2021, doi: 10.1039/d0nr07476d.
- [292] H. A. Qiu and J. M. Mativetsky, "Elucidating the Role of Ion Migration and Band Bending in Perovskite Solar Cell Function at Grain Boundaries via Multimodal Nanoscale Mapping" *Advanced Materials Interfaces*, vol. 8, no. 9, MAY 2021, doi: 10.1002/admi.202001992.
- [293] K. M. Reza *et al.*, "Grain Boundary Defect Passivation in Quadruple Cation Wide-Bandgap Perovskite Solar Cells" *Solar RRL*, vol. 5, no. 4, APR 2021, doi: 10.1002/solr.202000740.
- [294] S. Tang *et al.*, "Complementary bulk and surface passivations for highly efficient perovskite solar cells by gas quenching" *Cell Reports Physical Science*, vol. 2, no. 8, p. 100511, 2021/08/18/ 2021, doi: <https://doi.org/10.1016/j.xcrp.2021.100511>.
- [295] Z. Xuan *et al.*, "Efficient Perovskite Solar Cells with a Gradient Light Absorption Layer and Low VOC Loss Obtained by Interface Engineering" *ACS Applied Energy Materials*, vol. 4, no. 4, pp. 3584-3592, 2021/04/26 2021, doi: 10.1021/acsaem.1c00018.
- [296] X. Yang *et al.*, "Buried Interfaces in Halide Perovskite Photovoltaics" *Advanced Materials*, <https://doi.org/10.1002/adma.202006435> vol. 33, no. 7, p. 2006435, 2021/02/01 2021, doi: <https://doi.org/10.1002/adma.202006435>.
- [297] W. L. Yao *et al.*, "Dependence of the Heterogeneity of Grain Boundaries on Adjacent Grains in Perovskites and Its Impact on Photovoltage" *Small*, no. 18, p. 8, 2021, doi: 10.1002/sml.202105140.

- [298] X. Qiu, Y. Liu, W. Li, and Y. Hu, "Traps in metal halide perovskites: characterization and passivation" *Nanoscale*, vol. 12, no. 44, pp. 22425-22451, Nov 19 2020, doi: 10.1039/d0nr05739h.
- [299] M. U. Rothmann *et al.*, "Direct observation of intrinsic twin domains in tetragonal CH₃NH₃PbI₃" *Nature Communications*, vol. 8, FEB 23 2017, doi: 10.1038/ncomms14547.
- [300] X. Lao *et al.*, "Luminescence and thermal behaviors of free and trapped excitons in cesium lead halide perovskite nanosheets" *Nanoscale*, vol. 10, no. 21, pp. 9949-9956, May 31 2018, doi: 10.1039/c8nr01109e.
- [301] S. D. Stranks, V. M. Burlakov, T. Leijtens, J. M. Ball, A. Goriely, and H. J. Snaith, "Recombination Kinetics in Organic-Inorganic Perovskites: Excitons, Free Charge, and Subgap States" *Physical Review Applied*, vol. 2, no. 3, 2014, doi: 10.1103/PhysRevApplied.2.034007.
- [302] E. V. Pean, S. Dimitrov, C. S. De Castro, and M. L. Davies, "Interpreting time-resolved photoluminescence of perovskite materials" *Phys Chem Chem Phys*, vol. 22, no. 48, pp. 28345-28358, Dec 23 2020, doi: 10.1039/d0cp04950f.
- [303] A. J. Winchester *et al.*, "Investigation of Trap States and Their Dynamics in Hybrid Organic-inorganic Mixed Cation Perovskite Films Using Time Resolved Photoemission Electron Microscopy" in *2018 Conference on Lasers and Electro-Optics (CLEO)*, 2018: IEEE, p. 2.
- [304] E. Bauer, *Surface Microscopy with Low Energy Electrons*. New York: Springer, 2014, p. 513.
- [305] A. Neff, F. Niefind, B. Abel, S. C. B. Mannsfeld, and K. R. Siefermann, "Imaging Nanoscale Morphology of Semiconducting Polymer Films with Photoemission Electron Microscopy" *Adv Mater*, vol. 29, no. 29, Aug 2017, doi: 10.1002/adma.201701012.
- [306] K. Fukumoto *et al.*, "Femtosecond time-resolved photoemission electron microscopy for spatiotemporal imaging of photogenerated carrier dynamics in semiconductors" *Rev Sci Instrum*, vol. 85, no. 8, p. 083705, Aug 2014, doi: 10.1063/1.4893484.
- [307] W. Liu *et al.*, "Mapping Trap Dynamics in a CsPbBr₃ Single-Crystal Microplate by Ultrafast Photoemission Electron Microscopy" *Nano Lett*, vol. 21, no. 7, pp. 2932-2938, Apr 14 2021, doi: 10.1021/acs.nanolett.1c00014.
- [308] E. L. Wong, J. Winchester Andrew, V. Pareek, J. Madéo, K. L. Man Michael, and M. Dani Keshav, "Pulling apart photoexcited electrons by photoinducing an in-plane surface electric field" *Science Advances*, vol. 4, no. 9, p. eaat9722, 2018, doi: 10.1126/sciadv.aat9722.
- [309] L. Wittenbecher *et al.*, "Unraveling the Ultrafast Hot Electron Dynamics in Semiconductor Nanowires" *ACS Nano*, vol. 15, no. 1, pp. 1133-1144, Jan 26 2021, doi: 10.1021/acsnano.0c08101.
- [310] M. K. L. Man *et al.*, "Imaging the motion of electrons across semiconductor heterojunctions" *Nature Nanotechnology*, vol. 12, no. 1, pp. 36-40, 2017/01/01 2017, doi: 10.1038/nnano.2016.183.

- [311] M. Da Browski, Y. Dai, and H. Petek, "Ultrafast Photoemission Electron Microscopy: Imaging Plasmons in Space and Time" *Chem Rev*, vol. 120, no. 13, pp. 6247-6287, Jul 8 2020, doi: 10.1021/acs.chemrev.0c00146.
- [312] K. Yamagiwa, M. Shibuta, and A. Nakajima, "Visualization of Surface Plasmons Propagating at the Buried Organic/Metal Interface with Silver Nanocluster Sensitizers" *ACS Nano*, vol. 14, no. 2, pp. 2044-2052, Feb 25 2020, doi: 10.1021/acsnano.9b08653.
- [313] G. Spektor, E. Prinz, M. Hartelt, A.-K. Mahro, M. Aeschlimann, and M. Orenstein, "Orbital angular momentum multiplication in plasmonic vortex cavities" *Science Advances*, vol. 7, no. 33, p. eabg5571, doi: 10.1126/sciadv.abg5571.
- [314] Q. Sun, K. Ueno, H. Yu, A. Kubo, Y. Matsuo, and H. Misawa, "Direct imaging of the near field and dynamics of surface plasmon resonance on gold nanostructures using photoemission electron microscopy" *Light: Science & Applications*, vol. 2, no. 12, pp. e118-e118, 2013/12/01 2013, doi: 10.1038/lsa.2013.74.
- [315] F. J. Meyer zu Heringdorf, L. I. Chelaru, S. Möllenbeck, D. Thien, and M. Horn-von Hoegen, "Femtosecond photoemission microscopy" *Surface Science*, vol. 601, no. 20, pp. 4700-4705, 2007, doi: 10.1016/j.susc.2007.05.052.
- [316] T. Taniuchi, Y. Kotani, and S. Shin, "Ultrahigh-spatial-resolution chemical and magnetic imaging by laser-based photoemission electron microscopy" *Rev Sci Instrum*, vol. 86, no. 2, p. 023701, Feb 2015, doi: 10.1063/1.4906755.
- [317] F. Kronast, J. Schlichting, F. Radu, S. K. Mishra, T. Noll, and H. A. Dürr, "Spin-resolved photoemission microscopy and magnetic imaging in applied magnetic fields" *Surface and Interface Analysis*, <https://doi.org/10.1002/sia.3561> vol. 42, no. 10-11, pp. 1532-1536, 2010/10/01 2010, doi: <https://doi.org/10.1002/sia.3561>.
- [318] R. Juge *et al.*, "Magnetic skyrmions in confined geometries: Effect of the magnetic field and the disorder" *Journal of Magnetism and Magnetic Materials*, vol. 455, pp. 3-8, 2018/06/01/ 2018, doi: <https://doi.org/10.1016/j.jmmm.2017.10.030>.
- [319] D. N. Peles and J. D. Simon, "Challenges in Applying Photoemission Electron Microscopy to Biological Systems†" *Photochemistry and Photobiology*, <https://doi.org/10.1111/j.1751-1097.2008.00484.x> vol. 85, no. 1, pp. 8-20, 2009/01/01 2009, doi: <https://doi.org/10.1111/j.1751-1097.2008.00484.x>.
- [320] A. Skallberg, K. Bunnfors, C. Brommesson, and K. Uvdal, "New Tools for Imaging Neutrophils: Work Function Mapping and Element-Specific, Label-Free Imaging of Cellular Structures" *Nano Letters*, vol. 21, no. 1, pp. 222-229, 2021/01/13 2021, doi: 10.1021/acs.nanolett.0c03554.
- [321] K. Fukumoto *et al.*, "Visualization of ultrafast electron dynamics using time-resolved photoemission electron microscopy" in *19th International Conference on Ultrafast Phenomena*, 2014/07/07 Optica Publishing Group, 09.Wed.E.3, doi: 10.1364/UP.2014.09.Wed.E.3.
- [322] A. D. Smith, G. Cressey, P. F. Schofield, and B. A. Cressey, "Development of X-ray photoemission electron microscopy (X-PEEM) at the SRS" *Journal of Synchrotron Radiation*, vol. 5, no. 3, pp. 1108-1110, 1998, doi: doi:10.1107/S0909049597015811.

- [323] C. N. Berglund and W. E. Spicer, "Photoemission Studies of Copper and Silver: Theory" *Physical Review*, vol. 136, no. 4A, pp. A1030-A1044, 11/16/ 1964, doi: 10.1103/PhysRev.136.A1030.
- [324] S. Hüfner, "*Photoelectron spectroscopy: principles and applications*", Third Edition ed. (QC454.P48 H84 2003). New York: Springer -Verlag Berlin Heidelberg GmbH, 2003, p. 671. 2003.
- [325] T. O. Menteş and A. Locatelli, "Angle-resolved X-ray photoemission electron microscopy" *Journal of Electron Spectroscopy and Related Phenomena*, vol. 185, no. 10, pp. 323-329, 2012, doi: 10.1016/j.elspec.2012.07.007.
- [326] E. Brüche, "Elektronenmikroskopische Abbildung mit lichtelektrischen Elektronen" *Zeitschrift für Physik*, vol. 86, no. 7, pp. 448-450, 1933/07/01 1933, doi: 10.1007/BF01341360.
- [327] E. Bauer, "A brief history of PEEM" *Journal of Electron Spectroscopy and Related Phenomena*, vol. 185, no. 10, pp. 314-322, 2012, doi: 10.1016/j.elspec.2012.08.001.
- [328] H. H. Rotermund, W. Engel, M. Kordesch, and G. Ertl, "Imaging of spatio-temporal pattern evolution during carbon monoxide oxidation on platinum" *Nature*, vol. 343, no. 6256, pp. 355-357, 1990/01/01 1990, doi: 10.1038/343355a0.
- [329] E. Bauer and T. Schmidt, "Multi-Method High-Resolution Surface Analysis with Slow Electrons" in *High-Resolution Imaging and Spectrometry of Materials*, F. Ernst and M. Rühle Eds. Berlin, Heidelberg: Springer Berlin Heidelberg, 2003, pp. 363-390.
- [330] O. Hayes Griffith and W. Engel, "Historical perspective and current trends in emission microscopy, mirror electron microscopy and low-energy electron microscopy: An introduction to the proceedings of the second international symposium and workshop on emission microscopy and related techniques" *Ultramicroscopy*, vol. 36, no. 1, pp. 1-28, 1991/05/01/ 1991, doi: [https://doi.org/10.1016/0304-3991\(91\)90135-S](https://doi.org/10.1016/0304-3991(91)90135-S).
- [331] G. Massey, M. Jones, and J. Johnson, "Nonlinear photoemission for viewing guided or evanescent waves" *IEEE Journal of Quantum Electronics*, vol. 17, no. 6, pp. 1035-1041, 1981, doi: 10.1109/JQE.1981.1071242.
- [332] N. M. Buckanie, J. Gohre, P. Zhou, D. von der Linde, M. Horn-von Hoegen, and F. J. Meyer Zu Heringdorf, "Space charge effects in photoemission electron microscopy using amplified femtosecond laser pulses" *J Phys Condens Matter*, vol. 21, no. 31, p. 314003, Aug 5 2009, doi: 10.1088/0953-8984/21/31/314003.
- [333] B. Schönhense *et al.*, "Multidimensional photoemission spectroscopy - the space-charge limit" *New Journal of Physics*, vol. 20, no. 3, 2018, doi: 10.1088/1367-2630/aaa262.
- [334] F. Rotermund and V. Petrov, "Generation of the fourth harmonic of a femtosecond Ti:sapphire laser" *Opt. Lett.*, vol. 23, no. 13, pp. 1040-1042, 1998/07/01 1998, doi: 10.1364/OL.23.001040.
- [335] A. D. Smith, P. F. Schofield, A. Scholl, R. A. D. Patrick, and J. C. Bridges, "XPEEM valence state imaging of mineral micro-intergrowths with a spatial resolution of 100nm" *Journal de Physique IV*, vol. 104, pp. 373-376, 2003, doi: 10.1051/jp4:20030103.

- [336] M. P. Seah and W. A. Dench, "Quantitative electron spectroscopy of surfaces: A standard data base for electron inelastic mean free paths in solids" *Surface and Interface Analysis*, <https://doi.org/10.1002/sia.740010103> vol. 1, no. 1, pp. 2-11, 1979/02/01 1979, doi: <https://doi.org/10.1002/sia.740010103>.
- [337] H. T. Nguyen-Truong, "Electron inelastic mean free path at energies below 100 eV" *J Phys Condens Matter*, vol. 29, no. 21, p. 215501, Jun 1 2017, doi: 10.1088/1361-648X/aa6b9d.
- [338] Refractiveindexinfo. "Refractive index database." <https://refractiveindex.info/>.
- [339] O. Bostanjoglo and M. Weingärtner, "Pulsed photoelectron microscope for imaging laser-induced nanosecond processes" *Review of Scientific Instruments*, vol. 68, no. 6, pp. 2456-2460, 1997/06/01 1997, doi: 10.1063/1.1148168.
- [340] O. Schmidt *et al.*, "Time-resolved two photon photoemission electron microscopy" *Applied Physics B: Lasers and Optics*, vol. 74, pp. 223-227, 2002, doi: 10.1007/s003400200803.
- [341] L. Wang, C. Xu, M. Y. Li, L. J. Li, and Z. H. Loh, "Unraveling Spatially Heterogeneous Ultrafast Carrier Dynamics of Single-Layer WSe₂ by Femtosecond Time-Resolved Photoemission Electron Microscopy" *Nano Lett*, vol. 18, no. 8, pp. 5172-5178, Aug 8 2018, doi: 10.1021/acs.nanolett.8b02103.
- [342] M. Maiuri, M. Garavelli, and G. Cerullo, "Ultrafast Spectroscopy: State of the Art and Open Challenges" *Journal of the American Chemical Society*, vol. 142, no. 1, pp. 3-15, 2020/01/08 2020, doi: 10.1021/jacs.9b10533.
- [343] P. E. Marchezi *et al.*, "Degradation mechanisms in mixed-cation and mixed-halide Cs_xFA_{1-x}Pb(BryI_{1-y})₃ perovskite films under ambient conditions" *Journal of Materials Chemistry A*, vol. 8, no. 18, pp. 9302-9312, 2020, doi: 10.1039/d0ta01201g.
- [344] A. Verna, G. Greco, V. Lollobrigida, F. Offi, and G. Stefani, "Space-charge effects in high-energy photoemission" *Journal of Electron Spectroscopy and Related Phenomena*, vol. 209, pp. 14-25, 2016, doi: 10.1016/j.elspec.2016.03.001.
- [345] C. Xiao *et al.*, "Mechanisms of Electron-Beam-Induced Damage in Perovskite Thin Films Revealed by Cathodoluminescence Spectroscopy" *The Journal of Physical Chemistry C*, vol. 119, no. 48, pp. 26904-26911, 2015/12/03 2015, doi: 10.1021/acs.jpcc.5b09698.
- [346] K. Siegrist, E. D. Williams, and V. W. Ballarotto, "Characterizing topography-induced contrast in photoelectron emission microscopy" *Journal of Vacuum Science & Technology A: Vacuum, Surfaces, and Films*, vol. 21, no. 4, pp. 1098-1102, 2003, doi: 10.1116/1.1562185.
- [347] G. Tumen-Ulzii *et al.*, "Detrimental Effect of Unreacted PbI₂ on the Long-Term Stability of Perovskite Solar Cells" *Adv Mater*, vol. 32, no. 16, p. e1905035, Apr 2020, doi: 10.1002/adma.201905035.
- [348] Q. Chen *et al.*, "Controllable self-induced passivation of hybrid lead iodide perovskites toward high performance solar cells" *Nano Lett*, vol. 14, no. 7, pp. 4158-63, Jul 9 2014, doi: 10.1021/nl501838y.

- [349] Y. Chen *et al.*, "Mechanism of PbI₂ in Situ Passivated Perovskite Films for Enhancing the Performance of Perovskite Solar Cells" *ACS Appl Mater Interfaces*, vol. 11, no. 47, pp. 44101-44108, Nov 27 2019, doi: 10.1021/acsami.9b13648.
- [350] K. Nakano, Y. Kaji, and K. Tajima, "Highly Sensitive Evaluation of Density of States in Molecular Semiconductors by Photoelectron Yield Spectroscopy in Air" *ACS Applied Materials & Interfaces*, vol. 13, no. 24, pp. 28574-28582, 2021/06/23 2021, doi: 10.1021/acsami.1c05686.
- [351] C. De Blasi, C. Galassini, C. Manfredotti, G. Micocci, L. Ruggiero, and A. Tepore, "Trapping Levels in PbI₂" *Solid State Communications*, vol. 25, p. 5, 1978.
- [352] J. M. Azpiroz, E. Mosconi, J. Bisquert, and F. De Angelis, "Defect migration in methylammonium lead iodide and its role in perovskite solar cell operation" *Energy & Environmental Science*, vol. 8, no. 7, pp. 2118-2127, 2015, doi: 10.1039/c5ee01265a.
- [353] S. W. Lee *et al.*, "UV Degradation and Recovery of Perovskite Solar Cells" *Sci Rep*, vol. 6, p. 38150, Dec 2 2016, doi: 10.1038/srep38150.
- [354] K. Chen *et al.*, "Defect passivation by alcohol-soluble small molecules for efficient p-i-n planar perovskite solar cells with high open-circuit voltage" *Journal of Materials Chemistry A*, vol. 7, no. 37, pp. 21140-21148, 2019, doi: 10.1039/c9ta06718c.
- [355] Q. Jiang *et al.*, "Surface passivation of perovskite film for efficient solar cells" *Nature Photonics*, vol. 13, no. 7, pp. 460-466, 2019, doi: 10.1038/s41566-019-0398-2.
- [356] D.-H. Kang, S.-Y. Kim, J.-W. Lee, and N.-G. Park, "Efficient surface passivation of perovskite films by a post-treatment method with a minimal dose" *Journal of Materials Chemistry A*, 10.1039/D0TA10581C vol. 9, no. 6, pp. 3441-3450, 2021, doi: 10.1039/D0TA10581C.
- [357] S. Tan *et al.*, "Surface Reconstruction of Halide Perovskites During Post-treatment" *Journal of the American Chemical Society*, vol. 143, no. 18, pp. 6781-6786, 2021/05/12 2021, doi: 10.1021/jacs.1c00757.
- [358] M. Ge *et al.*, "Naphthylmethylamine post-treatment of MAPbI₃ perovskite solar cells with simultaneous defect passivation and stability improvement" *Solar Energy*, vol. 220, pp. 18-23, 2021/05/15/ 2021, doi: <https://doi.org/10.1016/j.solener.2021.03.016>.
- [359] N. K. Noel *et al.*, "Enhanced Photoluminescence and Solar Cell Performance via Lewis Base Passivation of Organic-Inorganic Lead Halide Perovskites" *ACS Nano*, vol. 8, no. 10, pp. 9815-9821, 2014/10/28 2014, doi: 10.1021/nn5036476.
- [360] S. Yang *et al.*, "Tailoring Passivation Molecular Structures for Extremely Small Open-Circuit Voltage Loss in Perovskite Solar Cells" *Journal of the American Chemical Society*, vol. 141, no. 14, pp. 5781-5787, 2019/04/10 2019, doi: 10.1021/jacs.8b13091.
- [361] E. Aydin, M. De Bastiani, and S. De Wolf, "Defect and Contact Passivation for Perovskite Solar Cells" *Advanced Materials*, <https://doi.org/10.1002/adma.201900428> vol. 31, no. 25, p. 1900428, 2019/06/01 2019, doi: <https://doi.org/10.1002/adma.201900428>.

- [362] L. Huang, Z. Ge, X. Zhang, and Y. Zhu, "Oxygen-induced defect-healing and photo-brightening of halide perovskite semiconductors: science and application" *Journal of Materials Chemistry A*, vol. 9, no. 8, pp. 4379-4414, 2021, doi: 10.1039/d0ta10946k.
- [363] H.-H. Fang, F. Wang, S. Adjokatse, N. Zhao, and M. A. Loi, "Photoluminescence Enhancement in Formamidinium Lead Iodide Thin Films" *Advanced Functional Materials*, vol. 26, no. 26, pp. 4653-4659, 2016, doi: 10.1002/adfm.201600715.
- [364] J. F. Galisteo-Lopez, M. Anaya, M. E. Calvo, and H. Miguez, "Environmental Effects on the Photophysics of Organic-Inorganic Halide Perovskites" *J Phys Chem Lett*, vol. 6, no. 12, pp. 2200-5, Jun 18 2015, doi: 10.1021/acs.jpcclett.5b00785.
- [365] M. Anaya, J. F. Galisteo-Lopez, M. E. Calvo, J. P. Espinos, and H. Miguez, "Origin of Light-Induced Photophysical Effects in Organic Metal Halide Perovskites in the Presence of Oxygen" *J Phys Chem Lett*, vol. 9, no. 14, pp. 3891-3896, Jul 19 2018, doi: 10.1021/acs.jpcclett.8b01830.
- [366] S. Chen *et al.*, "Light Illumination Induced Photoluminescence Enhancement and Quenching in Lead Halide Perovskite" *Solar RRL*, vol. 1, no. 1, 2017, doi: 10.1002/solr.201600001.
- [367] Y. Tian *et al.*, "Mechanistic insights into perovskite photoluminescence enhancement: light curing with oxygen can boost yield thousandfold" *Phys Chem Chem Phys*, vol. 17, no. 38, pp. 24978-87, Oct 14 2015, doi: 10.1039/c5cp04410c.
- [368] S. Cacovich *et al.*, "Light-Induced Passivation in Triple Cation Mixed Halide Perovskites: Interplay between Transport Properties and Surface Chemistry" *ACS Appl Mater Interfaces*, vol. 12, no. 31, pp. 34784-34794, Aug 5 2020, doi: 10.1021/acsmami.0c06844.
- [369] D. Guo, Z. Andaji Garmaroudi, M. Abdi-Jalebi, S. D. Stranks, and T. J. Savenije, "Reversible Removal of Intermixed Shallow States by Light Soaking in Multication Mixed Halide Perovskite Films" *ACS Energy Lett*, vol. 4, no. 10, pp. 2360-2367, Oct 11 2019, doi: 10.1021/acsenerylett.9b01726.
- [370] A. Szemjonov *et al.*, "Impact of Oxygen on the Electronic Structure of Triple-Cation Halide Perovskites" *ACS Materials Letters*, vol. 1, no. 5, pp. 506-510, 2019, doi: 10.1021/acsmaterialslett.9b00294.
- [371] Y.-B. Lu *et al.*, "Light enhanced moisture degradation of perovskite solar cell material CH₃NH₃PbI₃" *Journal of Materials Chemistry A*, vol. 7, no. 48, pp. 27469-27474, 2019, doi: 10.1039/c9ta10443g.
- [372] E. T. Hoke, D. J. Slotcavage, E. R. Dohner, A. R. Bowring, H. I. Karunadasa, and M. D. McGehee, "Reversible photo-induced trap formation in mixed-halide hybrid perovskites for photovoltaics" *Chem Sci*, vol. 6, no. 1, pp. 613-617, Jan 1 2015, doi: 10.1039/c4sc03141e.
- [373] A. J. Knight *et al.*, "Electronic Traps and Phase Segregation in Lead Mixed-Halide Perovskite" *ACS Energy Letters*, vol. 4, no. 1, pp. 75-84, 2018, doi: 10.1021/acsenerylett.8b02002.

- [374] A. J. Knight and L. M. Herz, "Preventing phase segregation in mixed-halide perovskites: a perspective" *Energy & Environmental Science*, vol. 13, no. 7, pp. 2024-2046, 2020, doi: 10.1039/d0ee00788a.
- [375] C. Bi, X. Zheng, B. Chen, H. Wei, and J. Huang, "Spontaneous Passivation of Hybrid Perovskite by Sodium Ions from Glass Substrates: Mysterious Enhancement of Device Efficiency Revealed" *ACS Energy Letters*, vol. 2, no. 6, pp. 1400-1406, 2017/06/09 2017, doi: 10.1021/acseenergylett.7b00356.
- [376] M. Saliba *et al.*, "Incorporation of rubidium cations into perovskite solar cells improves photovoltaic performance" *Science*, vol. 354, no. 6309, pp. 206-209, 2016/10/14 2016, doi: 10.1126/science.aah5557.
- [377] E. L. Unger *et al.*, "Chloride in Lead Chloride-Derived Organo-Metal Halides for Perovskite-Absorber Solar Cells" *Chemistry of Materials*, vol. 26, no. 24, pp. 7158-7165, 2014/12/23 2014, doi: 10.1021/cm503828b.
- [378] Z. Wang *et al.*, "Additive-Modulated Evolution of HC(NH₂)₂PbI₃ Black Polymorph for Mesoscopic Perovskite Solar Cells" *Chemistry of Materials*, vol. 27, no. 20, pp. 7149-7155, 2015/10/27 2015, doi: 10.1021/acs.chemmater.5b03169.
- [379] Q. Li *et al.*, "Efficient Perovskite Solar Cells Fabricated Through CsCl-Enhanced PbI₂ Precursor via Sequential Deposition" *Advanced Materials*, <https://doi.org/10.1002/adma.201803095> vol. 30, no. 40, p. 1803095, 2018/10/01 2018, doi: <https://doi.org/10.1002/adma.201803095>.
- [380] C. Qin, T. Matsushima, T. Fujihara, and C. Adachi, "Multifunctional Benzoquinone Additive for Efficient and Stable Planar Perovskite Solar Cells" *Advanced Materials*, <https://doi.org/10.1002/adma.201603808> vol. 29, no. 4, p. 1603808, 2017/01/01 2017, doi: <https://doi.org/10.1002/adma.201603808>.
- [381] A. J. Winchester, 2020, "Spatially and temporally resolved microscopy of traps in hybrid organic-inorganic perovskites" *PhD Thesis*, Okinawa Institute of Science and Technology Graduate University.
- [382] W. Liu *et al.*, "Imaging and Controlling Photonic Modes in Perovskite Microcavities" *Advanced Materials*, <https://doi.org/10.1002/adma.202100775> vol. 33, no. 25, p. 2100775, 2021/06/01 2021, doi: <https://doi.org/10.1002/adma.202100775>.
- [383] M. De Bastiani *et al.*, "Toward Stable Monolithic Perovskite/Silicon Tandem Photovoltaics: A Six-Month Outdoor Performance Study in a Hot and Humid Climate" *ACS Energy Letters*, vol. 6, no. 8, pp. 2944-2951, 2021, doi: 10.1021/acseenergylett.1c01018.
- [384] H. X. Dang *et al.*, "Multi-cation Synergy Suppresses Phase Segregation in Mixed-Halide Perovskites" *Joule*, vol. 3, no. 7, pp. 1746-1764, 2019, doi: 10.1016/j.joule.2019.05.016.
- [385] J. Liang *et al.*, "Suppressing the Phase Segregation with Potassium for Highly Efficient and Photostable Inverted Wide-Band Gap Halide Perovskite Solar Cells" *ACS Applied Materials & Interfaces*, vol. 12, no. 43, pp. 48458-48466, 2020/10/28 2020, doi: 10.1021/acsaami.0c10310.

- [386] L. Mao, C. C. Stoumpos, and M. G. Kanatzidis, "Two-Dimensional Hybrid Halide Perovskites: Principles and Promises" *Journal of the American Chemical Society*, vol. 141, no. 3, pp. 1171-1190, 2019/01/23 2019, doi: 10.1021/jacs.8b10851.